Tectonic deformation and earthquake hazard in Northwestern Vietnam inferred from GPS observations

（GPS 観測に基づくベトナム北西部の造構性地殻変動と地震ハザードの研究）

NGUYEN ANH DUONG

Doctor of Science
Graduate School of Environmental Studies
Nagoya University

2014

Tectonic deformation and earthquake hazard in Northwestern Vietnam inferred from GPS observations

（GPS 観測に基づくベトナム北西部の造構性地殻変動と地震ハザードの研究）

NGUYEN ANH DUONG

A dissertation for the degree of Doctor of Science

Department of Earth and Environmental Sciences,
Graduate School of Environmental Studies,
Nagoya University

2014

Abstract

Horizontal velocity field determined from a GPS network with 22 sites surveyed from 2001 to 2012 in northwestern Vietnam are presented. The velocity is accurately estimated at each site by fitting a linear trend to each coordinate time series under the assumption that it is constant with time, after accounting for coseismic displacements caused by the 2004 Sumatra and the 2011 Tohoku earthquakes using static fault models. Considering the coseismic effects of the earthquakes, motion of northwestern Vietnam is 34.3 ± 0.7 mm/yr at an azimuth of N108° ± 0.7°E in ITRF2008. This motion is close to, but slightly different from, that of South China block (SC). The area is in a transition zone between this block, the Sundaland block (SU), and the Baoshan subblock. This work also suggests that the deformation between the SC and SU should be spread out toward the south of the study area and is accommodated by multiple NW-SE trending faults probably appear to reach NONN site in central Vietnam. At the local scale, detailed estimation of the crustal deformation across major fault zones is geodetically revealed for the first time. A locking depth of 15.3 ± 9.8 km with an accumulating left-lateral slip rate of 1.8 ± 0.3 mm/yr for Dien Bien Phu fault (DBPF), and a shallow locking depth with a right-lateral slip rate of 1.0 ± 0.6 mm/yr for Son La fault (SLF) and Da River fault (DRF) are identified. The result is consistent with the geological studies in the deformation of each fault and spatial variation of the fault slip rate along DBPF. The geodetically estimated locking depth of DBPF is agreement with the depth distribution of crustal earthquakes as well as the magnetotelluric sounding result. The strain rate field is calculated from the velocity field. As a result, the study area is within the extensional tectonic setting with the moderate strain rate. Focal mechanisms of earthquakes match the estimated strain rates and and the strain rate field is adequately estimated for understanding the tectonic deformation as well as the seismicity in northwestern Vietnam. Earthquakes with maximum magnitude as large as 6.0 could be generated every four or five hundred years with ruptures along middle parts of the SLF and DRF zones. While the DBPF zone could repeatedly rupture events every 566 years with magnitude probably reaching 6.7 or every 1338 years with maximum magnitude of 7.4.

Acknowledgements

Foremost, I would like to express my deepest thanks to my two supervisors, Prof. Fumiaki KIMATA and Prof. Takeshi SAGIYA. Their patience, encouragement, and immense knowledge were key motivations throughout my PhD. They carry out their research with an objective and principled approach to seismology and crustal deformation. They persuasively conveyed an interest in my work. Prof. Kimata has been my supervisor through four years of my PhD research. I am truly thankful for his seless dedication to both my personal and academic development. I cannot think of a better supervisor to have. Prof. Sagiya has become my supervisor after Prof. Kimata retired, from whom I have learnt the vital skill of disciplined critical thinking. His scrutiny of my scientific writing has been invaluable. He has always found the way to propose consistently excellent improvements. In every sense, none of this work would have been possible without him. I owe a great debt of gratitude to Prof. Kimata and Prof. Sagiya.

I would like to thank the colleagues and staffs at Earthquake and Volcano Research Center, Graduate School of Environmental Studies, Nagoya University and Vietnam Institute of Geophysics, Vietnam Academy of Science and Technology for their help and encouragement during my work. In particular, I am grateful to all colleagues of the Vietnam Institute of Geophysics and Institute of Geological Sciences, Vietnam Academy of Science and Technology who participated in the GPS campaigns to collect data for this work.

I am indebted to the Japan Society for the Promotion of Science (JSPS) for direct financial aid through the JSPS RONPAKU (Dissertation PhD) Fellowship. This study was also supported by the National Foundation for Science and Technology Development of Vietnam (NAFOSTED).

I would like to thank my parents. They were always supporting me and encouraging me with their best wishes. Finally, my acknowledgment must go to my lovely wife Yen and my son Binh Minh for their understanding and love during the past few years. Without their support and encouragement I would never have been able to finish my dissertation.

Contents

List of Figures

List of Tables

Glossary of Abbreviations

BS	Baoshan sub-block
CMT	Centroid Moment Tensor
CODE	Center for Orbit Determination in Europe
DBPF	Dien Bien Phu fault
DRF	Da River fault
EU	Eurasian plate
GEODYSSEA	Geodynamics of South and Southeast Asia
GPS	Global Positioning System
GUTE	Gutenberg and Richter earthquake catalog
HRV	Harvard Centroid Moment Tensor
IERS	International Earth Rotation and Reference Systems Service
IGS	International GPS Service
ITRF	International Terrestrial Reference Frame
MRF	Ma River fault
MSK	Medvedev-Sponheuer-Karnik
NWV	Northwestern Vietnam
PPP	Precise Point Positioning
PREM	Preliminary Reference Earth Model
RRF	Red River fault
SLF	Son La fault
SU	Sundaland block

Chapter 1

INTRODUCTION

Crustal tectonic motion may represent the deformation of tectonic regions. The crustal tectonic motion in the continents is extended across wide regions where distributed seismic deformation rather than concentrated in narrow zones at oceanic plate boundaries. This arises a result that the continental deformation zone is usually wider and much more diffuse than that in narrow oceanic plate boundaries (Molnar and Tapponnier, 1975). It implies the deformation in the continents is far more complex than that in the oceans. The crustal tectonic motion of deformation regions is inferred either from spatial variations of strain rates estimated from seismicity (Holt et al., 1991; Jackson et al., 1992; Holt and Haines, 1993), from long-term fault slip rates (England and Molnar, 1997), or directly from GPS measurements (Clarke et al., 1998; McClusky et al., 2000; Sagiya, 2004; Simons et al., 2007). The first two approaches are limited by sparse earthquakes and by lack of geological data over regions of distributed continental deformation such as Northwestern Vietnam where seismic activity is not high. Thus, this study is to apply the GPS measurement technique to the behavior of the continental crust deformation over time-scales of a few years to ten years and at the scale of $\sim$100 km, crossing several active faults at a complex plate boundary, in the region of Northwestern Vietnam.

The northward motion of the Indian - Australian plate with respect to the Eurasian plate (EU) has caused the east-southeastward extrusion of Southeastern Asia (Molnar and Tapponnier, 1975; England and Molnar, 1997). Northwestern Vietnam (NWV) was originally considered to be a part of the Eurasian plate (DeMets et al., 1994). With increasing number of precise geodetic observation, it turned out that the NWV forms a border between the South China block (SC) (Shen et al., 2005) and the Sundaland block (SU) (Simons et al., 2007) (Figure 1.1). The Red River Fault (RRF) in northern Vietnam is regarded as the northeastern tectonic boundary between SC and SU accommodating right-lateral shear strain (Wilson et al., 1998; Michel et al., 2001; Kreemer et al., 2003; Simons et al., 2007). Meanwhile, Bird (2003) and McCaffrey (2009) suggested this

boundary is located farther south. Because of the slow relative motion between the SU and SC blocks and the scarcity of precise space geodetic measurement in this area, the actual location of the tectonic boundary is still uncertain. Thus a dense GPS observation network in NWV can provide an insight into tectonic deformation of this region as well as Southeast Asia.

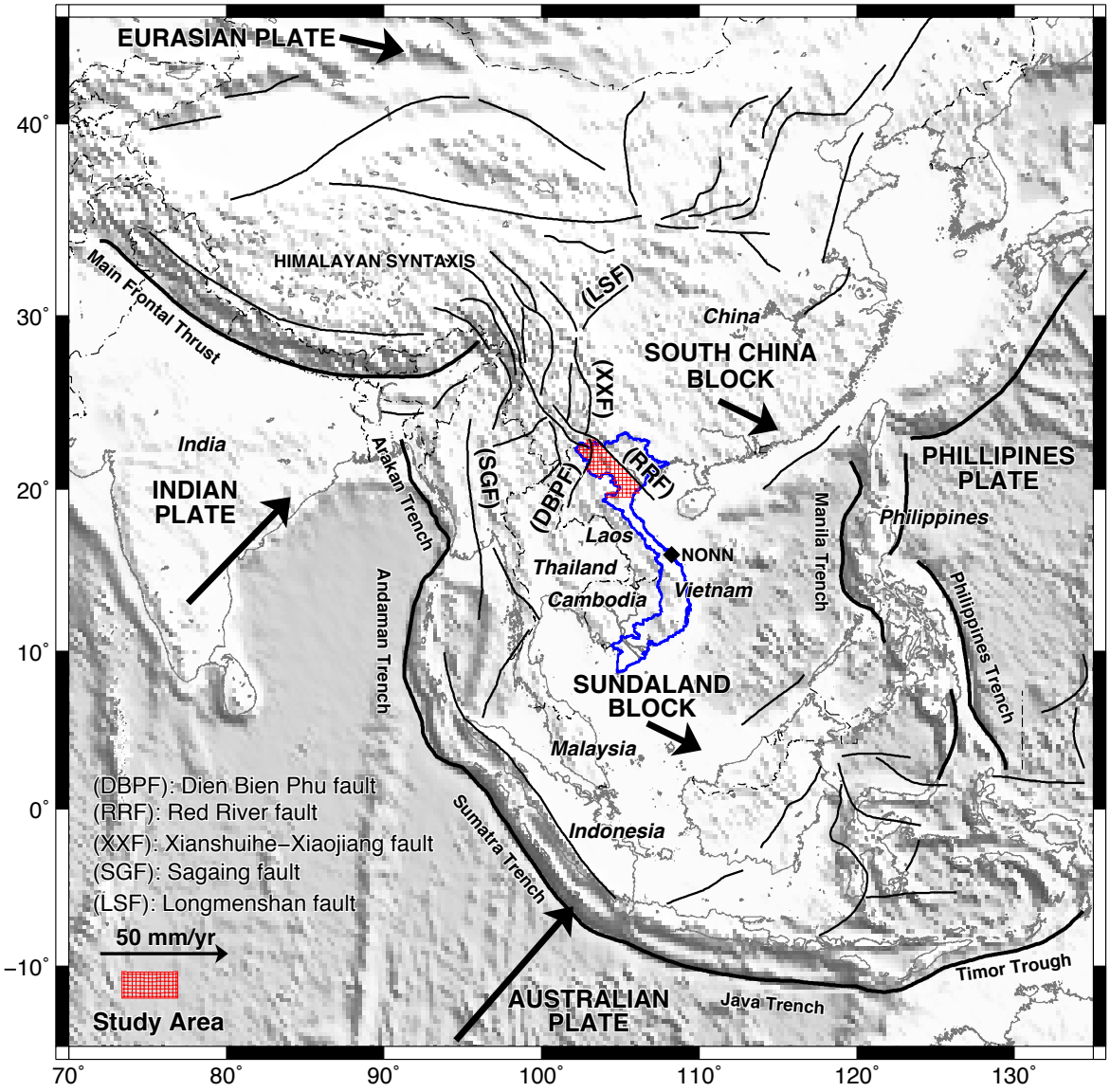

Figure 1.1: Topography, main active faults (thick and thin black lines) from Lacassin et al. (1997); Burchfiel (2004); Simons et al. (2007); Yin (2010). Black arrows denote motions of the Eurasian, Australian, Indian plates and the South China and Sundaland blocks in SE Asia and its vicinity, which are computed using the global plate kinematic model NNR-NUVEL-1A (DeMets et al., 1994). Solid diamond represents NONN site, which is one of GEODYSSEA sites (as described by Simons et al., 2007). The hachure shows the study area shown in Figure 1.2.

In this century, there were two M9 earthquakes occurred: the 26 December 2004 M9.1 Sumatra earthquake (e.g., Lay et al., 2005) and the 11 March 2011 M9.0 Tohoku earthquake (e.g., Simons et al., 2011). Based on GPS observations as well as a dislocation model for a spherical body, far-field coseismic offsets produced by the 2004 Sumatra and the 2011 Tohoku earthquakes at distances thousands of kilometers away from the earthquake rupture were shown to be over 1 mm (e.g., Banerjee et al., 2005; Kreemer et al., 2006; Pollitz et al., 2011). Therefore, the effect of the distant giant earthquakes must be considered to analyze crustal deformation in NWV, where tectonic deformation rate is not high. This was not considered in the previous studies.

The complicated geological structure and the differential tectonic movement had led this study area to the highest seismic activity in Vietnam. Although the seismic hazard is not so great as in the countries situated directly on plate boundaries as Japan, Philippine, Indonesia, the confident information on seismic hazard is necessary due to the safety of local people, infrastructure, as well as numerous great hydropower stations, such us Hoa Binh, Son La, Lai Chau, Nam Chien, and Ban Chat (Figure 1.2) located in such an active zone and seismic prevention against natural disasters related to these constructions. The earthquake potential assessment is necessary to seismic hazard analysis. Accurate estimate of fault slip rate and locking depth is fundamental in evaluation of both the strain rate and seismic moment accumulation rate along a fault as well as in accurately future earthquake prediction for the fault.

In NWV, there are many active faults, such as the Dien Bien Phu Fault (DBPF), the Son La Fault (SLF), the Ma River Fault (MRF), the Da River Fault (DRF), and the Red River Fault (RRF) (Figure 1.2). Along the SLF, DRF, and DBPF zones, the present-day relative movements are geodetically investigated in previous studies (Duong et al., 2006; Tran, 2006), however they are less adequately estimated due to the sparse distribution as well as the short time spanning of GPS sites. Thus, the GPS network in NWV of higher level of accuracy, spatial resolution, and longer time span is utilized to resolve the small relative motions along the faults. On the other hand, study of crustal deformation across a major fault zone is an important factor to analyze the seismic hazard. So the detailed estimation of the crustal deformation across the major fault zones DPBF, DRF, and SLF is geodetically revealed for the first time. The GPS-derived locking depths of the faults are compared with the effective thickness of the locked zones (seismogenic thickness) derived from the seismicity to quantitatively measure the similarities and differences in the two approaches along the faults in NWV.

Earthquake occurrence rate is an important part of seismic hazard assessment. To estimate the earthquake occurrence rate, three major types of data can be utilized: historical seismicity, geological slip rate on active fault, and geodetic slip rate along the

fault. Each approach has limitations. However, the last two approaches need many more assumptions to estimate earthquake occurrence rate. With the accurate estimate of geodetic fault slip rate, in this study, the earthquake occurrence rates of major active faults in NWV are predicted by using some empirical relationship regressions. Additionally, strain rate field is an essential part of seismic hazard analysis that is discussed as the first time for the NVW region. In order to do these it is first necessary to discuss the overall objectives as well as the organization of this dissertation and then reviews the tectonic setting of NWV in the next chapter.

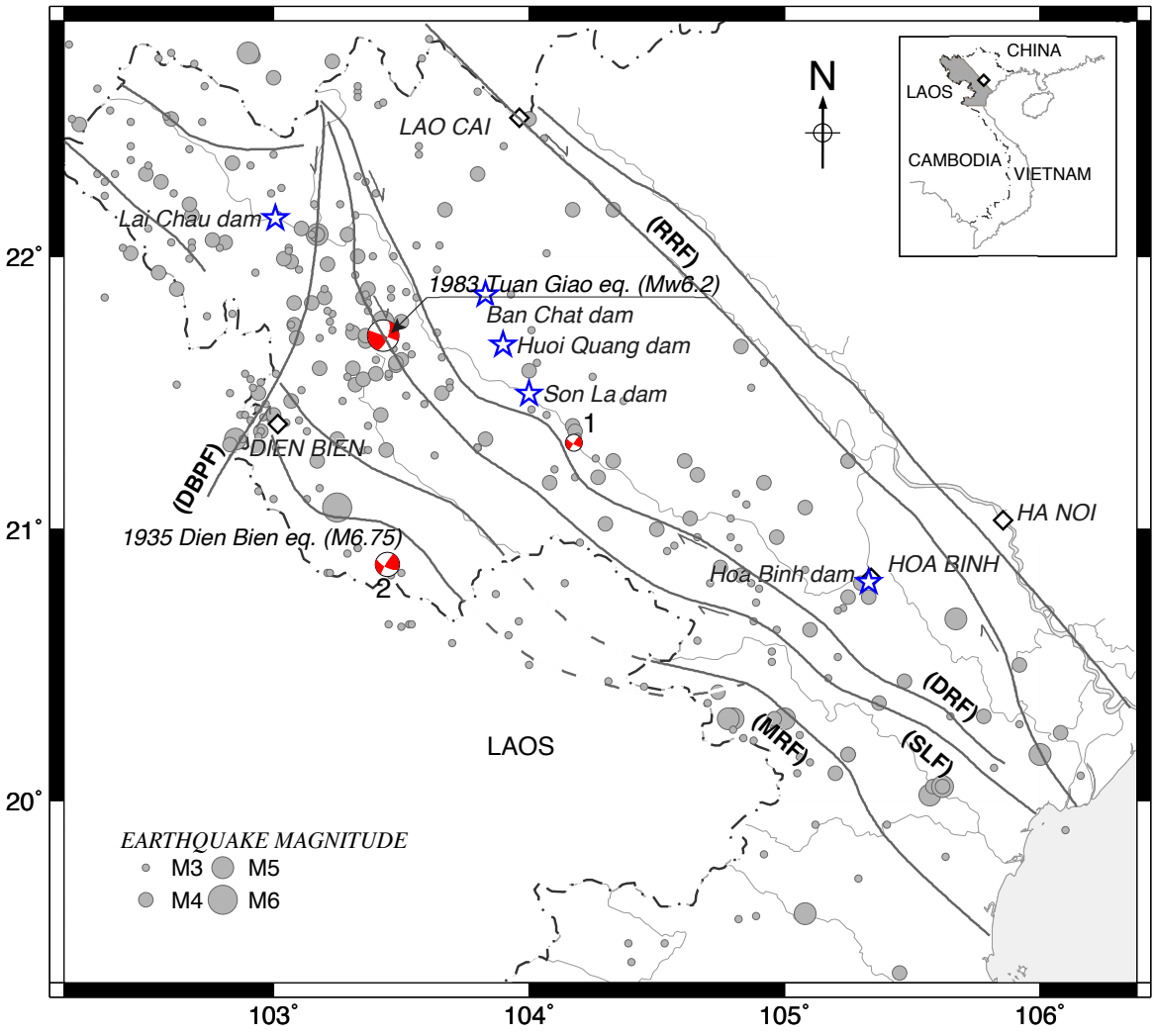

Figure 1.2: Fault system and seismicity map of NWV. Earthquakes with local magnitude 3.0 - 6.8 occurred from 1903 to April 2012 along the fault zones and their vicinities. The focal mechanisms are of the 1983 Tuan Giao earthquake Mw6.2; (1) the 2009 Muong La earthquake Mw3.6; (2) the 2010 Sop Cop earthquake Mw4.8. Thick solid and dashed lines depict the main faults. Thin lines indicate the permanent rivers and the coast of Vietnam. Star symbols are the locations of hydropower dams. Small box denotes the location of the study area in Vietnam. Diamond symbols show cities.

Dissertation objectives

The overall objectives of the work described in this dissertation are to clarify the tectonic affiliation of NWV in South East Asia geodynamic framework and constrain crust deformation across the major fault zones (DBPF, SLF, and DRF) by using a dense GPS observation network in NWV. All the GPS phase data in this region are firstly analyzed to get a coordinate time-series for each GPS site. The coseismic offsets due to great earthquakes are calculated by using static fault models and to offset the time-series. Then the velocity of each GPS site in the ITRF2008 reference frame is calculated from the corrected time-series. The crustal motion of the area is compared with SC, SU, and BS block motions, and the relative motions across the DBPF, SLF, and DRF zones are discussed. Finally, earthquake hazard geodetically assesses by attempting to evaluate the characteristics of the major active faults such as fault slip rate, locking depth, strain rate, seismic moment accumulation rate, potential earthquake magnitude, earthquake occurrence rate, as well as strain rate field of the study region.

Dissertation organization

As this dissertation intends to study the crustal deformation inferred from repeated GPS measurements and its implication for earthquake hazard assessment, knowledge of GPS method, of all aspects of its application as well as of all the GPS phase data is required. Thus, after reviewing the tectonic setting of the study area and its adjacency in Chapter 2, all GPS observation in this study as well as that before this study are being introduced in Chapter 3. A description of the basics of the GPS measurement processing method and interpreted results of coordinate sets derived from the GPS processing are then given in Chapter 4. In the interpreted results, horizontal velocities and their standard deviations at each GPS site are estimated by fitting a straight line through multiple observation epochs using the least squared method, assuming that deviations from this trend are caused by white noise errors. In first part of Chapter 5, we estimate the far-field coseismic displacements caused by the distant great earthquakes at the GPS sites in NWV using static fault models of these earthquakes. The elastic dislocation model for a layered spherical earth model is applied for far-field distance between the source and the GPS sites. The second part of Chapter 5 deals with time-series correction for the far-field coseismic displacements to estimate an average velocity for each GPS site. A comparison is made for the velocity estimates with and without the coseismic offsets for the earthquakes. Chapter 6 presents the crustal movement of NWV and its relation to tectonic blocks. First, block-predicted motions of NWV are calculated by using the Euler poles and the rotation rates of the defined blocks such

as the Sundaland block (SU), the Eurasia plate (EU), the South China block (SC) and the Baoshan sub-block (BS). Second, the tectonic boundary in this region is discussed by using the GPS-derived crustal movements corrected in Chapter 5 along with the block-predicted motions at the GPS sites. Then, the GPS-derived crustal movements are classified basing on study of their relation to the predicted motions of those blocks. Chapter 7 focuses on the earthquake hazard assessment in NWV using the results of GPS measurements. First, relative motions and locking depths of the DBPF, SLF, and DRF zones is geodetically estimated and then compared with the long-term fault slip rates proposed by geological studies and the seismogenic thickness derived from the seismicity, respectively. Next, the strain rate field of NWV is discussed to locate the concentrated deformation zones. Finally, the earthquake potential assessment is implemented for the fault zones by evaluating the strain rates, moment accumulation rates, maximum possible seismic events and their recurrence intervals. Chapter 8 closes this dissertation, in which the conclusion drawn from this study is presented and future research is indicated.

Chapter 2

TECTONIC SETTING OF NORTHWESTERN VIETNAM

The collision between Indian - Australian plate and Eurasian plate has resulted in the formation of the numerous strike slip faults between Myanmar and the Red River fault in the early Cenozoic (Tapponnier et al., 1982, 1990; Lacassin et al., 1997; Morley, 2004; Burchfiel, 2004; Yin, 2010). Northwestern Vietnam (NWV), located in this area, is a mountainous region with a complicated geological structure, dominated by many active faults, such as the Dien Bien Phu Fault (DBPF), the Son La Fault (SLF), the Ma River Fault (MRF), the Da River Fault (DRF), and the Red River Fault (RRF) (Figure 1.2). This region is the most seismically active in Vietnam, limited by DBPF in the west, RRF in the northeast, and MRF in the southwest. The present-day tectonic features of the faults are analyzed on the basis of surface geological investigations (Hung and Vinh, 2001; Zuchiewicz et al., 2004; Tung and Thang, 2006, 2008; Lai et al., 2012) and the studies of deep crustal structures (Cao et al., 2004; Minh et al., 2009, 2011).

2.1 Features of main active faults in NWV

There are now geological data of the fault zones available to discuss both geological fault slip rates and geodetic fault slip rates. In the following, we present the geological settings, focusing on the DBPF, SLF, and DRF zones, the most active fault zones in NWV, where GPS measurement sites in this study are located. Along with their geodetic features the tectonic characteristics of those fault zones will be clarified.

2.1.1 The Dien Bien Phu fault zone

The Dien Bien Phu fault zone, is one of the most seismically active fault zones in Indochina, appears south of the RRF zone in south of Yunnan Province (China), extending (over 150 km in Vietnam) from north of Chieng Chai (Vietnam - China border), through Lai Chau, Dien Bien Phu, to Tay Trang (Vietnam - Laos border) (Figure 2.1). This fault continues into Laos (Lacassin et al., 1997; Holt et al., 2000; Burchfiel, 2004) and probably finishing in Thailand (Leloup et al., 1995; Wang et al., 1998; Lepvrier et al., 2004). By geomorphic expressions the DBPF zone is composed of a number of subsidiary branches (Hung and Vinh, 2001) and simplified in Figure 2.1 by Zuchiewicz et al. (2004). In NWV, the northern part of the fault forms a nearly north-south strike, whereas the southern part gradually turns from southward to a southwestern strike. The main fault and associated subsidiary faults are characterized by strike-slip and oblique-slip displacement with the principal fault plane dipping to the west 60° - 70° in the northern part and 70° - 80° (even to 90°) in the southern part of the fault zone (Hung and Vinh, 2001) or vertically dipping (Minh et al., 2009).

The DBPF zone was formed in the early-middle Jurassic (198 - 158Ma) as the first phase of deformation. Since then the fault zone has gone through several phases of deformations (Tung, 2011). During the Cenozoic, DBPF spent two main tectonic development phases, which are respectively characterized by dextral and sinistral shear activities. The timing of the switch from right- to left-lateral motion on the fault is before 5Ma, in Pliocence (Lacassin et al., 1997; Hung and Vinh, 2001; Tung, 2011). This change of the sense of motion is considered to be a result of the collision between India and Eurasia (Tapponnier et al., 1982, 1990). The present-day geomorphic features of offset streams and regional structural analyses were used to estimate the amount of displacement along the faults. Result that DBPF is left-lateral with an offset of several hundreds of meters to several kilometers in Plio-Quaternary times (Hung and Vinh, 2001; Zuchiewicz et al., 2004; Tung and Thang, 2006, 2008; Tung, 2011; Lai et al., 2012). Presently the fault is of left-lateral and normal left-lateral motions, and the amount of normal component increasing to the north. To deduce a long-term slip rate, the timing of the onset of sinistral motion has been investigated based on the age of the offset drainage. The Holocene slip rate is of 0.6 - 2 mm/yr (Zuchiewicz et al., 2004). The Quaternary slip rate is of 1.1 - 1.8 mm/yr (Hung, 2002) and of 1.1 - 3.0 mm/yr (Tung and Thang, 2006, 2008). The Pliocene average slip rate is on the order of 2.5 mm/yr (Lai et al., 2012). While a large amount of post-Miocene dextral offset along the RRF has been estimated at 20 - 57 km (Allen et al., 1984), even 200 - 250 km (Leloup et al., 1995). Based on the contrasting sense of motion as well as the geometry of recently dextral RRF and sinistral DBPF zones, Zuchiewicz et al. (2004) proposed a

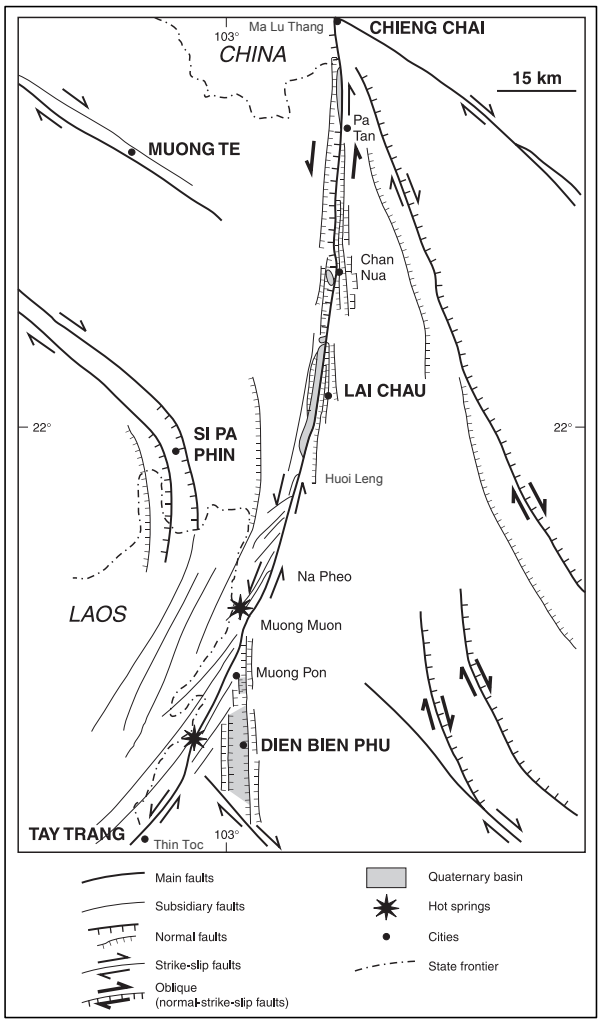

Figure 2.1: Structural sketch of the Dien Bien Phu fault zone (Hung and Vinh, 2001; Zuchiewicz et al., 2004)

conjugate-fault that is capable of generating relatively strong earthquakes in the future.

The DBPF zone is composed by several small, narrow pull-apart basins such as Pa Tan, Chan Nua, Lai Chau (Muong Lay), Na Pheo, Muong Muon, Muong Pon, and Dien Bien Phu (Figure 2.1), where geomorphic observations are mainly conducted (Hung and Vinh, 2001; Zuchiewicz et al., 2004; Tung and Thang, 2006, 2008; Tung, 2011; Lai et al., 2012). The segmentary characteristics of the DBPF zone are clarified with three segments in Vietnam territory, presented by Tung (2011) as the first time. Three segments are different characteristic of activity structure.

- The first segment is about 50 km, extending from Ma Lu Thang to Chan Nua. The associated seismic activity of this segment is scarce and weak.

- The second segment extends about 35 km from Chan Nua to Huoi Leng. This segment is characterized only by moderate size events (only some event with M $<$ 5.0).

- The third is the largest segment of about 70 km from Huoi Leng to Thin Toc. The latter is considered as the strongest seismically active zone compared to the formers with the occurrence of hot springs in the northwest of Muong Pon Village and Dien Bien Town (Figure 2.1) as well as the maximum observed earthquake of Ms5.3 (Son, 2004), (Mw5.1, Van, 2006) occurred on Feb. 19, 2001.

The other evidences of recent activity of the DBPF zone at a local scale are also increased emanations of radon, methane, and carbon dioxide in Lai Chau Town, Na Pheo Village. Moreover, landslide and mudflow disasters frequently occur in high mountain area such as those in 1996 and 1997 at Muong Lay Town (Hung and Vinh, 2001).

2.1.2 The Son La fault zone

The SLF zone is one of the most seismically active faults in NWV. However, compared to the DBPF, the SLF and its neighboring area are generally poorly investigated. According to Hung (2002) and Thuy (2005), the fault zone is summarized as follows. The SLF zone, more than 360 km, stretches northwest - southeast direction. It starts from Nam Nen (Tuan Giao) through Thuan Chau, stretching towards the southeast, then through Mai Son, Moc Chau, Mai Chau, Ba Thuoc, Thach Thanh, Bim Son and reaching the coast at Nga Son (Figure 2.2). The SLF is clearly seen in satellite images, aerial photographs, and topographic maps. It can be divided into 6 segments from northwest to southeast with different morphological structure: Nam Nem - Tuan Giao (about 80 km long); Pha Din (15 km); Pha Din - Chieng Co (40 km); Chieng Co - Chieng Ve (60 km); Chieng Ve - Mai Chau (40 km); Mai Chau - Nga Son (130 km). The main fault has the principal fault plane dipping to the northeast 60° - 80°. Based on the sounding magnetotelluric surveys, the SLF zone is considered to be a trans-crustal deep fault with the vertical or nearly vertical dipping (Minh et al., 2011). The fault zone, probably formed in the late Paleozoic, mainly cuts sedimentary and metamorphic rocks of the Paleozoic - Cenozoic age. The SLF was shaped in two main phases: left-lateral shear motion under sub-latitudinal compressive stress field in the Eocene - Miocene, and right-lateral strike-slip, reflected in the Quaternary fluvial sediments infilling pull-apart basin in Thuan Chau area, under predominately sub-longitude compressive stress field in the Plio-Quaternary times. From the geomorphic pattern of the drainage network along the SLF zone, a probable right-lateral offset on the fault is of 560 - 2000 m, thus the most probable Pleistocene slip rate is of $<$ 1.6 mm/yr (Hung, 2002).

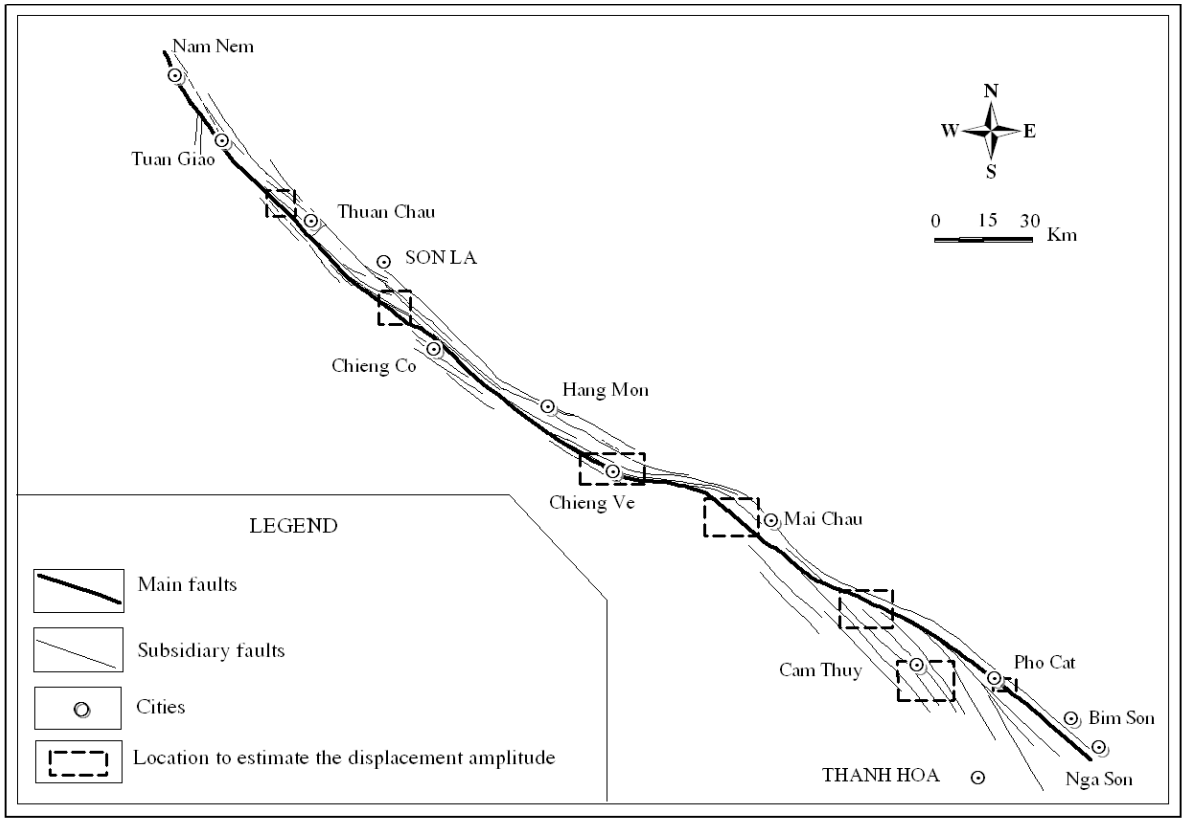

Figure 2.2: Structural sketch of the Son La fault zone (Hung, 2002, simplified).

In neotectonic time frame, the kinematic role of the fault is changed by each segment. The Nam Nem - Tuan Giao segment is normal right-lateral strike slip. The Pha Din, Pha Din - Chieng Co, Chieng Co - Chieng Ve, and Mai Chau - Nga Son segments are right-lateral strike slip. The Chieng Ve - Mai Chau segment is reverse right-lateral strike slip. Compared to the NW and SE parts of the fault, which are active tectonics, the middle part is less active, reflected on topography, geomorphology, and spatial variation of earthquake distribution along the fault zone (Figure 1.2). The fault zone is accompanied by the occurrence of geothermal anomaly and increased emanations of radon, methane and carbon dioxide in Chieng Mai, Chieng Ve, and Bim Son, however by the occurrence of thermal springs being rarely along the fault zone (Hung, 2002). Seismic activity of the SLF zone consists of events with Mw up to 6.2.

2.1.3 The Da River fault zone

Situated between the RRF and SLF zones, the DRF zone is a low-topography area, extending about 460 km from Pa Tan to the coast in Kim Son area (Figure 2.3). Most of the mountains are of low and moderate elevation (500 - 1000 m), except the Pu Sam Cap mountain (> 2000 m above sea level) located in the northwest of the fault zone.

The principal NW-SE trend of this zone is clearly marked on the Conrad interface at the depth of 12 - 14 km. The slightly curved middle section reflects a upward-convex structure on the Conrad interface in southwest of Bac Yen town (Cao et al., 2004).

The DRF is considered as a marginal fault, which is the boundary between the DRF and MRF structural zones (Lepvrier et al., 2004). The DRF and MRF structural zones play an important role for the understanding of the geodynamic evolution of the Indochina and South China blocks during the Indosinian Orogeny. The collision along MRF follows the northwards subduction of Indochina block beneath SC (Carter et al., 2001) and the subsequent development of the DRF which in turn was affected by the Late Triassic Indosinian phase of shortening (Lepvrier et al., 2004). Similar to the NW - SE trending fault systems in NWV, the DRF experienced two main phases of activity: left-lateral strike slip for the early phase and right-lateral strike slip for the later phase. In the later phase, the Quaternary geomorphic features of drainage network along the DRF zone show the right-lateral offset of 1100 - 2500 m and the estimated long-term slip rate of 1.1 - 2.5 mm/yr (Hung, 2002).

The DRF is not only a single fault but a complex set of parallel subsidiary fault systems. The fault zone mainly cuts sedimentary and metamorphic rocks of the Paleozoic - Cenozoic age. Results of geophysical investigations showed that the DRF plunges northeastward with a dip of 70° - 80° in general (Hung, 2002). The occurrences of thermal water sources, earthquakes of moderate magnitude observed along the fault zone, and increased emanations of radon, methane and carbon dioxide, as well as with landcracking and landsliding frequently occurring at different locations are also common within the fault zone (Figure 2.3). Therefore, it indicates that the fault is still active in the present time.

2.2 Seismic activity in NWV and its relation to tectonic setting

In general, data about earthquakes in Vietnam were collected from historical archives, field investigations and instrumental observation. A local seismic station network is installed and maintained by Vietnam Institute of Geophysics. Most of them recorded after 1900 when the number of historical document and seismogram was gradually increasing day by day. Before 1900, we have only few pieces of historical information; the seismic data are not sufficient. The largest observed earthquake occurred in this region is the Yen Dinh earthquake of M=6.8 in 1635 (Thuy, 2005), in the southeastern part of SLF. According to Son (2012) and earthquake catalog compiled by Vietnam Institute

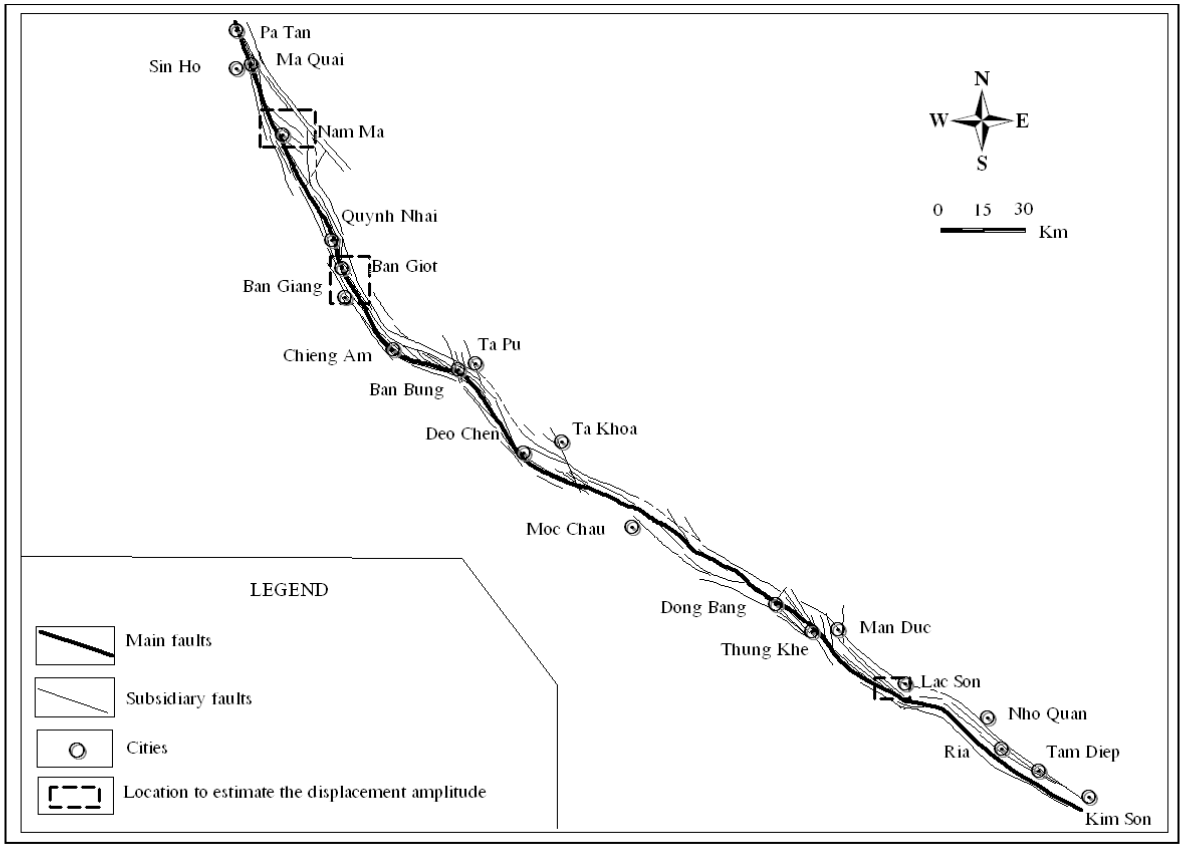

Figure 2.3: Structural sketch of the Da River fault zone (Hung, 2002, simplified)

of Geophysics, 332 earthquakes with local magnitude 3.0 - 6.8 occurred from 1903 to April 2012 in the vicinity of these fault zones. There were two large earthquakes, the 1935 Dien Bien earthquake (M6.75, according to earthquake catalog compiled by B. Gutenberg and C. Richter (GUTE) in 1954) in the northwestern part of MRF close to Dien Bien Phu city and the 24 June 1983 Tuan Giao earthquake (Mw6.2, according to Harvard CMT (HRV) catalog) in the northwestern part of SLF close to Tuan Giao town, which caused great damage to houses and infrastructure, as well as killing or injuring dozens of people in landslides (Thuy, 2005). The epicenters of these events are shown in Figure 1.2 with focal mechanisms of the 1983 Tuan Giao earthquake, the 2009 Muong La earthquake (Mw3.6, Giang, 2011), and the 2010 Sop Cop earthquake (Mw4.8, HRV) and presented in Appendix.

The 1983 Tuan Giao earthquake, the largest event in the SLF zone, showing strike-slip focal mechanism occurred at the distance of 11 km from Tuan Giao town in the north direction. The discontinued cracks with the width of 10 - 15 cm and length of tens to hundreds centimeters occurred on the ground and extended of about 20 km from Pu Nhung to Muong Mun. The epicenter area was about 30 km long in NW-SE direction and about 10 km wide. Strong ground motion with intensity of VIII (MSK scale) was observed in the area of 1500 km^2. Ground shaking with intensity of VII was observed

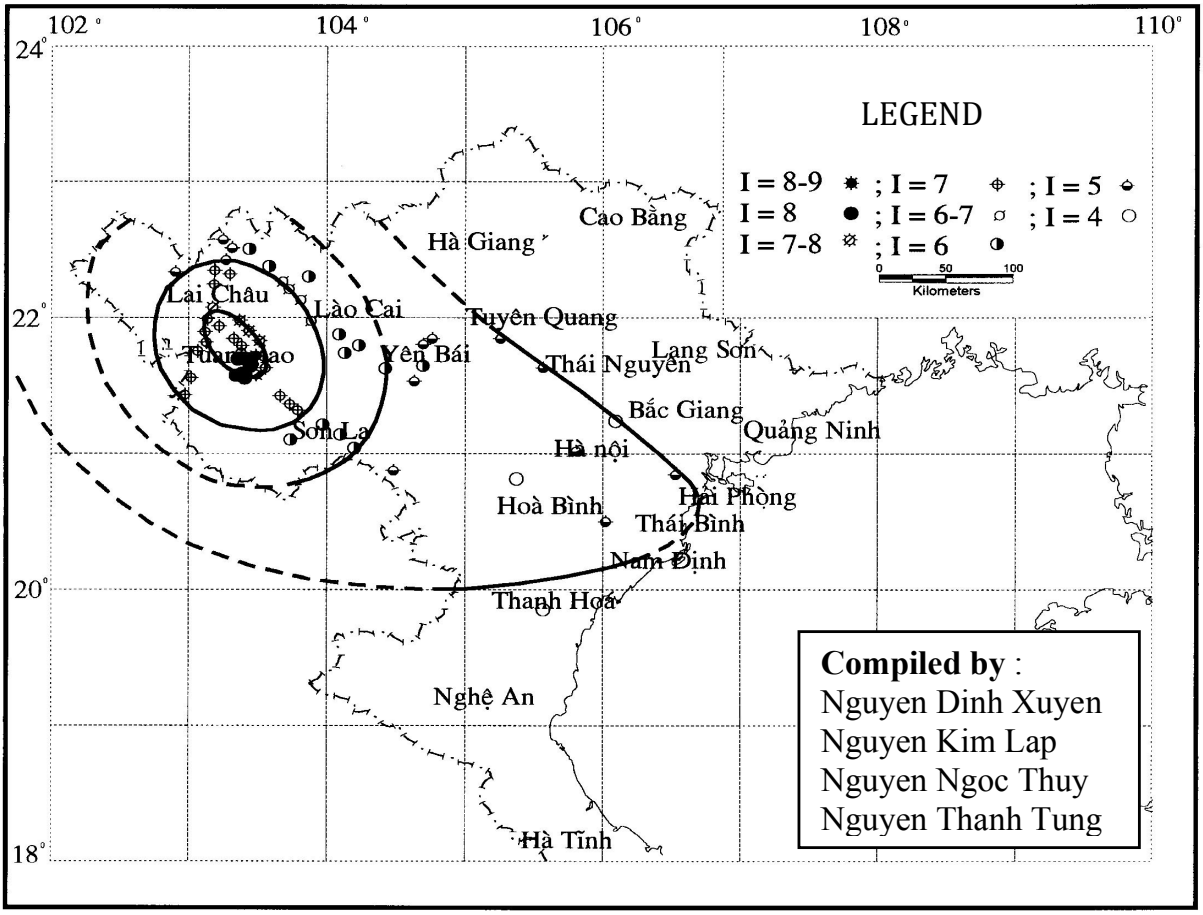

Figure 2.4: Isoseismal map of the Tuan Giao earthquake Mw6.2 on Jun. 24, 1983 (Thuy, 2005)

in the area of 13000 km^2. Figure 2.4 presents the isoseismal map of this earthquake. There were a number of aftershocks of which the strongest event occurred on July 15, 1983 with Ms = 5.1. Field investigations provided data pertaining to seismo-tectonic slip rates in the 1983 Tuan Giao earthquake epicenter area. The maximum observed surface displacement was 44 cm along the NW-SE trending of the SLF zone (Xuyen and Lap, 1985). The recurrence period of such earthquakes in the same area is about 1000 years that is proposed by Xuyen and Thanh (1991). However, the recurrence interval of 1000 years seems quite uncertain.

The recent Dien Bien Phu earthquake of Ms5.3 (Son, 2004) (Mw5.1, Van, 2006) occurred on Feb. 19, 2001. It is the largest observed event occurred in the DBPF zone. The epicenter of the event is located in a mountainous area, at the distance of 20 km from Dien Bien Phu city in southwest direction, near the Laos-Vietnam border within the third segment zone of DBPF. Its focal mechanism reveals the left- lateral strike slip fault (Van, 2006). The shaking with intensity of VII-VIII (MSK-scale) was observed in Dien Bien valley. There were a number of aftershocks of which the strongest had

magnitude up to 4.8. The earthquake damaged almost all masonry structures in the region and injured 10 people but no one was killed. The effects on constructions were quite severe: 130 houses were damaged, 1044 houses needed to be strengthened and 2044 houses were slightly damaged. The event had severe social and economic impact on the people and the local government in the region (Son, 2004). The isoseismal map of this earthquake is presented in Figure 2.5.

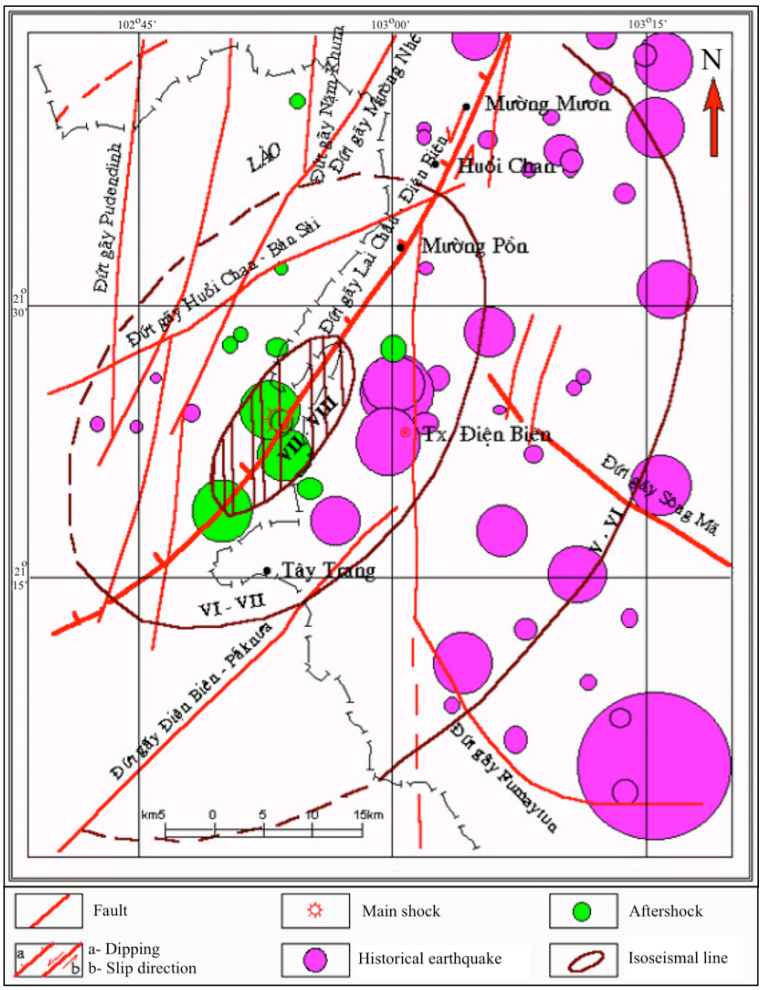

Figure 2.5: Isoseismal map of the Dien Bien earthquake Mw5.1 on Feb. 19, 2001 (Thuy, 2005).

Many earthquakes with intensity of VII on the MSK scale occurred in the study area, such as: Lai Chau in 1914, Dien Bien Phu in 1920, Son La in 1926, Hoa Binh in 1989, Ta Khoa in 1991, Lai Chau in 1993, Muong Luan in 1996 (Son, 2000), and some others in the RRF system. These earthquakes caused strong shaking with intensities of VII and VIII (MSK), and related geological disasters, such as landslides, landcracking and ground deformation on large areas, damaging houses and constructions. Moreover,

in 1989, few months after filling the Hoa Binh reservoir, seismic activity in the zone close to the Hoa Binh dam increased and strong earthquakes occurred (Thuy et al., 1993). The Hoa Binh M4.9 earthquake in 1989 and Ta Khoa M5.1 earthquake in 1991 represented induced earthquakes. That is why great attention should be paid to the phenomena of induced seismicity in the study area.

Earthquakes in the study area occur only in the earth's crust at depths not exceeding 30 km, and maximum focal depths vary in different zones. In the Ma River zone, the focal depth may reach 30 km. In the RRF system, focal depths do not exceed 20 - 25 km. In the remaining zones, focal depths do not exceed 15 - 20 km (Thuy, 2005). The limit of the focal depth is also the limit of the active layer where earthquakes may arise. The thickness of the active layer in different zones, which is estimated by the distribution of earthquakes with depth is therefore variable.

Chapter 3

GPS OBSERVATIONS IN NORTHWESTERN VIETNAM

3.1 Geodetic observation in Northwestern Vietnam before this study

In northern Vietnam investigation on active deformation started in 1963 by installation of the triangulation network of 12 sites spanning the Red River Fault (RRF) system. This network was designed to estimate relative motion as well as strain rates across RRF zone in an extensive as well as comprehensive manner. These sites were occupied with theodolites (Wild T3) by the Geodetic Survey of Vietnam in collaboration with Chinese scientists (Duong and Feigl, 1999). All the markers were concrete structures installed in soil so that they suffered from exogenous impacts. In addition, due to limited accuracy of triangulation measurement, it was not possible to detection of tectonic movements around the fault (Tran, 2001).

Along with technological development in instrumentation as well as data analysis software, GPS has become a common tool for geophysical investigation in 1990's. In Vietnam, a geodetic network of 16 GPS sites covering RRF zone was installed in 1994 to obtain their precise coordinates and their temporal changes. The network has been repeatedly measured since then (Tran, 2001; Vy et al., 2011; Tran et al., 2013).

GPS campaign measurements in northwestern Vietnam (NWV) started in 2001 by Vietnam Institute of Geological Sciences. The GPS network was designed to reveal crustal deformation pattern in the seismically active region. Therefore site locations were selected based on the following criteria; historical earthquake locations, highly populated areas, seismically vulnerable areas with soft soil conditions, and active faults.

11 sites were established in 2001 (DON1, LEM1, NGA1, HAM1, TPU1, LOT1, TCO1, NAH2, MON1, NOI1, NAD1) (Figure 3.1). In 2005, two sites near Hoa Binh city (MHA1 and TSN1) were added to the network. The sites mainly cover geological structures such as the Dien Bien Phu fault (DBPF), the Son La fault (SLF), and the Da River fault (DRF). The GPS network actually consists of two local networks around DBPF and SLF-DRF, respectively, in each of which GPS site spacing is 10 - 50 km. These two local networks are about 100 km apart each other. The SLF-DRF network including 7 sites (TPU1, LOT1, TCO1, NAH2, MON1, NOI1, NAD1) was established across SLF and DRF zones at Son La province. According to Duong et al. (2006), in addition to the 4 sites mentioned above (DON1, LEM1, NGA1, HAM1), there were two other sites, TAU1 and TAU2, in DBPF network. TAU1 was the 4-th order point belonging to the GPS network of Geodetic Survey of Vietnam. The site was unstable since it was not on stable bedrock but on a concrete block with a porcelain mark on top. TAU2 was installed on stable bedrock by a stainless steel cylinder pin of about 10 cm. However, we found on the field that both of these sites were destroyed for building houses in 2009.

Initial results from the local networks located in the DBPF zone (Duong et al., 2006) and SLF-DRF-RRF zones (Tran, 2006) could not reveal a highly confident deformation pattern related with the fault systems. Recently, Lai et al. (2012) combined velocity solutions of Duong et al. (2006) and Shen et al. (2005) to evaluate the deformation of DBPF and reported a slip rate of 2 - 3 mm/yr. This result may be overestimated since the GPS sites used in Shen et al. (2005) are close to the northern segment of RRF or the Xianshuihe - Xiaojiang fault in south China where tectonic deformation is more active than NWV. Thus, a GPS network of higher level of accuracy, spatial resolution and longer time span is required to resolve such small motions of this area.

3.2 GPS observation in this study

As is described in the previous section, the amount of geodetic measurements of crustal deformation in northern Vietnam was limited. Additional GPS measurements in northern Vietnam are therefore essential to better understand tectonic loading processes in NWV, which is the most seismically active region in Vietnam. In addition, tectonic affiliation of NWV has not been thoroughly studied. Thus the intensified GPS network is expected to provide a new insight into large-scale tectonics in Southeast Asia, too. With such scientific objectives in our mind, we construct new GPS sites in NWV and started campaign GPS observation in 2009.

In 2009, besides maintaining the 2001 GPS sites, we deployed an expanded GPS network with new campaign sites concentrated on the SLF-DRF zone. One of the

largest earthquakes (M6.8, Mw6.2) in Vietnam occurred in this area in 1983 (Figure 3.1). Vietnam Institute of Geophysics, in close collaboration with Japanese scientists from Nagoya University, established 9 new sites (PLA1, CUT1, CMA1, MLA1, DTB1, NSA1, CHE1, NAN1, TGA1). The site NAN1 was installed as a replacement of the old sites TAU1 and TAU2. And three sites (MLA1, CHE1, NSA1) were installed in the vicinity of the old sites (TPU1, MON1, LOT1), respectively, considering the risk of future losses of the old sites. The new sites covered the area between the two local networks mentioned above to provide the displacement field over a region of active deformation with an improved spatial resolution. The network is expected to serve for detecting deformation gradients and a better understanding of the physical processes of the deformation in NWV.

Including the pre-existing sites, we deal with 22 GPS campaign sites in total in NWV. The spatial distribution of these sites is based on the geological consideration and the actual accessibility. Figure 3.1 presents the distribution of GPS network in NWV.

Table 3.1: GPS data collected at individual sites in NWV.

Site	2001	2002	2003	2004	2005	2006	2007	2009	2010	2011	2012
DON1		9/24/T4	4/24/T4	4/24/T4					4/24/T5	2/24/T5	2/24/T5
LEM1		9/24/T4	4/24/T4	6/24/T4				3/24/T4	3/24/T4	2/24/T5	
NGA1		5/24/T4	4/24/T4	4/24/T4				3/24/T5	3/24/T5	2/24/T5	2/24/T5
HAM1		9/24/T4	4/24/T4	4/24/T4				6/24/T5	3/24/T5		
TPU1				3/12/T4	4/12/T4			2/24/T5	1/24/T5	2/24/T5	2/24/T5
LOT1	2/12/T4	3/12/T4		3/12/T4	3/12/T4			1/24/T4	2/24/T5	2/24/T5	2/24/T5
NAD1	1/12/T4							2/24/T5	3/24/T4	2/24/T5	2/24/T5
TCO1	4/12/T4							3/24/T5	3/24/T5	2/24/T5	2/24/T5
NAH2					3/12/T4			1/24/T5		2/24/T5	2/24/T5
MON1	3/12/T4	3/12/T4		3/12/T4	3/12/T4			1/24/T5		2/24/T5	2/24/T5
NOI1	3/12/T4	3/12/T4		3/12/T4	3/12/T4			1/24/T4	2/24/T5	2/24/T5	2/24/T5
MLA1								2/24/T5	2/24/T5	2/24/T5	2/24/T5
DTB1								2/24/T4	2/24/T4	3/24/T5	2/24/T5
NSA1								3/24/T5	1/24/T5	2/24/T5	2/24/T5
CHE1								3/24/T5	2/24/T5	1/24/T5	2/24/T5
NAN1								2/24/T4		3/24/T5	2/24/T5
TGA1									2/24/T5	3/24/T5	2/24/T5
CUT1								3/24/T5	2/24/T5	3/24/T5	2/24/T5
CMA1								7/24/T5	2/24/T5	3/24/T5	2/24/T5
PLA1								11/24/T5	10/24/T5	3/24/T5	2/24/T5
MHA1					6/24/T4	4/24/T4	6/24/T4				
TSN1					4/24/T4	4/24/T4	4/24/T4				

(number of sessions/session time in hour/receiver type used*)

(*) receiver type used: T4 - Trimble 4000 SSE/SSI; T5 - Trimble 5700

At these GPS sites, steel benchmarks are installed in bedrock to minimize uncertainties. The benchmarks are 10 cm long steel rods of 1.5 cm diameter with a small hole at their top (1.2 mm diameter by 2 mm deep) that represents the actual measurement point. The top surface of the benchmarks is smooth, with no engraving. The benchmarks have been sealed with cement in deep holes drilled in unweathered and unfractured rock. It was usually not easy to find out good outcrops of rock together with convenient site accessibility, good sky visibility, as well as a location that satisfies the research objectives due to the high mountain study area. For no concrete pillar in the network, we setup a GPS antenna point with a tripod.

For GPS campaign observation, we used Trimble 4000 or 5700 GPS receiver with Permanent L1/L2 or Zephyr Geodetic GPS antennas. These GPS sites have been repeatedly occupied at most once every year. Each GPS site is occupied for 1 to several days in each campaign. We describe detailed occupation of GPS sites in each GPS campaign in the following. GPS data sampling rate is 30 seconds and the elevation mask is 10 degrees throughout. Result is a unique GPS data set of 22 campaign sites in total spanning from 2001 to 2012 used in this study to comprehend the present-day tectonic deformations in NWV.

Besides the 22 sites established since 2001, there were a number of sites created as auxiliary ones or even as main ones. However, for some reason they were lost or unable to continue to observe after few measurements. Data from these sites will only be used in data processing along with that of the 22 sites in order to receive daily coordinate solutions. Each GPS field campaign is presented below. Details of the GPS campaign data of 22 sites are summarized in Table 3.1.

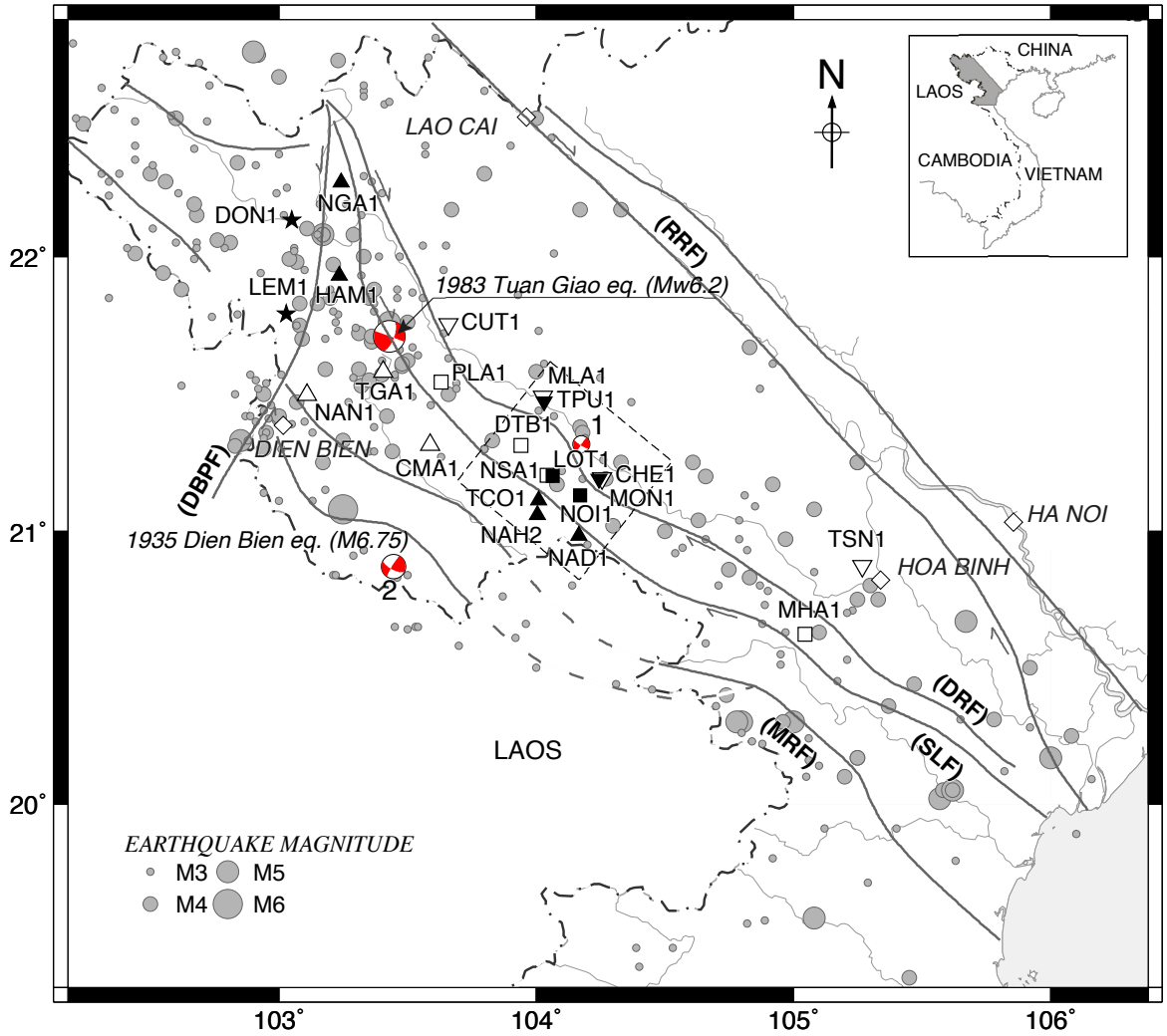

Figure 3.1: GPS sites and seismicity map of NWV. Symbols (squares, triangles, inverted triangles and stars) that are classified in Figure 6.8 show GPS sites. The black solid symbols denote the sites with long observation, and the white solid symbols are sites with short observation spans (Table 3.1). Earthquakes with local magnitude 3.0 - 6.8 occurred from 1903 to April 2012 along the fault zones and their vicinities. The focal mechanisms are of the 1983 Tuan Giao earthquake Mw6.2; (1) the 2009 Muong La earthquake Mw3.6; (2) the 2010 Sop Cop earthquake Mw4.8. Thick solid and dashed lines depict the main fault systems. Thin lines indicate the permanent rivers and the coast of Vietnam. The small box denotes the location of the study area in Vietnam. Star symbols show the cities of Vietnam. Rectangle with dashed line shows profiles of the GPS sites in Figure 7.4.

3.3 Details specific to individual GPS campaigns in NWV

2001 GPS campaign

The 2001 GPS campaign was implemented in late 2001 and lasted until early next year. There were 3 teams on the field. Each team was equipped with a Trimble 4000 SSI receiver and a Compact L1/L2 with ground plane antenna. The sites (NOI1, LOT1, MON1, TCO1, QTA2, NAD1, NAD2 and TPU2) of SLF-DRF network were measured according to the schedule indicated in Table 3.2. It had originally planned to measure NAD2 as a main site and NAD1 as an auxiliary one. However, NAD2 as well as QTA2 and TPU2 were destroyed for building houses, so that we use NAD1 as main site and it is still maintained. The daily sessions lasted about 12 hours (from 00:00 to 12:00 UTC).

Table 3.2: Measurement campaign schedule (2001 GPS field campaign).

Year	Session	NOI1	LOT1	MON1	TCO1	NAD1	NAD2	QTA2	TPU2
2001	362	x		x		x			
	363			x			x	x	
	364			x			x		
2002	1				x			x	x
	2	x			x				x
	3		x		x				x
	4	x	x					x	
	5				x		x		

2002 GPS campaign

There were 3 GPS campaigns deployed in early and late 2002. First (session 54 - 58) and third (session 318 - 325) campaigns were implemented in DBPF network and remain one (session 262 - 269) was in SLF - DRF network. Four Trimble 4000 SSI and a Trimble 4000 SSE receivers with Compact L1/L2 with ground plane antennas were used for the first campaign. Another campaigns were prepared three Trimble 4000 SSI receivers with the same type of antennas. The daily sessions lasted about 12 hours and 24 hours for the sites in SLF-DRF network and DBPF network, respectively. We did not have data on session 265 of second and 322 of third campaigns due to time transferring of teams between the sites.

Table 3.3: Measurement campaign schedule (2002 GPS field campaign).

Site	Session																		
	54	55	56	57	58	262	263	264	266	267	268	269	318	319	320	321	323	324	325
HAM1	x	x	x	x	x										x	x	x	x	
LEM1	x	x	x	x	x											x	x	x	x
NGA1	x	x	x	x	x														
DON1	x	x	x	x	x								x	x	x	x			
TAU1													x					x	x
TAU2	x	x	x	x	x														
TAT1													x	x			x		
NOI1							x				x	x							
LOT1								x	x			x							
MON1									x	x	x								
QTA2						x				x		x							
NAD2									x	x	x								
NAH1						x	x	x											
TPU2						x	x	x											

2003 GPS campaign

The 2003 GPS campaign was decided to remeasure the sites installed along DBPF. The campaign had four full days to observe by Trimble 4000 SSI receivers and Compact L1/L2 with ground plane antennas.

Table 3.4: Measurement campaign schedule (2003 GPS field campaign).

Session	HAM1	LEM1	NGA1	DON1	TAU2
51	x	x	x	x	x
52	x	x	x	x	x
53	x	x	x	x	x
54	x	x	x	x	x

2004 GPS campaign

There were 2 GPS campaigns deployed in early 2002. First campaign (session 41 - 48) was implemented at the sites located in SLF and DRF zones. In this campaign, Trimble 4000 SSI receivers and Compact L1/L2 with ground plane antennas were used

for all 12-hour sessions. After the end of the first trip about 10 days, second campaign was started from session 58 to 65 in DBPF network. Four Trimble 4000 SSI and a Trimble 4000 SSE receivers with Compact L1/L2 with ground plane antennas and only 1 Micro Centered L1/L2 with Ground Plane antenna were used for the this campaign. The daily sessions lasted about 24 hours for the sites in DBPF network. We did not have data on session 44 of first and 62 of second campaigns due to transferring of teams between the sites.

Table 3.5: Measurement campaign schedule (2004 GPS field campaign).

Site	Session													
	41	42	43	45	46	47	48	58	59	60	61	63	64	65
HAM1								x	x	x	x			
LEM1								x	x	x	x	x	x	
NGA1								x	x	x	x			
DON1								x	x	x	x			
TAU2								x	x	x	x			x
TAU1												x	x	x
TAT1												x	x	x
NOI1	x				x		x							
LOT1		x		x			x							
MON1				x	x	x								
TPU1	x	x	x											
QTA2			x			x	x							
NAD2				x	x	x								
NAH1	x	x	x											

2005 GPS campaign

In fact, there was only one GPS campaign deployed in the SLF-DRF network in late 2005. The data measured at MHA1 and TSN1 sites were supported by research project (ID: 105.09.48.09) from the National Foundation for Science and Technology Development of Vietnam. These sites were installed in SLF and DRF zones but about 100 km further east from the SLF - DRF network (Figure 3.1). They are close to the RRF zone, especially TSN1 site about 30km from the fault. Including these sites in NWV GPS network, we will have a general visualization of tectonic deformation between SLF - DRF and RRF zone, although they were measured in different campaigns. Trimble 4000 SSI receivers and Compact L1/L2 with ground plane antennas were used for all sessions in Table 3.6. The daily sessions lasted about 12 hours for the sites in SLF - DRF network and about 24 hours for MHA1 and TSN1 sites.

Table 3.6: Measurement campaign schedule (2005 GPS field campaign).

Session	NOI1	LOT1	MON1	TPU1	NAH2	QTA2	NAD2	HNA1	NAH4	PAV4	MHA1	TSN1
249											x	
250											x	
251											x	
252											x	
254												x
255												x
256												x
257												x
269												x
293												x
326				x				x		x		
327				x	x	x			x			
328	x			x	x				x			
329		x		x	x				x			
330	x		x				x					
331			x			x	x					
332		x	x				x					
333	x	x				x						

2006 and 2007 GPS campaigns

There were only GPS campaigns at MHA1 and TSN1 sites in 2006 and 2007. Trimble 4000 SSI receiver and Compact L1/L2 with ground plane antenna were used for all 24-hour sessions in Table 3.7.

Table 3.7: Measurement campaign schedule (2006 and 2007 GPS field campaigns).

Site	Sessions in 2006								Sessions in 2007									
	105	106	107	108	110	111	112	113	198	199	200	201	203	204	205	206	225	229
MHA1	x	x	x	x					x	x	x	x						
TSN1					x	x	x	x					x	x	x	x	x	x

2009 GPS campaign

The 2009 GPS field campaign was a large survey in NWV. There were 6 teams on the field. Five Trimble 5700 receivers with Trimble Zephyr Geodetic antennas of Nagoya University and one Trimble 4000 SSI receiver with Compact L1/L2 with ground plane

antenna of were used for the this campaign. We remeasured the pre-existing sites in DBPF and SLF-DRF networks. Last campaign of DBPF and SLF-DRF networks was in 2004 and 2005, respectively. An expanded GPS network with new campaign sites (PLA1, CUT1, CMA1, MLA1, DTB1, NSA1, CHE1, NAN1, TGA1) was measured in this campaign according to the schedule indicated in Table 3.8. Three new sites (MLA1, CHE1, NSA1) were intended to take the place of the old sites (TPU1, MON1, LOT1), respectively. Thus the old sites were measured only one full day together with the new ones. The new site PLA1 as a master site of the campaign that located between DBPF and SLF-DRF networks was measured for whole campaign (11 days). The purpose was to constrain the sites in whole network. In this campaign, HAM1 site of DBPF network was measured about 6 hours in session 266 then transferred to MLA1 site of SLF-DRF network. DON2 was observed instead of DON1 as originally planned because of wrong positioning of a GPS team. The daily sessions lasted about 24 hours except session 260 at PLA1 and session 266 at TCO1, MLA1, DTB1 were only about 12 hours due to time transferring of teams between sites.

Table 3.8: Measurement campaign schedule (2009 GPS field campaign).

Site	Session										
	260	261	262	263	264	265	266	267	268	269	270
HAM1		x	x	x	x	x	x				
LEM1		x	x	x							
NGA1		x	x	x							
DON2		x	x	x	x	x					
NAN1					x	x					
PLA1	x	x	x	x	x	x	x	x	x	x	x
CMA1		x	x	x	x	x	x	x			
NOI1											x
NSA1									x	x	x
LOT1									x		
CHE1									x	x	x
MON1											x
NAD1										x	x
TCO1							x	x	x		
NAH2									x		
TPU1								x			
MLA1							x	x			
DTB1							x	x			
CUT1					x	x	x				

2010 GPS campaign

In 2010 GPS campaign, we deployed 5 teams on the field that equipped four Trimble 5700 receivers with Trimble Zephyr Geodetic antennas of Nagoya University and one Trimble 4000 SSI receiver with Compact L1/L2 with ground plane antenna. We installed and measured TGA1 site located close to the 1983 earthquakes (M6.8) in Tuan Giao town and DON3 as an axillary site of DON1. PLA1 as a master site of the campaign was measured for whole campaign (10 days). In this campaign, the daily sessions lasted about 24 hours except session 117 at TCO1, DTB1, CUT1 and MLA1 were only about 12 hours due to transferring between the sites of DBPF network to the sites of SLF-DRF network.

Table 3.9: Measurement campaign schedule (2010 GPS field campaign).

Site	Session									
	112	113	114	115	116	117	118	119	120	121
HAM1	x	x	x							
LEM1		x	x	x						
NGA1	x	x	x							
DON1	x	x	x	x						
NOI1									x	x
LOT1									x	x
NAD1								x	x	x
TCO1						x	x	x		
TPU1								x		
PLA1	x	x	x	x	x	x	x	x	x	x
DTB1						x	x			
CUT1						x	x			
CMA1				x	x					
MLA1						x	x			
CHE1									x	x
NSA1								x		
DON2	x									
TGA1				x	x					
DON3					x					
LEM2					x					

2011 GPS campaign

The 2011 GPS field campaign was implemented with only four Trimble 5700 receivers with Trimble Zephyr Geodetic antennas of Nagoya University. Due to the limited time available and number of equipment for this campaign, each site was measured maximum 3 days, with the exceptions of CHE1 and NSA1 that were measured one day only. On the field, we discovered that HEM1 in DBPF network was lost so that only 3 sites were measured in the first two days of the campaign. The daily sessions lasted about 24 hours except session 58 at PLA1, CUT1, NAN1 and TGA1 were about 15 hours due to time transferring between the sites.

Table 3.10: Measurement campaign schedule (2011 GPS field campaign).

Site	Session									
	56	57	58	59	60	61	62	63	64	65
LEM1	x	x								
NGA1	x	x								
DON1	x	x								
NOI1									x	x
LOT1								x	x	
MON1									x	x
NAD1									x	x
TCO1							x	x		
TPU1							x	x		
NAH2					x	x				
PLA1			x	x	x					
DTB1					x	x	x			
CUT1			x	x	x					
CMA1					x	x	x			
MLA1					x	x				
CHE1										x
NSA1								x		
NAN1			x	x	x					
TGA1			x	x	x					

2012 GPS campaign

The 2012 GPS campaign was implemented quite similar to the 2011 one because of the limited time available and number of equipment. Four Trimble 5700 receivers with Trimble Zephyr Geodetic antennas of Nagoya University were deployed in this campaign. Results, each site was measured 2 days except NAN1 was measured only one day. On the field, we discovered that LEM1 in DBPF network was waterlogged so that it was not measured. We decided to measure DON2 and DON3 together with DON1 (main site), which might be flooded in near future due to Son La hydropower reservoir was filling. The daily sessions lasted about 24 hours except session 59 was about 15 hours. That was the day of transferring between the sites.

Table 3.11: Measurement campaign schedule (2012 GPS field campaign).

Site	Session									
	57	58	59	60	61	62	63	64	65	66
NGA1	x	x								
DON1	x	x								
NOI1									x	x
LOT1							x	x		
MON1									x	x
NAD1									x	x
TCO1					x	x				
TPU1							x	x		
NAH2							x	x		
PLA1			x	x						
DTB1					x	x				
CUT1			x	x						
CMA1					x	x				
MLA1					x	x				
CHE1									x	x
NSA1							x	x		
NAN1				x						
DON2	x	x								
TGA1			x	x						
DON2	x	x								

Chapter 4

GPS DATA PROCESSING

GPS data processing strategies have been already discussed in many studies (e.g., Lichten and Border, 1987; Dach et al., 2011). However, the chosen GPS processing method depends on the software used and varies from campaign to campaign with subjective operations. The software used in this study is the BERNESE Version 5.0 software (Dach et al., 2007) developed at Astronomical Institute, University of Berne, Switzerland. The data processing is followed the standard processing strategy of Dach et al. (2011). In this chapter, we present the data processing strategy that we have adopted for the GPS measurements in NWV.

4.1 Methodology

When estimating coordinates with the BERNESE Version 5.0 software two major processing modes can be distinguished, namely the precise point positioning (PPP) and a differential (relative) mode. PPP is based on precise orbit, undifferenced code and/or phase observations, and clock information. Precise site coordinates and receiver clock corrections independently for each site are then derived. However, the differential mode promises to produce the highest precision for the relative geometry between the sites processed together in a network solution. In a network analysis, the double-differenced observations are utilized to estimate site coordinates. Moreover, the phase ambiguities can only be taken in this relative mode, which is the first choice for obtaining the highest quality results. Thus, in this study, the signal double-differentiation (relative processing) for the calculation of regional sized network is adopted.

By following the standard processing strategy (Dach2011), 26 IGS sites SELE, BUCU, NICO, POLV, KUNM, WUHN, IRKT, TNML, TRAB, ZECK, DARW, KARR, ALIC, CEDU, TIDB, BAKO, COCO, DAEJ, DGAR, GUAM, IISC, LHAZ, NTUS,

PIMO, SHAO, TSKB distributed around the study area are included in our processing as well. IGS final orbits, CODE global ionosphere models, IERS Earth Orientation Parameters and ocean tide loading corrections (http://froste.oso.chalmers.se/loading/) are used. We use Saastamoinen model (Saastamoinen, 1972), one of the most popular models, together with the Niell mapping function (Niell, 1996) to compute the tropospheric refraction. The geometry of the network relative to daily measurement sessions is chosen with the aim of maximizing the simultaneous observations among sites. The QIF (quasi-ionosphere-free) strategy is chosen to resolve the ambiguities in baseline processing. The program ADDNEQ2 is used to stack normal equation files to produce daily site coordinates.

In general, it is not possible to estimate the absolute position of all stations. Some of them (at least one) have to be kept fixed on their priori positions. Free network conditions (or minimum constraint conditions) are optimal to define the geodetic datum with a minimum number of constraints, without fixing or constraining particular site coordinates. This minimum constraint approach is well suited to analyze inconsistencies in the reference site coordinates. Minimum constraint conditions are based on the assumption that there are two reference frames: a priori reference frame, and a reference frame of the resulting coordinates. Both reference frames are related to each other by computing the translations of the barycenter of the resulting reference site coordinates (the latter) with respect to the barycenter of the a priori reference site coordinates (the former). In this study, coordinates of the first 15 IGS sites listed above, which are not affected by large earthquakes, are used to constrain the solution in ITRF2008 (Altamimi et al., 2011). Coordinates of other IGS sites are estimated with the local sites.

Each GPS site was occupied for 1 to 11 sessions in each campaign. Thus we calculate mean campaign coordinates and its standard deviations from daily coordinate solutions for each site. For a campaign with only 1 session, we assume standard deviation of the campaign coordinate is that of daily coordinate solution. In our analysis, we assume the eastward and northward components of a site's velocity to be independent. Finally, horizontal velocities and their standard deviations are estimated by the least squares method by assuming white noise model errors (Zhang et al., 1997). There have been many studies demonstrating the importance of colored noise for the estimation of velocity uncertainties. Zhang et al. (1997) pointed out velocity uncertainties with a colored noise model become larger by a factor of 2 - 6 than those with a white noise model. However, we cannot adequately distinguish a specific noise model for a temporally sparse campaign GPS data set. Thus, the velocity errors in this study may be a little optimistic.

4.2 Error estimate for velocity

The linear regression problem for determining velocities can be expressed as fitting a straight line through a series of N points x_i taken at times t_i:

$$x_i = x_0 + rt_i + \varepsilon_x(t_i) \tag{4.1}$$

where x_0 and r are x-intercept and slope of the line; $\varepsilon_x(t_i)$ is the error term. The slope is a velocity component of a GPS site.

Zhang et al. (1997) derived equations for the variance of the x-intercept and slope when the error term only consists of white noise or random walk noise. While, Williams (2003) derived the variance of slope and offset when the error term consists of white noise or random walk noise and offsets in coordinate-time series. Consider the simplest case where there is one offset (assuming coseismic offset) at time t_{off} ($t_1 < t_{off} < t_N$) in the coordinate-time series. Equation (4.1) now becomes

$$x_i = x_0 + rt_i + p_i x_{off} + \varepsilon_x(t_i) \tag{4.2}$$

where

$$p_i = \begin{cases} 1 & t_i \geq t_{off} \\ 0 & t_i < t_{off} \end{cases}$$

Equation (4.2) may be written in the matrix form

$$\mathbf{x} = \mathbf{A}\widehat{\mathbf{y}} + \boldsymbol{\varepsilon} \tag{4.3}$$

where

$$\mathbf{x} = (x_1, ..., x_N)^T$$

$$A = \begin{bmatrix} 1 & t_1 & p_1 \\ 1 & t_2 & p_2 \\ \vdots & \vdots & \vdots \\ 1 & t_N & p_N \end{bmatrix}$$

$$\widehat{y} = (\widehat{x}_0, \widehat{r}, \widehat{x}_{off})^T$$

$$\boldsymbol{\varepsilon} = (\varepsilon_1, ..., \varepsilon_N)^T$$

Fitting a straight line to the coordinate-time series by weighted least squares ap-

proach, the x_0, r and x_{off} are obtained from

$$\widehat{\mathbf{y}} = [\mathbf{A}^T\mathbf{C}_x^{-1}\mathbf{A}]^{-1}\mathbf{A}^T\mathbf{C}_x^{-1}\mathbf{x} \tag{4.4}$$

with a covariance matrix

$$\widehat{\mathbf{C}}_{\widehat{\mathbf{y}}} = [\mathbf{A}^T\mathbf{C}_x^{-1}\mathbf{A}]^{-1} \tag{4.5}$$

where $\mathbf{C}_x$ is the covariance matrix of the measurements x_i.

In this study, we consider the case of the uncorrelated measurement errors (white noise). Thus we can express the covariance matrix of the measurements x_i as

$$\mathbf{C}_x = a^2\mathbf{I} \tag{4.6}$$

where $\mathbf{I}$ is identity matrix of dimension N; a is the magnitude of white noise. The covariance matrix for the estimates is given by

$$\widehat{\mathbf{C}}_{\widehat{\mathbf{y}}} = a^2 \begin{bmatrix} N & \sum_{i=1}^N t_i & \sum_{i=1}^N p_i \\ \sum_{i=1}^N t_i & \sum_{i=1}^N t_i^2 & \sum_{i=1}^N p_i t_i \\ \sum_{i=1}^N p_i & \sum_{i=1}^N p_i t_i & \sum_{i=1}^N p_i^2 \end{bmatrix}^{-1} \tag{4.7}$$

and

$$\widehat{\mathbf{C}}_{\widehat{\mathbf{y}}} = \begin{bmatrix} \sigma_{x_0}^2 & \sigma_{x_0 r} & \sigma_{x_0 x_{off}} \\ \sigma_{x_0 r} & \sigma_r^2 & \sigma_{r x_{off}} \\ \sigma_{x_0 x_{off}} & \sigma_{r x_{off}} & \sigma_{x_{off}}^2 \end{bmatrix} \tag{4.8}$$

In case of equally spaced data, we have such that

$$t_i = (i-1) \triangle T; \quad T = (N-1) \triangle T \tag{4.9}$$

where $\triangle T$ is the sampling interval, and T is the total observation span. From (4.7), (4.8) and (4.9), the variance of the estimate velocity is

$$\sigma_{\hat{r}}^2 = \frac{12a^2}{\triangle T^2 N(N^2 - 3NM + 3M^2 - 1)} \tag{4.10}$$

where $M = \sum_{i=1}^N p_i$. Using (4.9) for N$\gg$1, equation (4.10) is similar to the velocity error without offsets in coordinate-time series (Zhang et al., 1997), which is

$$\sigma_{\hat{r}}^2 \cong \frac{12a^2}{NT^2} \tag{4.11}$$

The variance of the offset is

$$\sigma^2_{\widehat{x}_{off}} = \frac{a^2 N(N^2-1)}{M(N^3 - N - 4N^2M + 6NM^2 - 3M^3 + M)} \tag{4.12}$$

If the offset is situated in the center of the coordinate-time series, then $M = N/2$ and equations (4.10) and (4.12) are simplified to

$$\sigma^2_{\widehat{r}} = \frac{48a^2}{\triangle T^2 N(N-2)(N+2)} \tag{4.13}$$

$$\sigma^2_{\widehat{x}_{off}} = \frac{16a^2(N^2-1)}{N(N^2-4)} \tag{4.14}$$

Using (4.9) for large N, equation (4.13) is such that

$$\sigma^2_{\widehat{r}} \cong \frac{48a^2}{NT^2} \tag{4.15}$$

Comparing (4.11) and (4.15), the velocity uncertainty for a coordinate-time series with an offset is double of the uncertainty for the coordinate-time series without the offset. From (4.14), the offset uncertainty is independent of the total observation span (T), so this equation is used to analyze the uncertainty of coseismic offset.

Chapter 5

ESTIMATE OF FAR-FIELD COSEISMIC DISPLACEMENTS AND TIME-SERIES CORRECTIONS

5.1 Introduction

During the GPS campaigns in NWV spanning from 2001 to 2012, three great earthquakes occurred: the 26 December 2004 M9.1 Sumatra earthquake (e.g., Lay et al., 2005), the 12 May, 2008, M 7.9 Wenchuan earthquake (e.g., Burchfiel et al., 2008), and the 11 March 2011 M9.0 Tohoku earthquake (e.g., Simons et al., 2011). These earthquakes occurred at about 2000 km, 1000 km, and 4000 km distance from the study area, respectively, if we refer to epicenters.

The 2004 Sumatra earthquake ruptured at least 1200 km of the megathrust along the plate boundary between the Indian - Australian plate the Eurasian plate. Its epicenter was located at the southernmost end of the source region. Thus, the actual distance from the study area to the earthquake source was shorter (about 1500 km).

While, the 2011 Tohoku earthquake is the largest seismic event occurred after the 2004 Sumatra earthquake. This event occurred near the northeastern coast of Honshu Island, Japan, as a result of thrust faulting caused by the Pacific plate subduction beneath the Japan Island Arc. The fault rupture is characterized by a compact region of high-slip of about 450 km long and about 200 km wide localized near the trench with a large maximum slip up to 60 m (e.g., Ito et al., 2011; Shao et al., 2011; Yagi and

Fukahata, 2011; Yoshida et al., 2011; Gusman et al., 2012).

Based on GPS observation as well as dislocation model for a spherical body, far-field coseismic offsets produced by these earthquakes at distances thousands of kilometers away from the earthquake rupture were shown to be over 1 mm (e.g., Banerjee et al., 2005; Kreemer et al., 2006; Pollitz et al., 2011). Therefore, the effect of these distant giant earthquakes must be considered to discuss crustal deformation in NWV where tectonic deformation rate is not high, especially, it was not taken in the previous studies. The coseismic offsets due to those earthquakes are calculated and to offset the time-series. Then we calculate the velocity of each GPS site in the ITRF2008 reference frame based on the corrected time-series.

5.2 Methodology and modeling

The GPS sites in NWV have been observed three or more years, thereby their velocities are considered to be free from the effect of seasonal and long period noise (Blewitt and Lavallée, 2002). On the other hand, the impact of the far-field coseismic displacements caused by the 2004 Sumatra, the 2008 Wenchuan, and the 2011 Tohoku earthquakes may be significant. So we estimate displacements caused by these earthquakes at the GPS sites using static fault models of these earthquakes.

Many distant IGS sites throughout the Southeast Asia recorded a measurable coseismic signal of the 2004 Sumatra earthquake. Chlieh et al. (2007) distinguished between far-field (300 - 1100 km) and very-far-field (>1100 km) data because the effect of the Earth's stratification and sphericity becomes significant typically beyond about 1100 km (Banerjee et al., 2005). Similarly, Shestakov et al. (2012) recognized that the predicted offset magnitudes underestimated by a factor of 1.5 - 2 at the far-field sites without adopting of the spherically layered isotropic medium approach (Pollitz, 1996). Considering the distance between the source fault and the GPS sites in NWV, we applied an elastic dislocation model for a layered spherical earth model developed by Pollitz (1996).

We assume physical properties for each layer of the spherical earth model based on the Preliminary Reference Earth Model (PREM) (Dziewonski and Anderson, 1981) as shown in Figure 5.1.

As for the source fault model, a large number of models have been proposed for the 2004 Sumatra earthquake (e.g., Ammon et al., 2005; Banerjee et al., 2005; Lay et al., 2005; Tsai et al., 2005; Vigny et al., 2005; Kreemer et al., 2006) and the 2011 Tohoku earthquake (e.g., Hayes, 2011; Ide et al., 2011; Nishimura et al., 2011; Ozawa

et al., 2011; Pollitz et al., 2011; Sato et al., 2011; Shao et al., 2011; Wang and Mori, 2011; Yagi and Fukahata, 2011; Yoshida et al., 2011; Gusman et al., 2012) based on the geodetic, seismic waves, ocean-bottom pressure gauges and tsunami waveform data. The models more or less adequately explain coseismic displacements observed in the near-field zone. Only few studies computed coseismic displacements from their models were then compared with the observed ones at a sparse GPS network of far-field sites (Banerjee et al., 2005; Kreemer et al., 2006; Pollitz et al., 2011). Applying a different fault model naturally gives different coseismic deformations. In this study, we selected source fault models whose model parameters about rupture size and slip distribution are digitally available; moreover, utilize the observed coseismic displacements at far-field GPS sites to compare with the predicted ones. With such a criterion, we chose a rupture model D of Kreemer et al. (2006) for the 2004 Sumatra earthquake. The rupture model was inferred from the far-field continuous GPS data. This model is different from that of Banerjee et al. (2005) who had a similar study using far-field data. According to Kreemer et al. (2006), the main difference is that they found a much lower slip on the northern rupture segment, which is more consistent with seismic studies (e.g., Ammon et al., 2005; Lay et al., 2005).

In contrast to the Sumatra region, a dense high-rate (1- Hz) GPS network of the GPS Earth Observation Network (GEONET) covered main islands of Japan that is operated by the Geospatial Information Authority of Japan (GSI) (Sagiya et al., 2000) have been detecting coseismic and postseismic displacements for many earthquakes since 1994, as well as the 2011 earthquake (Ozawa et al., 2011). GEONET has also revealed plate motions and interseismic deformation along the plate boundaries (e.g., Sagiya, 2004). Before the 2011 Tohoku earthquake, a contraction in the east-west direction was observed in northeastern Japan (Sagiya et al., 2000) and the plate interface was considered to be locked along the Japan Trench (e.g., Nishimura et al., 2004). Thus, a huge set of GPS data from GEONET was used by different organizations and researchers for updating the source model of this seismic event (e.g., Iinuma et al., 2011; Ito et al., 2011; Miyazaki et al., 2011; Nishimura et al., 2011; Ozawa et al., 2011; Pollitz et al., 2011; Yue and Lay, 2011; Gusman et al., 2012). Besides the source fault models obtained using GPS data, there are many other models based on inversion of seismic wave data (e.g., Hayes, 2011; Ide et al., 2011; Shao et al., 2011) or combinations of different techniques (Ammon et al., 2011; Koketsu et al., 2011; Koper et al., 2011; Simons et al., 2011; Gusman et al., 2012).

Finally, we utilized a model of Gusman et al. (2012) for the 2011 Tohoku earthquake. The rupture model was inverted from tsunami waveforms, GPS data, and seafloor crustal deformation data. The simulated tsunami waveforms from the source model fit well with the observed ones at Deep-ocean Assessment and Reporting of Tsunamis

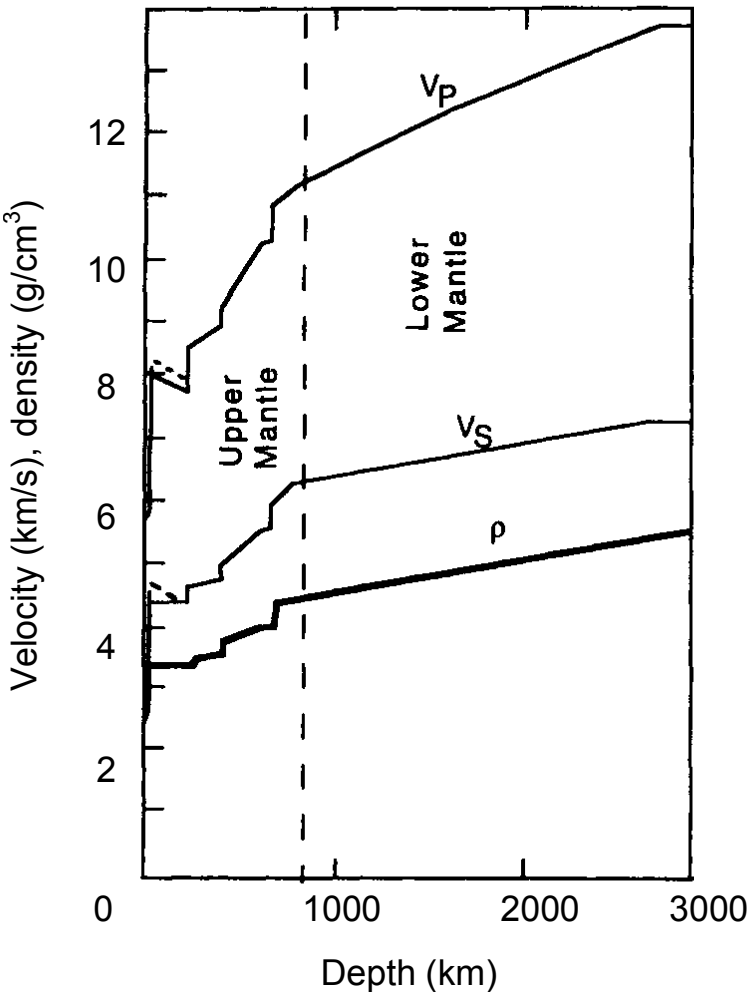

Figure 5.1: The Preliminary Reference Earth Model (PREM) of P velocity (V_p), S velocity (V_s), and density (ρ) as a function of depth (up to lower Mantle) in the Earth. Dashed lines are the horizontal components of velocity. (Dziewonski and Anderson, 1981).

(DART) buoys that are located offshore and across the Pacific Ocean. Some of buoys can be considered as far-field even very far-field sites from the epicenter.

Similarly to the 2004 Sumatra and the 2011 Tohoku earthquakes, the source fault model of the 2008 Wenchuan earthquake have been proposed by a large number of studies, using the GPS, InSAR, seismic wave data, or combinations of such different techniques (e.g., Ji and Hayes, 2008; Hao et al., 2009; Shen et al., 2009; Feng et al., 2010; Nakamura et al., 2010; Tong et al., 2010; Xu et al., 2010; Zhang et al., 2011; Fielding et al., 2013). We use the source model for joint geodetic-teleseismic slip of Fielding et al. (2013) for the 2008 Wenchuan earthquake.

5.3 Results and Discussion

5.3.1 Estimate of far-field coseismic displacements

We estimate far-field coseismic offsets at GPS sites in NWV from the 2004 Sumatra, the 2008 Wenchuan, and the 2011 Tohoku earthquakes using the respective fault models. The results are listed in Table 5.1. Calculated horizontal displacements show that the 2004 Sumatra earthquake caused southwestward movements by about 15 mm in NWV. Meanwhile, the 2011 Tohoku earthquake produced displacements in the opposite directions, approximately 1.2 mm to the east and 0.5 mm to the north, in the same region. The difference in amplitude of coseismic displacements can be attributed to the distance from each source fault to the study area. Moreover, according to previous studies, the region covering the measurable coseismic displacements caused the 2011 Tohoku earthquake is smaller than that affected by the 2004 Sumatra earthquake. Pollitz et al. (2011) presented coseismic offsets of ∼3 - 5 mm at distances as far as 3000 to 4000 km from the rupture of the 2011 Tohoku earthquake. Meanwhile, coseismic displacements of 5 - 10 mm were detected at GPS sites located more than 3000 km away from the 2004 Sumatra earthquake epicenter (Banerjee et al., 2005; Vigny et al., 2005; Kreemer et al., 2006).

The horizontal displacements in NWV from the 2008 Wenchuan earthquake are smaller than 1 mm, so they are negligible. Therefore, only the calculated coseismic offsets caused by the 2004 Sumatra and the 2011 Tohoku earthquakes are hereinafter taken into consideration.

5.3.2 Time-series correction for far-field coseismic displacements at GPS sites in NWV

According to the calculations in the previous section, the far-field coseismic displacements caused by the 2004 Sumatra and the 2011 Tohoku earthquakes are significant in NWV. We use the predicted far-field coseismic offsets caused by these earthquakes at GPS sites in NWV (Table 5.1) to correct these from original GPS time-series, and estimate an average displacement rate for the corrected time-series.

The east and north campaign positions for the observation span for the sites in NWV are shown in Figure 5.2. There are three groups of the campaign positions presented: the campaign positions without removing the predicted coseismic offsets of the earthquakes; the campaign positions after the 2004 Sumatra earthquake with removing the predicted coseismic offsets caused by this event; and the campaign positions after

Table 5.1: The predicted horizontal far-field coseismic displacements caused by the 2004 Sumatra, the 2008 Wenchuan, and the 2011 Tohoku earthquakes at the GPS sites in Northwestern Vietnam.

Site	Lon. (°E)	Lat. (°N)	The 2004 Sumatra eq.		The 2008 Wenchuan eq.		The 2011 Tohoku eq.	
			Δ_{east} (mm)	Δ_{north} (mm)	Δ_{east} (mm)	Δ_{north} (mm)	Δ_{east} (mm)	Δ_{north} (mm)
DON1	103.051	22.131	-8.3	-10.3	-0.2	-0.9	1.2	0.5
LEM1	103.029	21.792	-8.8	-10.8	-0.2	-0.8	1.2	0.5
NGA1	103.242	22.268	-8.2	-10.1	-0.2	-0.9	1.2	0.5
HAM1	103.236	21.931	-8.7	-10.6	-0.2	-0.8	1.2	0.5
NAN1	103.108	21.497	-9.4	-11.3	-0.2	-0.8	1.1	0.5
TGA1	103.405	21.582	-9.4	-11.1	-0.1	-0.8	1.2	0.5
CUT1	103.660	21.754	-9.2	-10.7	-0.2	-0.7	1.2	0.5
PLA1	103.631	21.542	-9.6	-11.0	-0.1	-0.7	1.2	0.5
CMA1	103.588	21.314	-10.0	-11.4	-0.1	-0.7	1.1	0.5
TPU1	104.031	21.473	-9.9	-11.0	-0.1	-0.6	1.2	0.5
MLA1	104.026	21.489	-9.9	-11.0	-0.1	-0.6	1.2	0.5
DTB1	103.942	21.312	-10.2	-11.3	-0.1	-0.6	1.2	0.5
LOT1	104.064	21.203	-10.5	-11.4	-0.1	-0.6	1.2	0.5
NSA1	104.044	21.204	-10.5	-11.4	-0.1	-0.6	1.2	0.5
TCO1	104.011	21.113	-10.6	-11.5	-0.1	-0.6	1.1	0.5
NAH2	104.005	21.059	-10.7	-11.6	-0.1	-0.6	1.1	0.5
MON1	104.245	21.189	-10.6	-11.3	-0.1	-0.6	1.2	0.5
CHE1	104.257	21.192	-10.6	-11.3	-0.1	-0.6	1.2	0.5
NOI1	104.172	21.131	-10.7	-11.4	-0.1	-0.6	1.1	0.5
NAD1	104.166	20.983	-11.0	-11.6	-0.1	-0.6	1.1	0.5
MHA1	105.045	20.624	-11.9	-11.5	-0.1	-0.4	1.1	0.5
TSN1	105.269	20.872	-11.5	-11.0	-0.1	-0.4	1.2	0.5
	Average		*-10.0*	*-11.1*	*-0.1*	*-0.7*	*1.2*	*0.5*

the 2011 Tohoku earthquake with removing the predicted coseismic offsets caused by the both earthquakes (Figure 5.2- a,b). We fit a straight line to the corrected coordinate-time series by the least squares approach then velocity of GPS site is estimated. We use the velocity to detrend all the data of the site (Figure 5.2- c,d). From this figure we can see that the impact of the 2011 Tohoku earthquake to NWV is insignificant compared with the 2004 Sumatra earthquake.

Velocities over a period of 2001 - 2012 and their 1-σ uncertainties are presented in Table 5.2. The velocity uncertainties are determined from the equation (4.11) in chapter 4 with assuming without any coseismic offsets in the coordinate-time series.

In Table 5.2, we compare the velocity estimates with and without the corrections

of the two large earthquakes. From this result, offsets of the 2004 Sumatra earthquake affect the velocity estimate by 1.1 ± 0.2 mm/yr for the east and 1.2 ± 0.2 mm/yr for the north components. On the other hand, effects of the 2011 Tohoku earthquake on velocity estimate are minor, causing velocity change of 0.3 ± 0.2 mm/yr and 0.1 ± 0.1 mm/yr for the east and north components, respectively. 1-σ uncertainties for the velocity components are mostly less than 0.5 mm/yr at the GPS sites observed for 4 years or more. Other sites with shorter observation time or with low data quality due to measurement problems have larger uncertainties, but still less than 1.0 mm/yr, which is precise enough for discussing tectonic deformation.

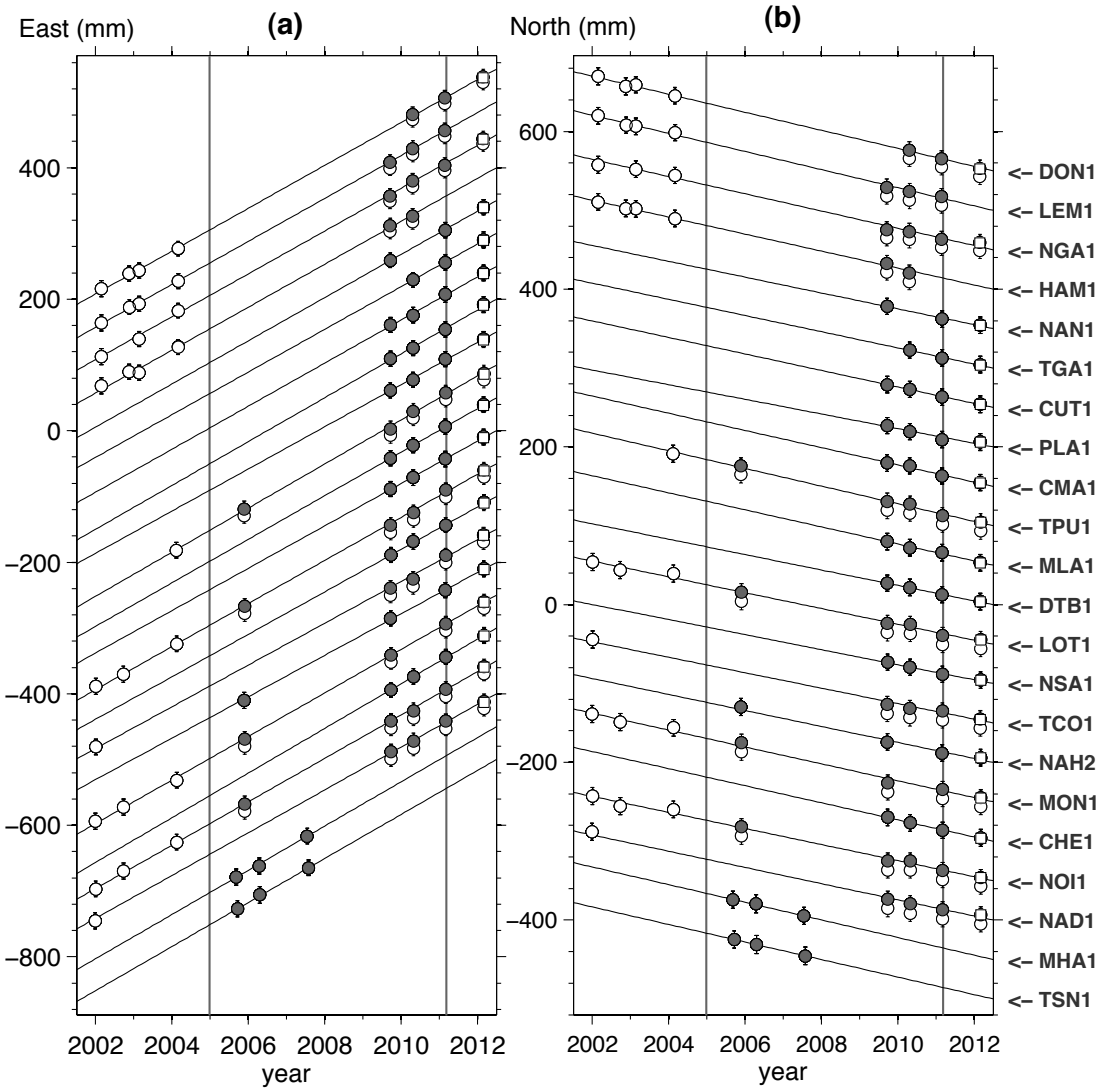

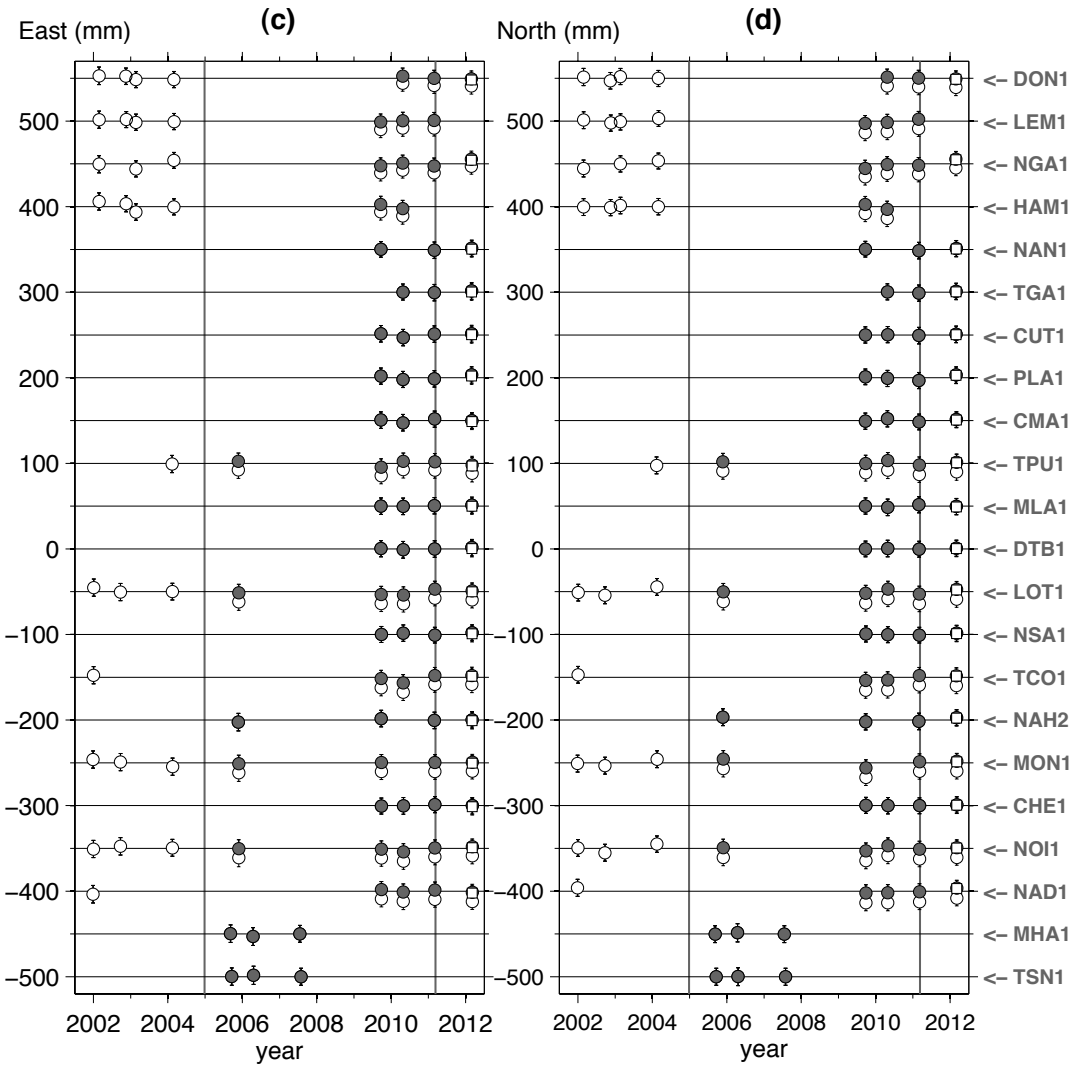

Figure 5.2: Horizontal coordinate-time series (a, b); time series after removing the linear trend (c, d) of GPS sites (named on right side of black solid lines) in NWV in ITRF2008. Vertical solid lines mark the 2004 Sumatra and the 2011 Tohoku earthquakes. Open circles denote the positions of the east and north components before removing the predicted far-field coseismic offsets of these earthquakes. Solid circle shows the positions after removing the predicted far-field coseismic offsets caused by the 2004 Sumatra earthquake. Open rectangle shows the positions after removing the predicted far-field coseismic offsets caused by both earthquakes. At the figure scale, Solid circles are covered by open rectangles after 2011. It means that the impact of the 2011 Tohoku earthquake to NWV is insignificant compared with the remaining one. Black solid lines are the best fitting lines for temporal changes of the horizontal coordinates with the correction of the coseismic offsets of the earthquakes. The coordinate uncertainties are shown 95% confidence level.

Table 5.2: GPS velocities in ITRF2008 reference frame and their 1σ uncertainties with-/without the correction of coseismic offsets for the 2004 Sumatra and the 2011 Tohoku earthquakes at the GPS sites in NWV (mm/yr).

Site	Uncorrected velocity				Velocity corrected for the 2004 Sumatra earthquake				Final corrected velocity (corrected for all earthquakes)			
	V_E	V_N	σ_E	σ_N	V_E	V_N	σ_E	σ_N	V_E	V_N	σ_E	σ_N
DON1	31.6	-12.6	0.2	0.1	32.7	-11.3	0.2	0.1	32.6	-11.4	0.2	0.1
LEM1	31.4	-13.0	0.2	0.3	32.6	-11.5	0.2	0.2	32.6	-11.5	0.2	0.2
NGA1	31.5	-12.2	0.4	0.4	32.6	-10.8	0.3	0.3	32.6	-10.9	0.3	0.3
HAM1	31.5	-12.1	0.5	0.2	32.8	-10.6	0.5	0.2	32.8	-10.6	0.5	0.2
NAN1	32.6	-10.1	1.0	0.7	32.6	-10.1	1.0	0.7	32.3	-10.2	1.0	0.6
TGA1	32.8	-10.0	0.7	0.8	32.8	-10.0	0.7	0.8	32.2	-10.3	0.5	0.7
CUT1	33.1	-10.0	1.0	0.5	33.1	-10.0	1.0	0.5	32.8	-10.1	0.9	0.5
PLA1	32.6	-10.5	0.6	0.6	32.6	-10.5	0.6	0.6	32.3	-10.6	0.6	0.6
CMA1	32.2	-10.6	0.7	0.8	32.2	-10.6	0.7	0.8	32.0	-10.7	0.7	0.7
TPU1	32.7	-12.1	0.3	0.3	33.5	-11.2	0.3	0.3	33.4	-11.3	0.3	0.3
MLA1	33.5	-10.5	0.7	0.7	33.5	-10.5	0.7	0.7	33.0	-10.7	0.7	0.7
DTB1	32.8	-9.6	0.6	0.5	32.8	-9.6	0.6	0.5	32.4	-9.7	0.6	0.5
LOT1	31.7	-11.2	0.4	0.4	32.8	-10.0	0.2	0.3	32.7	-10.0	0.2	0.3
NSA1	32.7	-9.5	0.6	0.5	32.7	-9.5	0.6	0.5	32.3	-9.6	0.5	0.4
TCO1	30.5	-11.1	0.4	0.4	31.6	-9.9	0.3	0.3	31.6	-9.9	0.3	0.3
NAH2	31.7	-10.3	0.4	0.5	31.7	-10.3	0.4	0.5	31.6	-10.3	0.4	0.4
MON1	32.1	-11.8	0.3	0.3	33.2	-10.6	0.2	0.3	33.1	-10.7	0.2	0.3
CHE1	34.1	-10.5	0.8	0.5	34.1	-10.5	0.8	0.5	33.7	-10.7	0.8	0.5
NOI1	31.8	-11.3	0.3	0.3	32.9	-10.2	0.2	0.3	32.9	-10.2	0.2	0.3
NAD1	31.7	-10.8	0.3	0.4	32.4	-9.9	0.3	0.3	32.2	-9.9	0.3	0.3
MHA1	33.7	-11.2	0.8	0.7	33.7	-11.2	0.8	0.7	33.7	-11.2	0.8	0.7
TSN1	33.4	-11.2	0.8	0.8	33.4	-11.2	0.8	0.8	33.4	-11.2	0.8	0.8

Chapter 6

CRUSTAL MOVEMENT OF NORTHWESTERN VIETNAM AND ITS RELATION TO TECTONIC BLOCKS

6.1 Introduction

In the theory of plate tectonics the lithosphere is divided into blocks termed plates. The boundaries between plates can take three forms (ocean ridges, trenches, and faults) and be determined by present-day tectonic activity (Isacks et al., 1968; Morgan, 1968). Within the basic theory of plate tectonics, plate is considered to be rigid (without internal deformation) and rotates with respect to other plates. The deformation only takes place at plate boundaries. So the present-day tectonic activity mostly takes place at the boundaries of plates. Location of earthquake epicenters can be used to define plate boundaries. Earthquakes mainly focus on the narrow plate boundaries of oceanic lithosphere. While intraplate boundaries are hard to be defined due to distributed earthquakes over wide areas (Jackson and McKenzie, 1988). Especially, it is limited to define the boundary in region where has a low seismic productivity such as NWV (Figure 1.2). Another independent approach comes from the techniques of space geodesy. The present day plate motions can be directly inferred from GPS measurements (e.g., Shen et al., 2005; Simons et al., 2007). The motion of a plate on the Earths surface can be described by an Euler pole, using of a theorem of Euler. The rotation rate can be described by a scalar value at the Euler pole or by an Euler vector from the center of the Earth toward the Euler pole. Its magnitude is usually measured in degrees per million

years. Various plate models have been proposed using methods of space geodesy that explain the motions of plates or regions by representation of rotation poles in various reference frames (e.g., Altamimi et al., 2002; Calais et al., 2003; Shen et al., 2005; Simons et al., 2007). Thus, in this study we apply the geodetic approach to study the crustal movement of NWV and its relation to the Eurasia plate (EU), Sundaland block (SU), South China block (SC), and Baoshan sub-block (BS). NWV was originally considered to be a part of the Eurasian plate (DeMets et al., 1994). With increasing number of precise geodetic observation, it turned out that the NWV forms a border between SC (Shen et al., 2005) and SU (Simons et al., 2007). The Red River Fault in NWV is regarded as the northeastern tectonic boundary between SC and SU accommodating right-lateral shear strain (Wilson et al., 1998; Michel et al., 2001; Kreemer et al., 2003; Simons et al., 2007). Meanwhile, Bird (2003) and McCaffrey (2009) suggested this boundary is located farther south. Because of the slow relative motion between the SU and SC blocks and the scarcity of precise space geodetic measurement in this area, the actual location of the tectonic boundary is still uncertain. Thus, by using the dense GPS observation network in NWV, the study provides the new insight into large-scale tectonics in Southeast Asia.

6.2 A local velocity from Euler pole and angular rate of a plate

The theory to compute a local velocity at a specified location on one plate with respect to another plate is described by Cox and Hart (1986). The information on the relative plate/block motion between a pair of plates in relative plate motion models is summarized in a finite rotation axis ($\overrightarrow{OE}$) (Figure 6.1) that intersects the Earths surface at point **E** called the Euler pole of rotation (for those two plates). Global relative plate motion models are derived using geological and geophysical data records, averaged over the past few million years, such as RM2 (Minster and Jordan, 1978), NUVEL-1A (DeMets et al., 1990, 1994), and the newest MORVEL (DeMets et al., 2010). The models divide the lithosphere into tectonic plates (about 10 large plates and some small ones). Each pair of plates has a distinct rotation axis. Finding the local velocity at **P** on plate B with respect to plate A, that is the motion along a small circle centered on the Euler pole **E** corresponding to an angular rate ${}_A\boldsymbol{\omega}_B$. We can calculate the local velocity using the cross product of the angular velocity vector and the position vector as follow

$$\mathbf{V} =_A \boldsymbol{\omega}_B \text{ x } (\mathbf{P}) \tag{6.1}$$

where ${}_A\boldsymbol{\omega}_B$ is the plate rotation rate vector, hereafter termed $\boldsymbol{\omega}$, $\mathbf{P}$ is the position vector of our considered point.

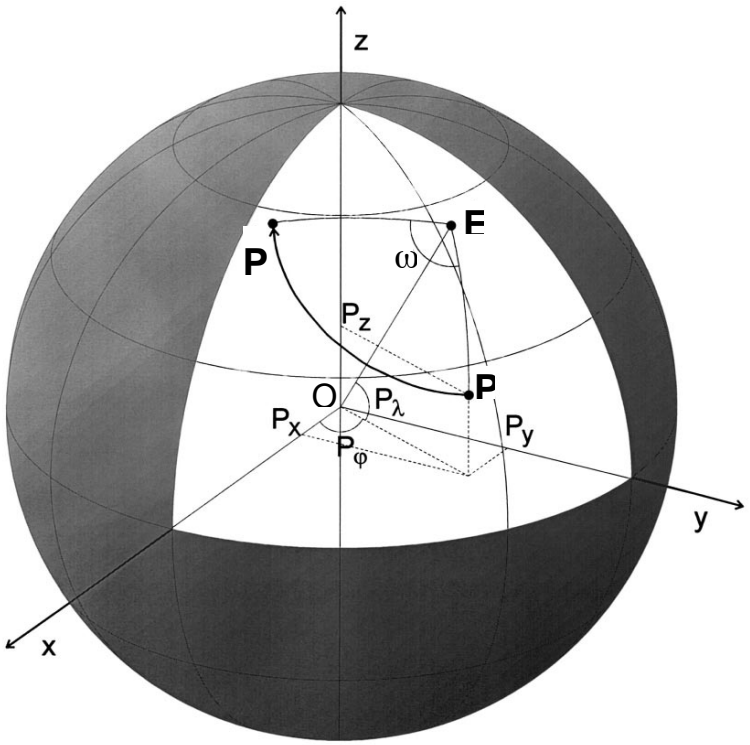

Figure 6.1: Definition of spherical geometry of a point $\mathbf{P}$ in the geographical (P_λ is the latitude, P_φ the longitude) and Cartesian (P_x, P_y, P_z) coordinate system and of the Euler pole $\mathbf{E}$ and its rotation angle ω. **P'** is a rotated point of $\mathbf{P}$.

The point $\mathbf{P}$ on the Earth's surface is defined by its geographical latitude P_λ and longitude P_φ or by its Cartesian coordinates P_x, P_y, P_z (Figure 6.1). Similarly, the Euler pole $\mathbf{E}$ is defined by (E_λ, E_φ) or (E_x, E_y, E_z). Then ω_x, ω_y, ω_z is the angular rotation vector components at the Euler pole in Cartesian reference frame. If we define ω is the scalar angular rotation rate, there is a relationship as follow:

$$\boldsymbol{\omega} = \omega\mathbf{E} \tag{6.2}$$

It is easy to convert the latitudes and longitudes to vectors into a Cartesian reference frame centered at Earth's center:

$$\begin{cases} P_x = \cos P_\lambda \cos P_\varphi \\ P_y = \cos P_\lambda \sin P_\varphi \\ P_z = \sin P_\lambda \end{cases} \tag{6.3}$$

$$\begin{cases} \omega_x = \omega \cos E_\lambda \cos E_\varphi \\ \omega_y = \omega \cos E_\lambda \sin E_\varphi \\ \omega_z = \omega \sin E_\lambda \end{cases} \tag{6.4}$$

In the Cartesian reference frame, the x-component lies in the plane of Earth's equator and points toward a longitude of 0°, the y-component is in the equatorial plane and points towards 90° East, and the z-component points towards the North Pole (Fig 6.1). We can compute the vector cross product in equation (6.1) to get the velocity values in the Cartesian reference frame

$$\mathbf{V} = \begin{pmatrix} V_x \\ V_y \\ V_z \end{pmatrix} = \omega R \begin{pmatrix} E_y P_z - P_y E_z \\ E_z P_x - P_z E_x \\ E_x P_y - P_x E_y \end{pmatrix} \tag{6.5}$$

In equation (6.5), we express the components in global Cartesian coordinate system, however we are usually interested in the local Cartesian components, northward (N), eastward (E), and upward (U) at point $\mathbf{P}$

$$\begin{pmatrix} V_N \\ V_E \\ V_U \end{pmatrix} = \mathbf{T} \begin{pmatrix} V_x \\ V_y \\ V_z \end{pmatrix} \tag{6.6}$$

where

$$\mathbf{T} = \begin{bmatrix} -\sin P_\lambda \cos P_\varphi & -\sin P_\lambda \sin P_\varphi & \cos P_\lambda \\ -\sin P_\varphi & \cos P_\varphi & 0 \\ -\cos P_\lambda \cos P_\varphi & -\cos P_\lambda \sin P_\varphi & -\sin P_\lambda \end{bmatrix} \tag{6.7}$$

The equation (6.6) becomes

$$\begin{cases} V_N = -\sin P_\lambda \cos P_\varphi V_x - \sin P_\lambda \sin P_\varphi V_y + \cos P_\lambda V_z \\ V_E = -\sin P_\varphi V_x + \cos P_\varphi V_y \\ V_U = -\cos P_\lambda \cos P_\varphi V_x - \cos P_\lambda \sin P_\varphi V_y - \sin P_\lambda V_z \end{cases} \tag{6.8}$$

To convert a vector expressed in local components (N, E, U) to one in global components (x, y, z), we simply use the inverse matrix $\mathbf{T}^{-1}$. Because the matrix $\mathbf{T}$ is a transformation of an orthonormal basis, $\mathbf{T}$ is an orthogonal matrix. Thus, the inverse $\mathbf{T}^{-1}$ is equal to the transposed matrix $\mathbf{T}^{-T}$ and can be derived by switching the rows and columns of $\mathbf{T}$. We have the converted case of equation (6.6)

$$\begin{pmatrix} V_x \\ V_y \\ V_z \end{pmatrix} = \mathbf{T}^{-1} \begin{pmatrix} V_N \\ V_E \\ V_U \end{pmatrix} \tag{6.9}$$

where

$$\mathbf{T}^{-1} = \begin{bmatrix} -\sin P_\lambda \cos P_\varphi & -\sin P_\varphi & -\cos P_\lambda \cos P_\varphi \\ -\sin P_\lambda \sin P_\varphi & \cos P_\varphi & -\cos P_\lambda \sin P_\varphi \\ \cos P_\lambda & 0 & -\sin P_\lambda \end{bmatrix} \tag{6.10}$$

The equation (6.9) becomes

$$\begin{cases} V_x = -\sin P_\lambda \cos P_\varphi V_N - \sin P_\varphi V_E - \cos P_\lambda \cos P_\varphi V_U \\ V_y = -\sin P_\lambda \sin P_\varphi V_N + \cos P_\varphi V_E - \cos P_\lambda \sin P_\varphi V_U \\ V_z = \cos P_\lambda V_N - \sin P_\lambda V_U \end{cases} \tag{6.11}$$

Combining the equations (6.5) and (6.8), we have the equation as follow

$$\begin{cases} V_N = \omega R[-\sin P_\lambda \cos P_\varphi (E_y P_z - P_y E_z) - \sin P_\lambda \sin P_\varphi (E_z P_x - P_z E_x) + \cos P_\lambda (E_x P_y - P_x E_y)] \\ V_E = \omega R[-\sin P_\varphi (E_y P_z - P_y E_z) + \cos P_\varphi (E_z P_x - P_z E_x)] \\ V_U = \omega R[-\cos P_\lambda \cos P_\varphi (E_y P_z - P_y E_z) - \cos P_\lambda \sin P_\varphi (E_z P_x - P_z E_x) - \sin P_\lambda (E_x P_y - P_x E_y)] \end{cases} \tag{6.12}$$

6.3 Classifying crustal movements in a region

We assume that we have horizontal crustal velocities at GPS sites in a region, which are inferred from GPS measurements in a reference frame. The Earths surface is covered by more than two plates, therefore there must be places where three plates come together, but none where four or more plates meet. The meeting sites of three plate boundaries are named "triple junctions". However, in this study, just simplify assuming that the region is surrounded by three plates (A, B, and C) that are represented by their Euler poles ($\mathbf{E}_\mathrm{A}$, $\mathbf{E}_\mathrm{B}$, $\mathbf{E}_\mathrm{C}$) and angular rates (ω_A, ω_B, and ω_C). In this case, the plate boundary zones between the plates are considered by taking into account the motions of the sites in that region as well as their relation to these plates. For example, site P is examined with its GPS-derived horizontal crustal velocities (VN_P, VE_P). The plate velocities in the same reference frame at site P are calculated for each plate A, B and C from equation (6.12), based on their angular velocity poles. (VN_PA, VE_PA), (VN_PB, VE_PB), and (VN_PC, VE_PC) represent the predicted plate motions at site P for A, B, and C plates, respectively. Figure 6.2-a shows plate geometry with uncertain boundary zones between the plates and location of site P. The GPS-derived and predicted plate velocities at site P can be represented by their coordinates in velocity diagram (Figure 6.2-b). Here, we consider the velocity of point P in the velocity diagram lain inside the velocity triangle ABC. In order to evaluate the locus of P with respect to the velocity triangle ABC in the

velocity diagram, this point satisfies the velocities on all three-cornered as the velocity relationships are proposed as follow

$$\begin{cases} VN_P = \alpha VN_{AP} + \beta VN_{BP} + \gamma VN_{CP} \\ VE_P = \alpha VE_{AP} + \beta VE_{BP} + \gamma VE_{CP} \\ \alpha + \beta + \gamma = 1 \end{cases} \tag{6.13}$$

where α, β, and γ are the contributed percentages of A, B, and C plate velocities, respectively. The largest percentage implies that the GPS-derived velocity at site P is the closest to that of the corresponding plate. It is one of information to study the plate boundary zone.

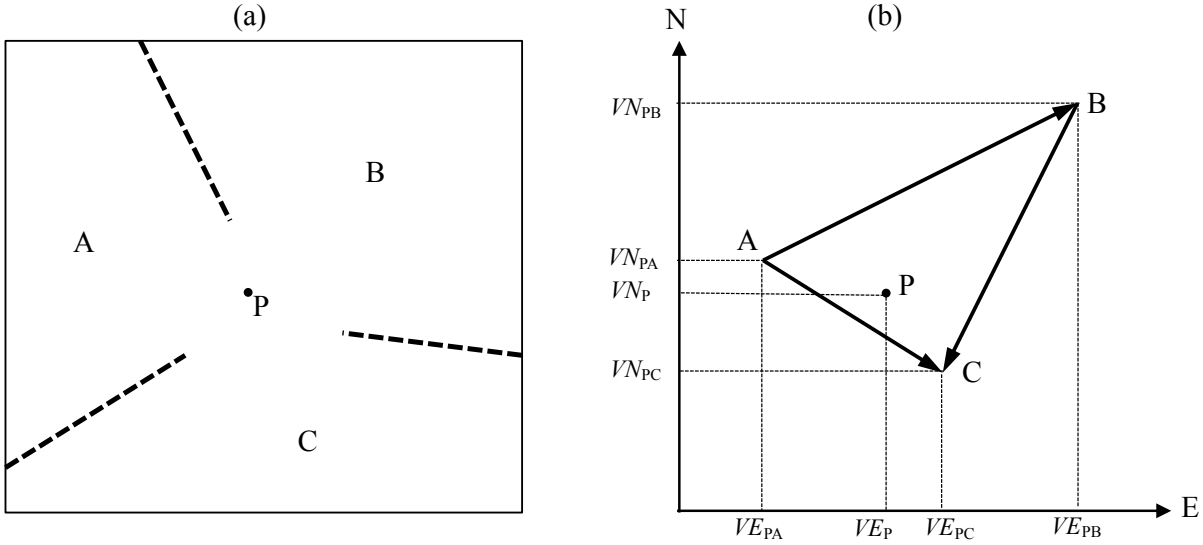

Figure 6.2: (a) Geometry diagram of plates and location of site P. (b) Velocity space representation of P.

6.4 Transforming the local velocity between ITRF2000 and ITRF2008

In this study, we use the Euler pole and angular velocity of plate/block that are reproduced in Table 6.1 to compute the plate velocities at GPS sites in NWV, utilizing the equation (6.12). The GPS-derived angular velocities in Table 6.1 are relative to ITRF2000 reference frame. Those plate velocities are in ITRF2000 reference frame, while the GPS velocities in this study are analyzed in ITRF2008. However, these two ITRF versions have a significant difference in their frame origin velocity, such that velocities in ITRF2008 will be different (in 3D) by close to 1.8 mm/yr from those in ITRF2000. The velocity difference should be mainly in the north-south and vertical

components. What this means is that it is not correct to use a plate motion estimate in ITRF2000 with velocities in ITRF2008 as the geocenter difference changes the plate angular velocities (plate angular velocity estimates are tied to the frame origin). There are no new estimates in ITRF2008 for SU, SC, EU, and Baoshan sub-block (BS). Thus we need to correct for the geocenter difference between the frames and then subtract the predicted plate motion. This may have a small effect, but this might change the tectonic interpretation at the complex plate boundary.

The standard model of transformation between two reference systems is a Euclidian similarity of fourteen parameters: three translations (T_{x}, T_{y}, T_{z}), one scale factor (D), and three rotations (R_{x}, R_{y}, R_{z}), and their rates: $\dot{T}_{\mathrm{x}}$, $\dot{T}_{\mathrm{y}}$, $\dot{T}_{\mathrm{z}}$, $\dot{D}$, $\dot{R}_{\mathrm{x}}$, $\dot{R}_{\mathrm{y}}$, $\dot{R}_{\mathrm{z}}$, designated respectively. The transformation parameters are produced by the International Terrestrial Reference Frame (website: http://itrf.ensg.ign.fr/ITRF_solutions/) and reproduced in Table 6.2 and 6.3. The transformation parameters presented in those tables are at difference epochs: 2000.0 and 2005.0. To convert a given transformation parameter P at an epoch $EPOCH$ to any epoch t, we obtain its value by using equation (6.14)

$$P_t = P_{EPOCH} + \dot{P}_{EPOCH} * (t - EPOCH) \tag{6.14}$$

Table 6.1: The absolute and relative rotation pole of plate/block.

Plate/Block	Reference Frame	Euler pole		Rotation rate ω(°/Myr)	Reference
		Lat. (°N)	Lon. (°E)		
Sundaland	ITRF2000	49.0 ± 1.9	-94.2 ± 0.3	0.336 ± 0.007	Simons et al. (2007)
South China	ITRF2000	61.2 ± 1.4	-115.6 ± 0.1	0.322 ± 0.002	Shen et al. (2005) Simons et al. (2007)
Eurasian	ITRF2000	52.3 ± 0.2	-107.0 ± 0.2	0.245 ± 0.005	Calais et al. (2003)
Baoshan/Eurasian	ITRF2000	21.7 ± 5.2	72.7 ± 20.9	-0.253 ± 0.092	Shen et al. (2005)

We convert the transformation parameters at epoch 2000.0 to epoch 2005.0 as below

$$P_{2005.0} = P_{2000.0} + 5.0 * \dot{P}_{2000.0} \tag{6.15}$$

Now we have the transformation parameters from ITRF2000 to ITRF2005 and form ITRF2005 to ITRF2008 at the same epoch 2005.0. So the transformation parameters from ITRF2000 to ITRF2008 at epoch 2005.0 can compute and symbolically expressed

as equation (6.16)

$$(ITRF2000 \rightarrow ITRF2008) = (ITRF2000 \rightarrow ITRF2005) + (ITRF2005 \rightarrow ITRF2008) \tag{6.16}$$

The parameters and their errors are presented in Table 6.4. The errors are calculated as quadratic mean or root mean square

$$\sigma_{ITRF2000 \rightarrow ITRF2008} = \sqrt{\frac{1}{2}(\sigma^2_{ITRF2000 \rightarrow ITRF2005} + \sigma^2_{ITRF2005 \rightarrow ITRF2008})} \tag{6.17}$$

Let $x(t)_{ITRF2000}$, $y(t)_{ITRF2000}$, $z(t)_{ITRF2000}$ denote the ITRF2000 coordinates for a point at time t in the Cartesian coordinate system. The transformation of the coordinates in ITRF2000 into $x(t)_{ITRF2008}$, $y(t)_{ITRF2008}$, $z(t)_{ITRF2008}$ coordinates in ITRF2008 is expressed by

$$\begin{pmatrix} x(t)_{ITRF2008} \\ y(t)_{ITRF2008} \\ z(t)_{ITRF2008} \end{pmatrix} = \begin{pmatrix} x(t)_{ITRF2000} \\ y(t)_{ITRF2000} \\ z(t)_{ITRF2000} \end{pmatrix} + \begin{pmatrix} T_x \\ T_y \\ T_z \end{pmatrix} + \begin{pmatrix} D & -R_z & R_y \\ R_z & D & -R_x \\ -R_y & R_x & D \end{pmatrix} \begin{pmatrix} x(t)_{ITRF2000} \\ y(t)_{ITRF2000} \\ z(t)_{ITRF2000} \end{pmatrix} \tag{6.18}$$

Generally, the coordinates (x, y, z) are functions of time to reflect the reality of the crustal motion associated with tectonic activities. T_{x}, T_{y}, T_{z}, D, R_{x}, R_{y}, R_{z} are also expressed as a function of time. The improvements in space-based geodetic techniques have enabled us to detect time-dependent variations of the seven parameters with some degree of accuracy. These time-related variations are assumed to be mostly linear.

Table 6.2: Transformation parameters at epoch 2000.0 and their first time derivatives from ITRF2000 to ITRF2005.

	T_x (mm)	T_y (mm)	T_z (mm)	D (ppb)	R_x (mas)	R_y (mas)	R_z (mas)
	-0.1	0.8	5.8	-0.40	-0.000	-0.000	-0.000
±	0.3	0.3	0.3	0.05	0.012	0.012	0.012

	$\dot{T}_x$ (mm/yr)	$\dot{T}_y$ (mm/yr)	$\dot{T}_z$ (mm/yr)	$\dot{D}$ (ppb/yr)	$\dot{R}_x$ (mas/yr)	$\dot{R}_y$ (mas/yr)	$\dot{R}_z$ (mas/yr)
	0.2	-0.1	1.8	-0.08	-0.000	-0.000	-0.000
±	0.3	0.3	0.3	0.05	0.012	0.012	0.012

Velocities referred to the ITRF2008 reference frame can be obtained from their corresponding ITRF2000 velocities by differentiating the equation (6.18) with respect

Table 6.3: Transformation parameters at epoch 2005.0 and their first time derivatives from ITRF2005 to ITRF2008.

	T_x (mm)	T_y (mm)	T_z (mm)	D (ppb)	R_x (mas)	R_y (mas)	R_z (mas)
	0.5	0.9	4.7	-0.94	-0.000	-0.000	-0.000
±	0.2	0.2	0.2	0.03	0.008	0.008	0.008

	$\dot{T}_x$ (mm/yr)	$\dot{T}_y$ (mm/yr)	$\dot{T}_z$ (mm/yr)	$\dot{D}$ (ppb/yr)	$\dot{R}_x$ (mas/yr)	$\dot{R}_y$ (mas/yr)	$\dot{R}_z$ (mas/yr)
	-0.3	-0.0	-0.0	-0.00	-0.000	-0.000	-0.000
±	0.2	0.2	0.2	0.03	0.008	0.008	0.008

to time. Since the derivative of coordinates (x, y, z) is about 100 mm/yr and the rotations (R_x, R_y, R_z) and scale factor D are of 10^{-6} level, the terms ($D\dot{x}$, $D\dot{y}$, $D\dot{z}$) and ($R_\mathrm{x}\dot{y}$, $R_\mathrm{x}\dot{z}$, $R_\mathrm{y}\dot{x}$, $R_\mathrm{y}\dot{z}$, $R_\mathrm{z}\dot{x}$, $R_\mathrm{z}\dot{y}$) are negligible, about 0.01 mm over 100 years. Thus the transformation equation of velocity between ITRF2000 and ITRF2008 reference frame is expressed

$$\begin{pmatrix} V_{x_{ITRF2008}} \\ V_{y_{ITRF2008}} \\ V_{z_{ITRF2008}} \end{pmatrix} = \begin{pmatrix} V_{x_{ITRF2000}} \\ V_{y_{ITRF2000}} \\ V_{z_{ITRF2000}} \end{pmatrix} + \begin{pmatrix} \dot{T}_x \\ \dot{T}_y \\ \dot{T}_z \end{pmatrix} + \begin{pmatrix} \dot{D} & -\dot{R}_z & \dot{R}_y \\ \dot{R}_z & \dot{D} & -\dot{R}_x \\ -\dot{R}_y & \dot{R}_x & \dot{D} \end{pmatrix} \begin{pmatrix} x(t)_{ITRF2000} \\ y(t)_{ITRF2000} \\ z(t)_{ITRF2000} \end{pmatrix} \quad (6.19)$$

where ($V_{\mathrm{xITRF2000}}$, $V_{\mathrm{yITRF2000}}$, $V_{\mathrm{zITRF2000}}$) and ($V_{\mathrm{xITRF2008}}$, $V_{\mathrm{yITRF2008}}$, $V_{\mathrm{zITRF2008}}$) are velocity components at the point (x, y, z) at time t (here is epoch 2005.0) in ITRF2000 and ITRF2008 reference frame, respectively. Those are velocity vectors expressed in the global Cartesian coordinate system. To convert to local coordinate system (N, E, U), we simply use the equations (6.6 and 6.7). We transform a local velocity vector in ITRF2000 to that in ITRF2008 at epoch 2005.0, using the transformation parameters in Table 6.4.

6.5 Results and discussion

6.5.1 Motion of NWV relative to tectonic blocks in ITRF2008

The plate velocities in ITRF2008 reference frame at GPS sites in NWV are calculated for EU, SU, SC and BS, based on the angular velocity poles reported by Calais et al.

Table 6.4: Transformation parameters at epoch 2005.0 and their first time derivatives from ITRF2000 to ITRF2008.

	T_x (mm)	T_y (mm)	T_z (mm)	D (ppb)	R_x (mas)	R_y (mas)	R_z (mas)
	1.4	1.2	19.5	-1.74	0.000	0.000	0.000
±	0.3	0.3	0.3	0.04	0.010	0.010	0.010
	$\dot{T}_x$ (mm/yr)	$\dot{T}_y$ (mm/yr)	$\dot{T}_z$ (mm/yr)	$\dot{D}$ (ppb/yr)	$\dot{R}_x$ (mas/yr)	$\dot{R}_y$ (mas/yr)	$\dot{R}_z$ (mas/yr)
	-0.1	-0.1	1.8	-0.08	0.000	0.000	0.000
±	0.3	0.3	0.3	0.04	0.010	0.010	0.010

(2003), Simons et al. (2007), and Shen et al. (2005) for the last two blocks, respectively. In order to verify the tectonic affiliation of the study area, we then subtract the predicted plate motions from the final GPS velocities analyzed in Chapter 5 to receive the motions with respect to each plate/block.

The final GPS velocity field (Figure 6.3) shows that NWV is moving in the east-southeastward direction with an average rate of 34.3 ± 0.7 mm/yr and azimuth of N108° ± 0.7°E in ITRF2008. This area has a significantly different motion from that of the Eurasia plate defined by Calais et al. (2003) ∼8 mm/yr in the N117°E direction (Table 6.5 and Figure 6.4). The NWV study area moves independently of the stable Eurasia plate, as do the SC (Wang et al., 2001; Shen et al., 2005) and SU blocks (Michel et al., 2001; Kreemer et al., 2003; Simons et al., 2007).

With respect to SU, our GPS sites coherently show south-southwestward movement at a rate of 4.4 to 6.3 mm/yr to the direction of N191° - 218°E (Table 6.5 and Figure 6.5). These agree with the estimates of Simons et al. (2007) on the relative motion between SC and SU in the study area. The estimated velocities decrease gradually to the east, consistent with the SC-SU rotation pole located to the east of Luzon (Simons et al., 2007). This result is consistent with left-lateral shear of north-northeast trending faults such as DBPF.

With respect to SC, our GPS sites are moving with a velocity of 1.4 to 2.8 mm/yr with an azimuth of N193° - 261°E (Table 6.5 and Figure 6.6). In the SC frame, 12 sites have velocities smaller than 2 mm/yr. However, the systematic southwestward motion in the northwestern part of the GPS network implies that the GPS network is located in a deformation zone at the periphery of SC.

Table 6.5: Velocity difference between the final GPS velocity and four block models (mm/yr).

GPS site	Eurasian plate		Sundaland block		South China block		Baoshan sub-block	
	V_E	V_N	V_E	V_N	V_E	V_N	V_E	V_N
DON1	7.1	-4.8	-2.4	-5.8	-1.60	-2.30	6.9	6.9
LEM1	7.2	-4.9	-2.3	-5.9	-1.60	-2.40	7.1	6.8
NGA1	7.1	-4.2	-2.4	-5.2	-1.60	-1.80	6.9	7.5
HAM1	7.4	-3.9	-2.1	-4.9	-1.40	-1.50	7.3	7.8
NAN1	6.9	-3.5	-2.6	-4.6	-1.90	-1.10	7.0	8.1
TGA1	6.8	-3.6	-2.7	-4.6	-2.00	-1.20	6.9	8.2
CUT1	7.4	-3.3	-2.1	-4.3	-1.40	-0.90	7.4	8.6
PLA1	6.9	-3.8	-2.5	-4.8	-1.90	-1.40	7.0	8.1
CMA1	6.6	-3.9	-2.8	-4.9	-2.20	-1.50	6.8	7.9
TPU1	8.0	-4.4	-1.4	-5.3	-0.70	-2.00	8.2	7.6
MLA1	7.6	-3.8	-1.8	-4.7	-1.10	-1.40	7.8	8.2
DTB1	7.0	-2.8	-2.4	-3.7	-1.70	-0.40	7.3	9.2
LOT1	7.4	-3.1	-2.1	-4.0	-1.40	-0.70	7.6	8.9
NSA1	7.0	-2.7	-2.5	-3.6	-1.80	-0.30	7.2	9.3
TCO1	6.3	-3.0	-3.1	-3.9	-2.50	-0.60	6.6	9.0
NAH2	6.3	-3.4	-3.1	-4.3	-2.50	-1.00	6.6	8.6
MON1	7.8	-3.8	-1.6	-4.6	-1.00	-1.40	8.1	8.4
CHE1	8.4	-3.8	-1.0	-4.6	-0.40	-1.40	8.7	8.4
NOI1	7.6	-3.3	-1.8	-4.2	-1.20	-0.90	7.9	8.8
NAD1	6.9	-3.0	-2.5	-3.9	-1.90	-0.60	7.3	9.1
MHA1	8.5	-4.1	-0.9	-4.8	-0.40	-1.70	9.1	8.4
TSN1	8.2	-4.0	-1.2	-4.7	-0.70	-1.60	8.7	8.5

Referring to the BS, NWV GPS sites is moving in the northeastward direction with a motion of 9.8 to 12.4 mm/yr with an azimuth of N38° - 47°E (Table 6.5 and Figure 6.7). The GPS velocities increase gradually toward the east, consistent with left-lateral strike slip motion along the DBPF system. This result is in agreement with both long-term and short-term left-lateral slip rates along the Xianshuihe - Xiaojiang fault (XXF) zone in south China (12 ± 4 mm/yr, King et al. (1997); ∼10 mm/yr, Chen et al. (2000); 16 mm/yr, Shen et al. (2003); and 7 mm/yr, Shen et al. (2005)).

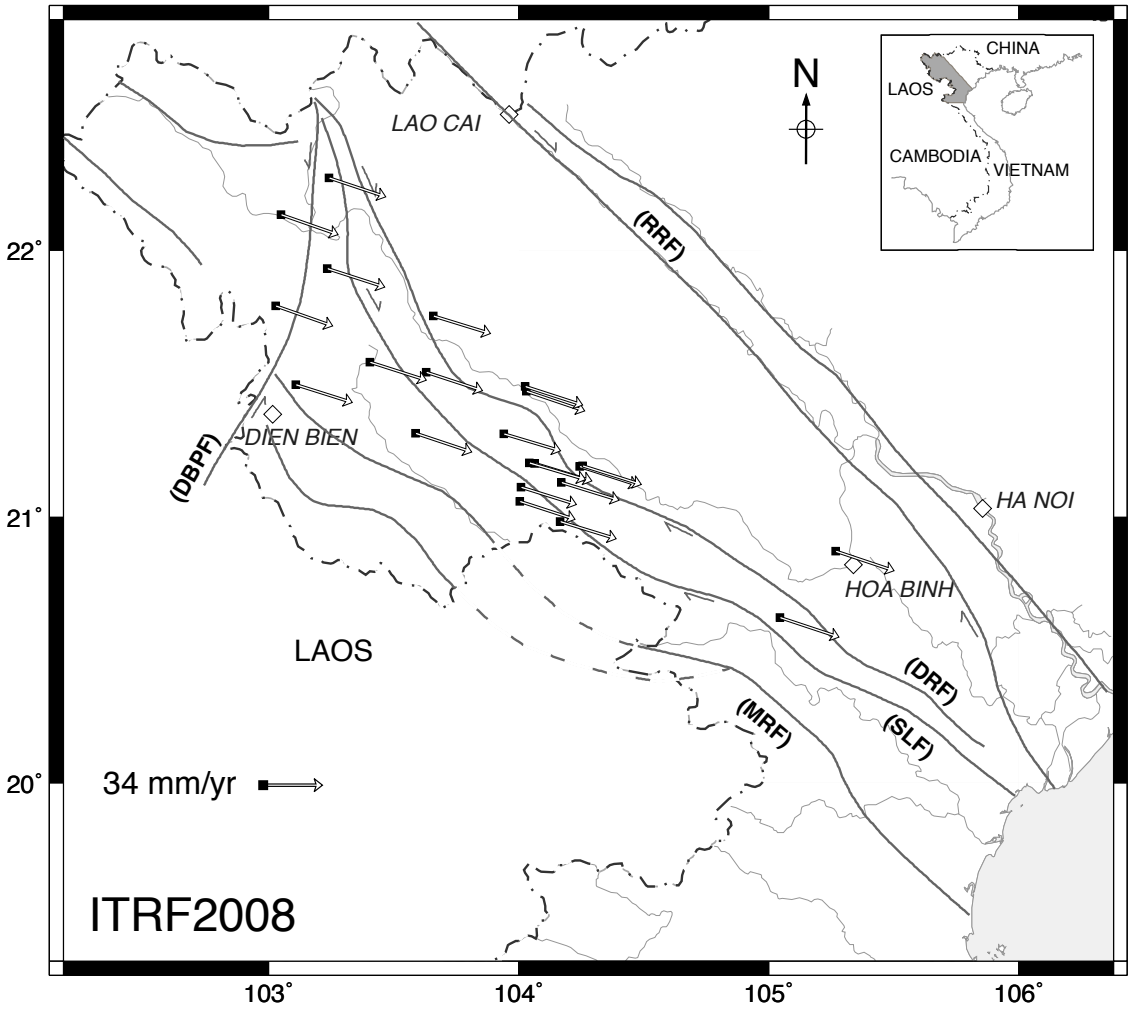

Figure 6.3: Velocities in NWV referred to ITRF2008. Thick solid and dashed lines depict the main fault systems. Thin lines indicate the permanent rivers and the coast of Vietnam. The small box denotes the location of the study area in Vietnam. Diamond symbols show cities.

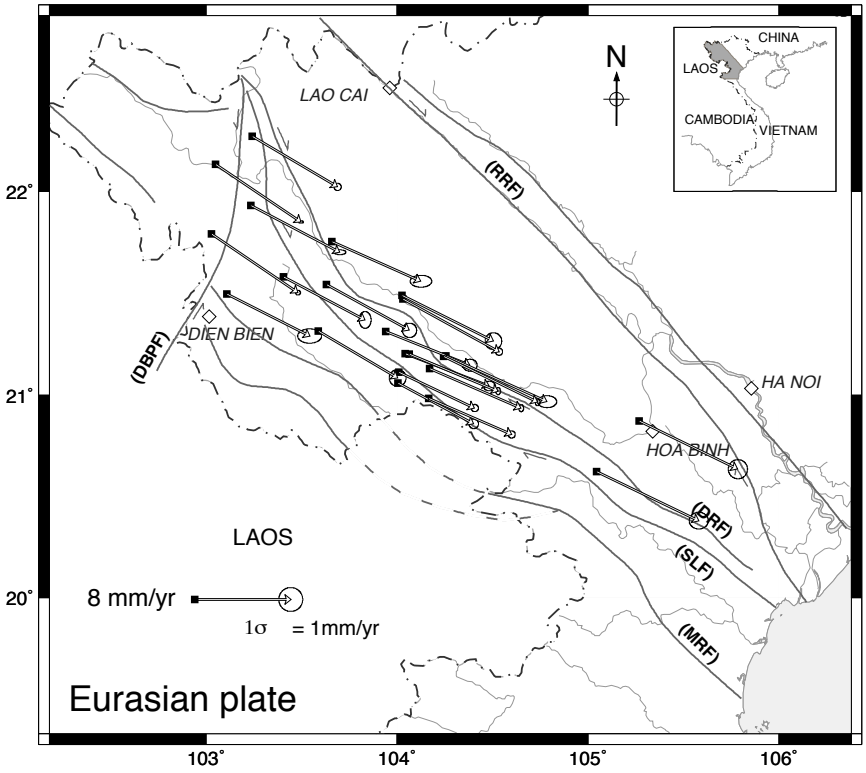

Figure 6.4: Velocities in NWV referred to the Eurasian plate (EU). Some descriptions are the same as Figure 6.3.

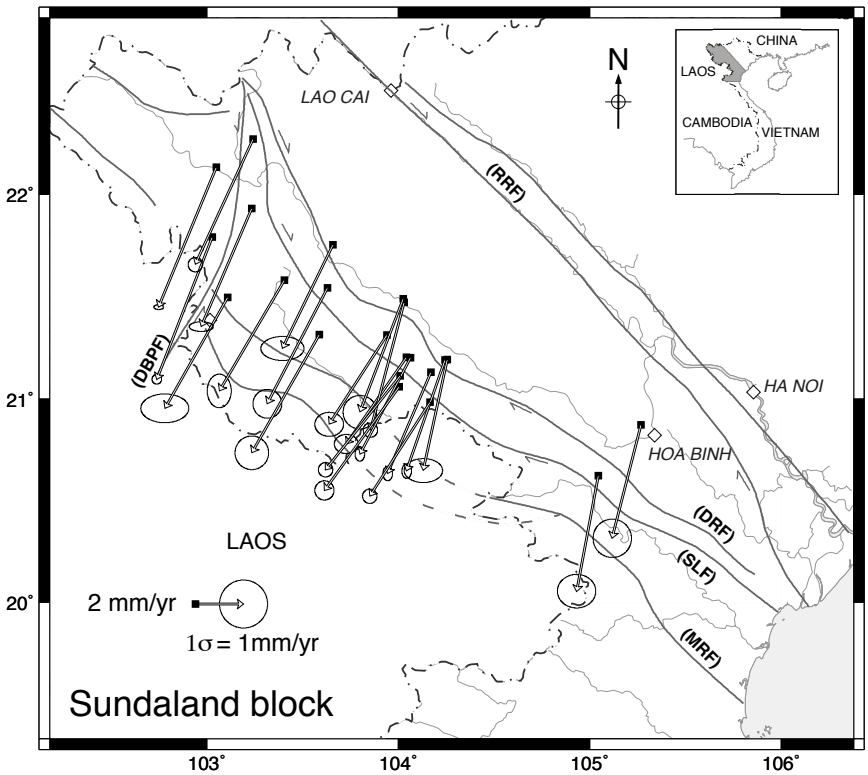

Figure 6.5: Velocities in NWV referred to the Sundaland block (SU). Some descriptions are the same as Figure 6.3.

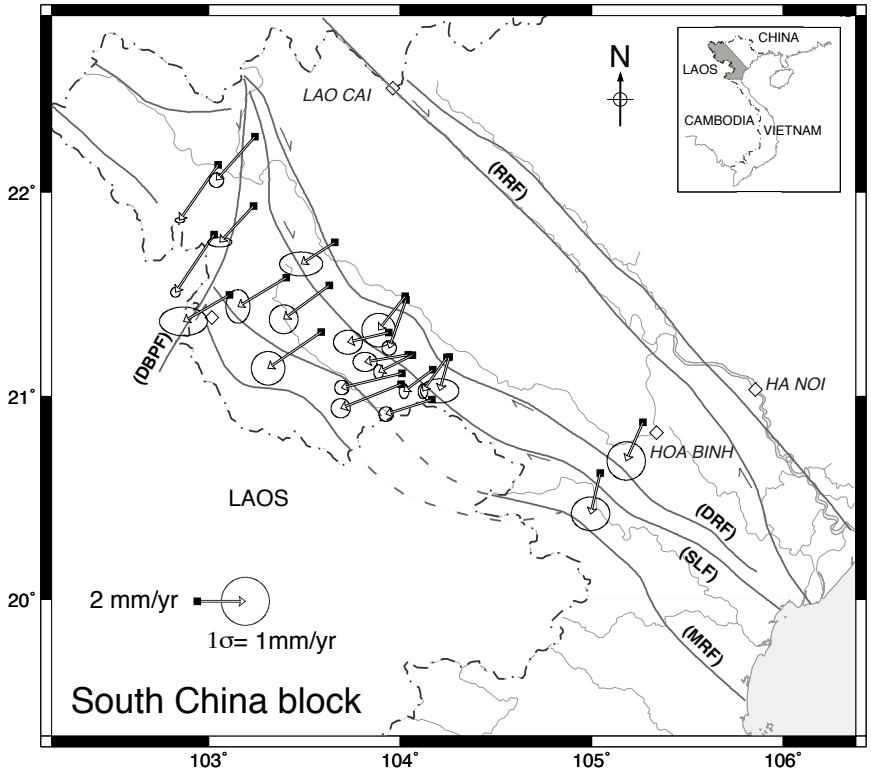

Figure 6.6: Velocities in NWV referred to the South China block (SC). Some descriptions are the same as Figure 6.3.

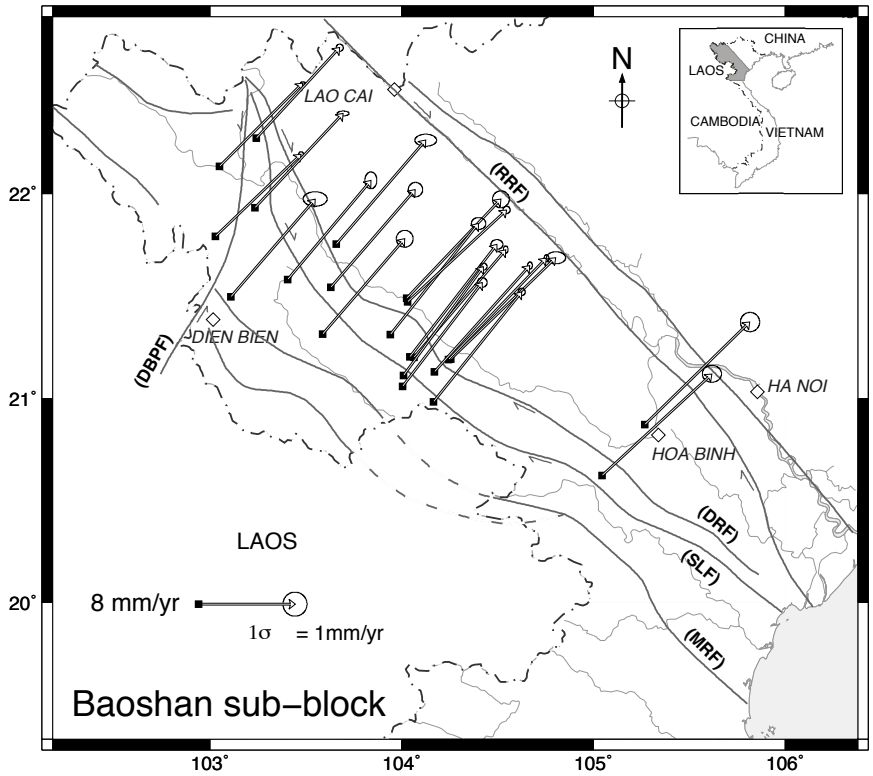

Figure 6.7: Velocities in NWV referred to the Baoshan sub-block (BS). Some descriptions are the same as Figure 6.3.

6.5.2 Classifying the crust movements in NWV according to geological structure and block motions

In order to discuss the tectonic affiliation of NWV in a larger framework, we create a vector diagram describing relative motions between GPS sites in NWV and SC, SU, EU, and the Baoshan sub-block (Shen et al., 2005), as shown in Figure 6.8. The dashed line circle with 2 mm/yr radius plotted in this figure represents the criterion for sites located on the stable SC block. This criterion is proposed by Shen et al. (2005) and Simons et al. (2007) to define a rigid block. The result implies that NWV motion is close to that of SC. This study area is in a deformation zone at the periphery of this block.

As discussed in session (6.3), we take into account three blocks SU, SC, and BS that come together and surround the NWV region. The contributed percentages of plate velocity at the GPS sites in each plate velocity triangle are evaluated and presented in Table 6.6. Only sites lie inside the plate velocity triangles in the velocity diagram (Figure 6.8) are considered. Because one of the contributed percentages of plate velocity at the sites becomes negative when these sites are outside of the plate velocity triangles such as DON1, LEM1, NGA1, TPU1, MLA1, TCO1, MON1, CHE1, MHA1, and TSN1 (Table 6.6). As the result, the contributed percentages of plate velocity at two long observation interval sites (NAH2 and NAD1) are the largest for the SU (61% and 53%, respectively). While, the contributions of BS (32% and 24%) at these sites are larger than the SC (7% and 23%, respectively). Moreover, these sites are south of the SLF and are near the stable SU block, located further south of the GPS network, than others (Figure 3.1). Thus, we can infer that the motions of the sites that located further south of the GPS network are closer to those of the SU (Table 6.6), although, the sites are in a deformation zone between SC, SU, and BS (Figure 6.8). The motions of two short observation interval sites (DTB1 and NSA1) are estimated to be close to those of the SU, however, their velocity uncertainties are large. In the map view Figure 3.1, DTB1, NSA1, LOT1, and NOI1 are located close each other between the SLF and DRF zones. Thus the motions of DTB1 and NSA1 are expected to be close to those of the long observation interval sites (LOT1 and NOI1), while the motions of two latters are close to those of SC (Table 6.6). Moreover, these four sites are inside the circle with 2 mm/yr radius (Figure 6.8). So, we can infer that the sites are probably in a deformation zone at the periphery of the SC. The sites (NAN1, TGA1, CUT1, PLA1, and CMA1) have the similar contributed percentages, but slightly larger for the SC, indicating that these sites are in a deformation zone between the three blocks. The HAM1 site is located west of the network, further north of the SU, but closer east of the BS (Figure 1.1 and 3.1). Our result supports that the contributed percentage of the BS (16%) is larger than that

of the SU (∼0%). That tendency is similar to DON1, LEM1, and NGA1 if in spite of the negative percentage values of the SU.

Table 6.6: Contributed percentages of plate velocity at GPS site in each plate velocity triangle.

GPS site	Contributed percentages (%)			Closest motion to block
	SC	SU	BS	
DON1	105	-22	17	-
LEM1	109	-26	16	-
NGA1	83	-2	19	-
HAM1	84	0	16	SC
NAN1	45	31	24	SC
TGA1	41	34	25	SC
CUT1	59	23	18	SC
PLA1	54	23	23	SC
CMA1	45	29	26	SC
TPU1	145	-49	4	-
MLA1	97	-8	12	-
DTB1	21	55	23	SU
LOT1	51	31	18	SC
NSA1	12	63	25	SU
TCO1	-9	76	33	-
NAH2	7	61	32	SU
MON1	102	-13	10	-
CHE1	136	-38	2	-
NOI1	72	14	14	SC
NAD1	23	53	24	SU
MHA1	148	-50	2	-
TSN1	127	-33	6	-

We also consider velocity values with respect to SC as well as geological structure such as active fault traces. The GPS sites can be classified into four groups, as shown with different symbols in Figure 6.8 (right). We use the same symbols (squares, triangles, inverted triangles, and stars) to pair with the geographic map in Figure 3.1. The inverted triangles (TPU1, MON1, MLA1, CHE1, CUT1, TSN1) and square groups (NOI1, LOT1, PLA1, NSA1, DTB1, MHA1) representing the sites located east of the DRF and between the SLF and DRF, respectively, do not significantly deviate from SC and most of the sites of the groups are inside the circle with 2 mm/yr radius. So the groups can be considered as a part of the SC. The groups are not clearly separated, probably due to the

locked nature of the SLF-DRF fault system. The triangle group (NGA1, HAM1, NAN1, TCO1, NAH2, NAD1, TGA1, CMA1) corresponds to the sites between the DBPF, SLF, and MRF. This group is separated from the former ones. It can be attributed to the distance of each group with respect to the stable SC block. It means that the sites of this group are located further south of the stable SC block compared with those of other groups (see the map views Fig 1.1 and 3.1). Their velocities with respect to the SC are consequently larger than 2 mm/yr (Figure 6.8). Only PLA1 is an outlier with a large velocity uncertainty. Its motion is similar to that of the triangle group, outside of the circle as unexpected. Another explanation is probably because the site is located close to the locked zone in northern portion of SLF where the largest 1983 Tuan Giao earthquake (Mw6.2) occurred (Figure 3.1). So, its motion is close to that of the triangle group, reflecting the locked nature of the SLF in this earthquake zone. The star group (LEM1, DON1), being west of DBPF, is independent from the other groups, possibly represents another region such as southwestern China or Myanmar that is described as the Baoshan sub-block (BS). It is in agreement with a suggestion of Lai et al. (2012) that DBPF represents eastern boundary of northern Indochina. Indochina is a peninsula of Southeast Asia comprising Vietnam, Laos, Cambodia, Thailand, Myanmar (Burma), and the mainland territory of Malaysia. The northern Indochina includes Vietnam, Laos, and Myanmar.

From the study in this chapter, we conclude that the changing trend of velocity in NWV does not follow the SC-SU combination, implying that this area does not represent the transition between only these two blocks. Rather, it is a transition zone among three blocks, SC, SU, and BS. However, the deformation zone mainly represents the SC motion, compared to the other two blocks (Figure 6.8-left). The transition zone between SC and SU should be spread out toward the south of the study area to reach site NONN (Figure 1.1 and 6.8) in central Vietnam, which represents SU motion (e.g., Bird, 2003; Simons et al., 2007). The NW-SE trending fault zones DRF and SLF appear to be accommodating part of relative motion ($<$ 4 mm/yr shown in Figure 6.8- left) between SC and SU. The RRF located further to the northeast, and multiple NW-SE trending faults possibly existing (Cao et al., 2003) to the south of the current study area down to NONN may also be accommodating some of the motion.

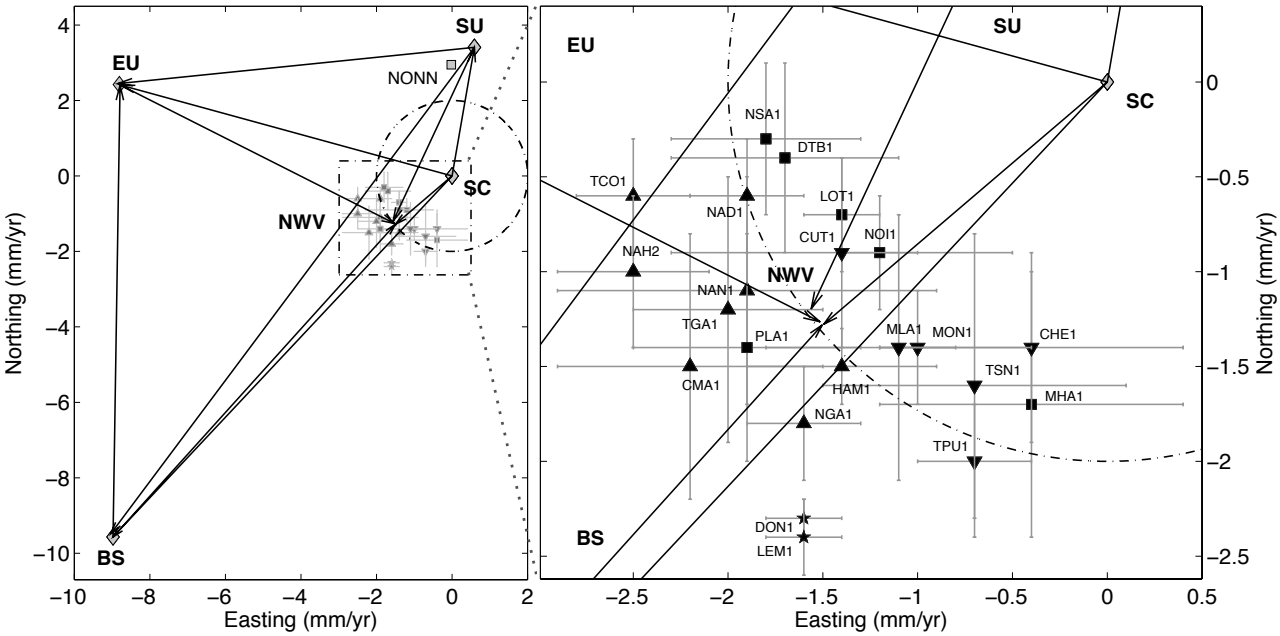

Figure 6.8: (left) Relative motion vectors between each pair among NWV, SC, SU, EU and BS. Velocities at the GPS sites in NWV with respect to SC are denoted by the solid circles with 1σ error bars. The solid square is NONN site (Figure 1.1). The rectangle with dot-dashed line is shown in detail in the right figure. (right) The GPS sites in NWV are classified into 4 groups geographically, as shown with different symbols. The star, inverted triangle, triangle, and square symbols correspond to the sites of west DBPF, of east DRF, between DBPF, SLF and MRF, and between SLF and DRF, respectively. The dot-dashed line circle with 2 mm/yr radius represents the criterion for sites located on the stable SC block.

Chapter 7

CRUSTAL DEFORMATION AND ITS IMPLICATION FOR EARTHQUAKE ACTIVITY IN NORTHWESTERN VIETNAM

7.1 Introduction

The continental deformed zone is usually wider than that in oceanic lithosphere where the deformation is restricted to narrow plate boundaries (Molnar and Tapponnier, 1975). Therefore, a framework is required to study the continental deformation which is different to that used to analyze deformation in oceanic lithosphere. Deformation within large continental tectonic regions such as mountain belts, intracontinental rifts, plateaus, basins, and continental transforms may be described by a discontinuous velocity field rather than by the relative motion of rigid blocks showed a uniform velocity field (England and Jackson, 1989). The velocity field of deformation regions is inferred either directly from GPS measurements (Clarke et al., 1998; McClusky et al., 2000; Sagiya, 2004; Simons et al., 2007), from spatial variations of strain rates estimated form seismicity (Holt et al., 1991; Jackson et al., 1992; Holt and Haines, 1993), or from long-term fault slip rates (England and Molnar, 1997). After obtaining the velocity field, an important problem is then to understand whether the motion is accommodated by the movement of discrete deformation zones or by a spatially continuous process. To understand the degree to which deformation is continuous or discontinuous across a region, some methods are usually used such as geologic, geodetic, and seismologic data analysis (Thatcher, 2003; McCaffrey, 2005). By applying those methods, some areas have

proven as large aseismic regions such as central Turkey, central Iran, the Tarim basin, and the Great Valley and Sierra Nevada in the southwestern United States, where their velocity fields present continuous patterns (McKenzie and Jackson, 1983; Avouac and Tapponnier, 1993; McClusky et al., 2000; McCaffrey, 2005). Meanwhile, in other areas such as the Walker Lane and Eastern California Shear Zone, their active deformations show diffuse distribution that their velocity fields cannot be considered as the relative motions of rigid blocks (Kreemer et al., 2009, 2010).

In this chapter, the velocity field inferred from GPS observations is analyzed to understand the crustal deformation and to evaluate seismic hazard in NWV. Strain rate field, an essential part of seismic hazard analysis, is calculated from the velocity field to locate the concentrated deformation zones. Geodetic measurements have been widely used to estimate surface strain and fault slip rates in active fault regions (e.g., Savage and Burford, 1973; Schmalzle et al., 2006). Thus, the results of GPS measurements are discussed in the context of deformation of the DBPF, SLF, and DRF zones in NWV, where strain may be accommodated along and adjacent to the fault system. GPS-derived locking depths of the faults are estimated and compared with the effective thickness of the locked zones (seismogenic thickness) derived from the seismicity to quantitatively measure the similarities and differences in the two approaches along the faults in NWV. The seismic moment accumulation rates along the faults are then examined based on the seismogenic thicknesses as suggested by seismicity and space geodesy.

7.2 Methodology

7.2.1 Dislocation model of strike-slip fault

Crustal deformation depends on the fault parameters (Cohen, 1999). In the simplest models, the Earth is taken to be homogeneous, linear elastic half-space, and deformation is driven by only the motion of the tectonic plates. Geodetic surface deformation measurements, combined with a mathematical model, can be used to estimate the effective thickness, referred to as the fault locking depth, of the zone that accumulates the interseismic strain. In this section, we will examine a simple two-dimensional elastic dislocation model, described by Savage and Burford (1973), with a vertical strike-slip fault embedded in an elastic half-space (Figure 7.1). The fault is locked at depth extending from the surface to the depth D, but slip at a constant rate below that depth. At great distances from the fault considered as the far-field, the left side of fault moves into the page at a constant relative velocity, $V/2$, while the right side of fault moves out of the page with a constant relative velocity, $-V/2$. The expression for the surface

displacement, $\nu(x)$, in the y direction, varying with distance from the fault, x, is as follow

$$\nu(x) = \frac{V}{\pi}\tan^{-1}\frac{x}{D} \tag{7.1}$$

Because of steady slip on the fault, the strain will be concentrated near the fault. Differentiating equation (7.1) with respect to the spatial coordinate perpendicular to the fault produces the shear strain rate at the free surface:

$$\varepsilon_{xy} = \frac{1}{2}\frac{\partial\nu}{\partial x} = \frac{V}{2\pi D}\frac{1}{1+\left(\frac{x}{D}\right)^2} \tag{7.2}$$

The shear strain rate is everywhere positive, thus shear strain accumulates on the fault between earthquakes. The equation (7.2) that is the interseismic strain is equal in magnitude and opposite in sign to the coseismic strain if the cumulative deep slip integrated over the time between earthquakes is equal to the coseismic slip. It means that the interseismic displacement plus coseismic displacement equals the long-term fault motion. For the peak strain rate occurring directly above the fault, its amplitude is given by

$$\varepsilon_{peak} = \frac{V}{2\pi D} \tag{7.3}$$

Strain rate decrease to half of its peak value at $x = D$. Similarly, coseismic displacement drops to half of its peak value at $x = D$.

Another related parameter that is the seismic moment accumulation rate M per unit length of fault L is given by the well-known formula

$$\frac{M}{L} = \mu V D \tag{7.4}$$

where is μ the crustal shear modulus, approximately 3×10^{10} N/m^2.

7.2.2 Strain rate distribution

Surface strain can provide important information on fundamental geodynamic processes. Strain rates can be estimated from the horizontal crustal motion velocity field measurements at GPS sites. Thus, continuous distribution of crustal deformation has essential importance.

In general, strain rate tensor is independent of the reference frame, and suitable for the discussion of deformation (Sagiya et al., 2000). We examine two-dimensional

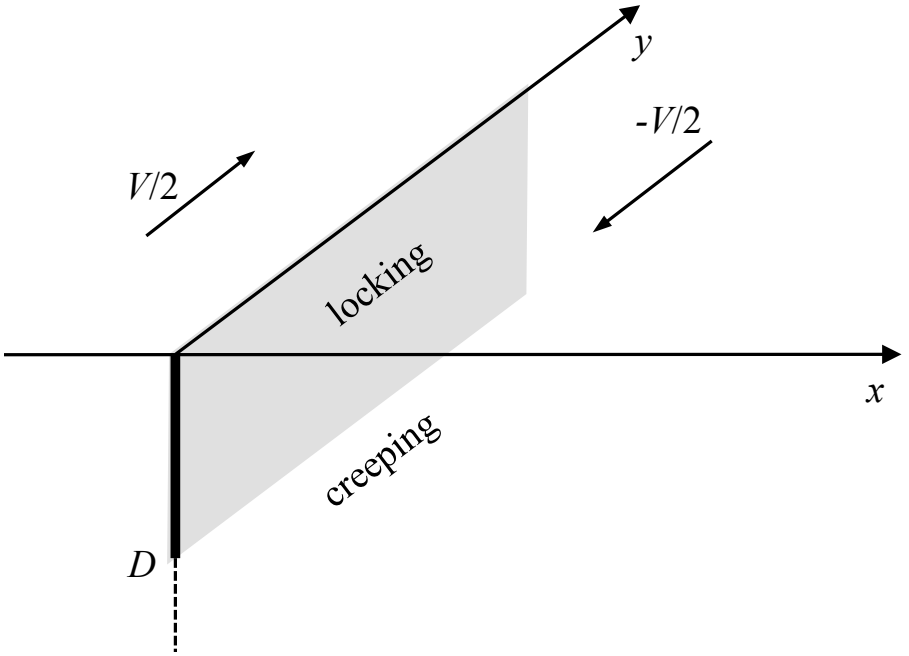

Figure 7.1: Simple model for strike-slip fault in the elastic half-space. The fault is locked from the earth's surface to depth D, but slips freely below that depth. The far-field slip rate of fault is V.

strain rate tensor (surface strain rate). In the strain rate modeling method, the two-dimensional strain rate tensor is defined as

$$u_i = t_i + \frac{\partial u_i}{\partial x_j} x_j = t_i + \dot{e}_{ij} x_j \tag{7.5}$$

where u_i is the GPS measured velocity of the GPS site, t_i is a constant of integration that represents the translation of a point at the origin of the coordinate system, x_j is the position of the GPS site, and $\dot{e}_{ij}$ is the strain rate tensor. To solve this system of linear equations using weighted least squares method, we rewrite the equations into matrices as Shen et al. (1996) and Sagiya et al. (2000). The horizontal displacement rate components (u, v), strain rate components ($\dot{e}_{xx}$, $\dot{e}_{xy}$, $\dot{e}_{yy}$) and a rotation rate ω at a particular point $\boldsymbol{x}_i = (x_i, y_i)$ are related with an observed displacement rate (U, V) at an observation point $\boldsymbol{X} = (X, Y)$ as follows:

$$\begin{pmatrix} U \\ V \end{pmatrix} = \begin{pmatrix} 1 & 0 & \Delta x_i & \Delta y_i & 0 & \Delta y_i \\ 0 & 1 & 0 & \Delta x_i & \Delta y_i & -\Delta x_i \end{pmatrix} \begin{bmatrix} u \\ v \\ \dot{e}_{xx} \\ \dot{e}_{xy} \\ \dot{e}_{yy} \\ \omega \end{bmatrix} + \begin{pmatrix} \varepsilon_x^i \\ \varepsilon_y^i \end{pmatrix} \tag{7.6}$$

where $\Delta x_i = X - x_i$ and $\Delta y_i = Y - y_i$. As known from classical mechanics, under the hypothesis of homogeneous and elastic strain field, the strain tensor can be expressed as

$$e_{ij} = \begin{pmatrix} \dfrac{\partial u}{\partial x} & \dfrac{1}{2}\left(\dfrac{\partial u}{\partial y} + \dfrac{\partial v}{\partial x}\right) \\ \dfrac{1}{2}\left(\dfrac{\partial u}{\partial x} + \dfrac{\partial v}{\partial y}\right) & \dfrac{\partial v}{\partial y} \end{pmatrix} \equiv \begin{pmatrix} \dot{\varepsilon}_{xx} & \dot{\varepsilon}_{xy} \\ \dot{\varepsilon}_{xy} & \dot{\varepsilon}_{yy} \end{pmatrix} \tag{7.7}$$

ε_x^i, ε_y^i are the observational errors and they are weighted depending on the distance between the observation point $\boldsymbol{X}$ and the calculation point $\boldsymbol{x}_i$ in the following formula

$$\varepsilon_{x,y}^i = \sigma_{x,y}^i e^{\left(\dfrac{-\Delta R_i^2}{2D^2}\right)} \tag{7.8}$$

where $\sigma_{x,y}^i$ is an original observational error of x (or y) component of the displacement rate, $\Delta R_i = |\boldsymbol{X} - \boldsymbol{x}_i|$ is the distance between the observation point $\boldsymbol{X}$ and the calculation point $\boldsymbol{x}_i$, and D is a specifying constant which specifies how the effect of observation points decay with distance from a calculation point and is called the Distance Decaying Constant (DDC). Observation points within one D distance contribute more than 67% to the least squares solution whereas those at a distance greater than 3D contribute less than 1% (Shen et al., 1996).

7.3 Result and discussion

7.3.1 Slip rates on the DBPF, SLF, and DRF zones

We evaluate relative motions across the fault zones around DPBF, DRF, and SLF in NWV. For this purpose, the velocity plot in Figure 7.2 (LEM1 fixed) is useful since the rigid-block translation common to the whole network has been mostly removed.

Near DBPF, most sites on the east side of DBPF with respect to LEM1 show significant motion at the 95% confidence level and their velocity vectors point parallel to the fault, roughly in the northward direction, implying left-lateral strike-slip across the fault zone. This result is in good agreement with the results of geomorphic and regional structural studies (Hung and Vinh, 2001; Hung, 2002; Zuchiewicz et al., 2004; Thuy, 2005; Tung and Thang, 2006, 2008). The left-lateral strike-slip faulting of DBPF zone can also be clearly seen in the fault-parallel (North) direction profile across the

fault (Figure 7.3). However, there is no significant displacement in the fault-normal (East) direction. Our GPS relative velocity across DPBF is 0.6 - 1.9 mm/yr in the north direction, consistent with the Holocene slip rate of 0.6 - 2 mm/yr (Zuchiewicz et al., 2004), and the Quaternary slip rate of 1.1 - 3.0 mm/yr (Tung and Thang, 2006, 2008). Lai et al. (2012) pointed out the present-day kinematics of the DBPF is likely to be the same as in the early Pliocene, and the current study supports their conclusion. In addition, velocities at three sites located along the DBPF (NGA1, HAM1, and NAN1) gradually increase (from 0.6 to 1.3 mm/yr) southward, which agrees with the increasing trend in the Quaternary fault slip rate from the north (1 - 1.25 mm/yr, Tung and Thang, 2006) to the south (2.5 - 3.0 mm/yr, Tung and Thang, 2008) though there is a systematic difference in the slip rate by a factor of 2 between the geodetic and geologic results. However, this geodetic result is good agreement with the geologic work of Tung (2011) from north to south of DBPF: (0.55 - 0.66 mm/yr), (0.66 - 1.11 mm/yr), and (1.38 - 1.66 mm/yr) along Ma Lu Thang - Chan Nua, Chan Nua - Huoi Leng, Huoi Leng - Thin Toc segments, respectively (Figure 2.1). The agreement between the geodetic and geologic results about the spatial distribution of the fault slip-rate along DBPF is a new finding.

In the velocity plot in Figure 7.2, velocities at MHA1 and TSN1 referred to LEM1 are not significant at the 95% confidence level. However, these vectors are directed toward the east or northeast, implying extension along the DRF-SLF to the west of these two sites. More observation and densification of the GPS network are needed to clarify this issue.

Figure 7.4 shows GPS velocity profiles across the SLF and DRF within the rectangular zone depicted by a dashed rectangle in Figure 3.1, referring to TPU1 as a fixed site. This zone is located far enough from the DBPF that the regional deformation pattern associated with the parallel SLF and DRF fault systems should appear along the profiles. There is no significant displacement in the fault-normal (N40°E) direction. On the other hand, the fault-parallel component (N50°W) clearly shows right-lateral displacement of 1 - 2 mm/yr across the DRF. Relative motion across the SLF does not seem to be significant. This result is also consistent with the long-term slip rates for SLF (<1.6 mm/yr for Pleistocene) and DRF (1.1 - 2.5 mm/yr for Quaternary) estimated by Hung (2002).

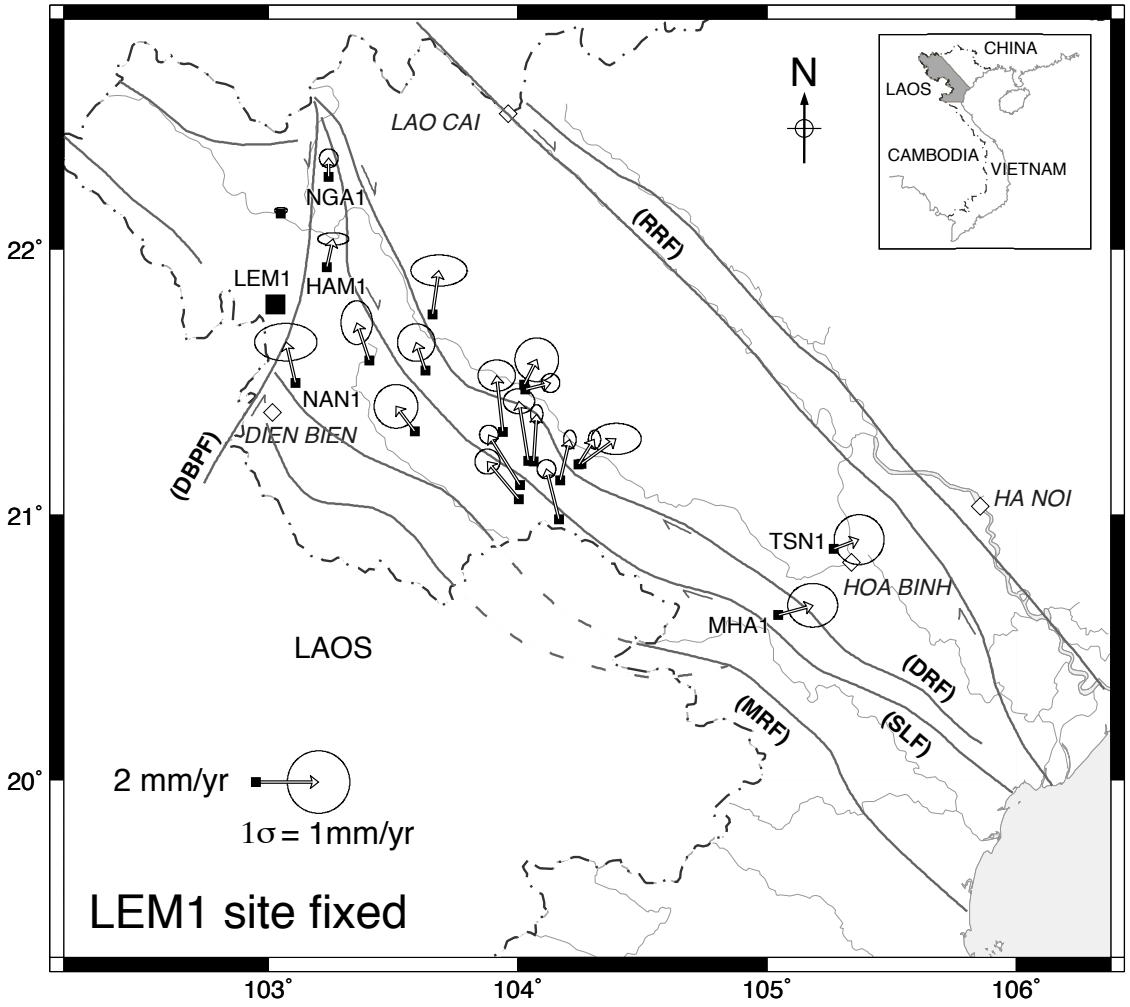

Figure 7.2: Velocities in NWV referred to LEM1 site. Thick solid and dashed lines depict the main fault systems. Thin lines indicate the permanent rivers and the coast of Vietnam. The small box denotes the location of the study area in Vietnam. Diamond symbols show cities.

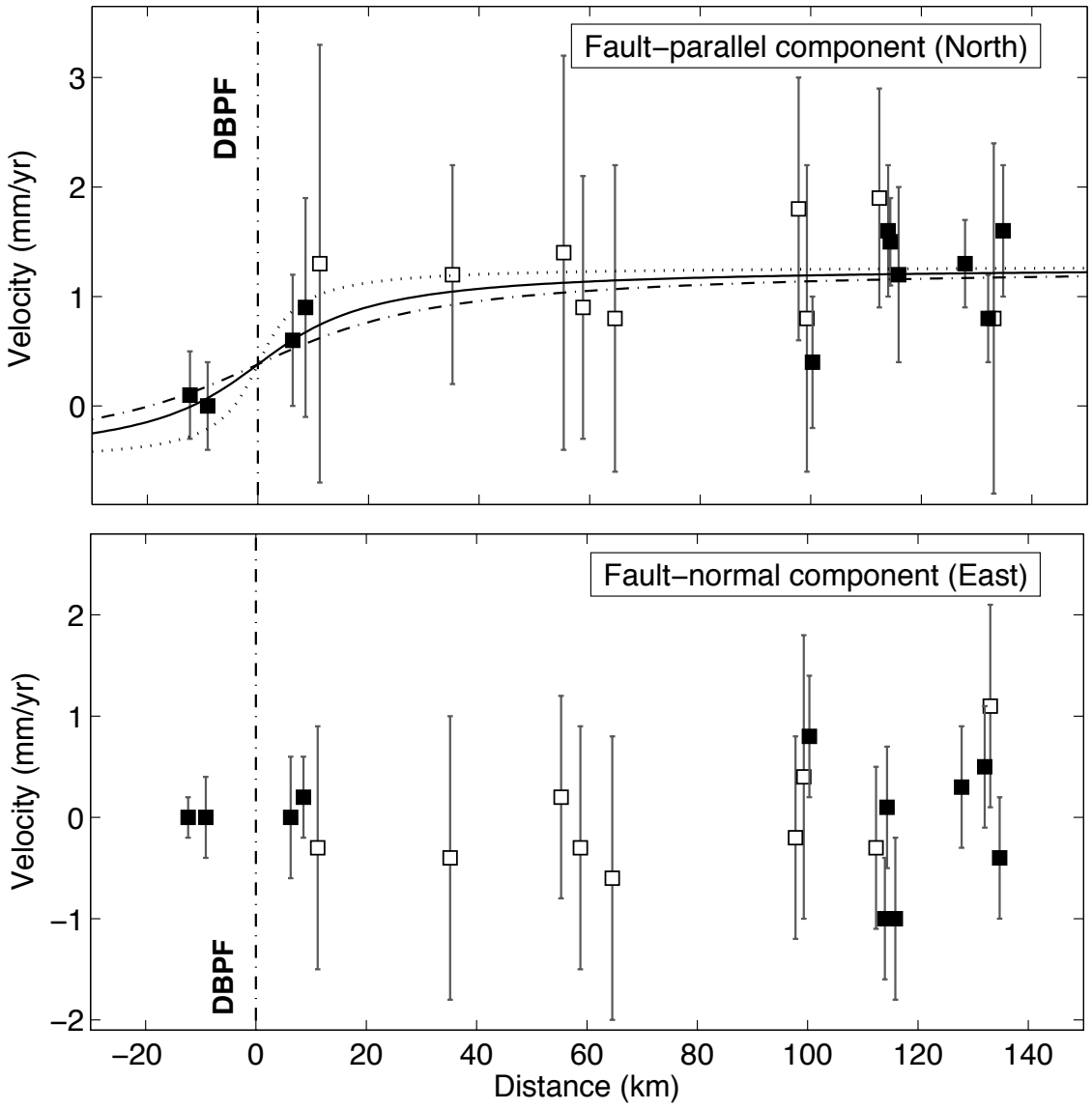

Figure 7.3: GPS velocity profiles across the DBPF. (top) Velocity component in the north direction plotted along the same direction, which is considered as the fault-parallel component. The black dotted, solid and dot-dashed lines represent the locking depths of 5.5, 15.3, 25.1 km (the best estimate and $\pm 1\sigma$ deviations), respectively. The slip rate of locking models is 1.8 mm/yr across DBPF. The estimated model parameters for DBPF are presented in Table 7.1. (bottom) The velocity component in the east direction. It is the fault-normal component with extension positive. Black and white squares indicate sites with long and short observation intervals, respectively (Table 3.1). Error bars are for the 95% confidence level. The vertical dot-dashed lines delineate the location of the DBPF.

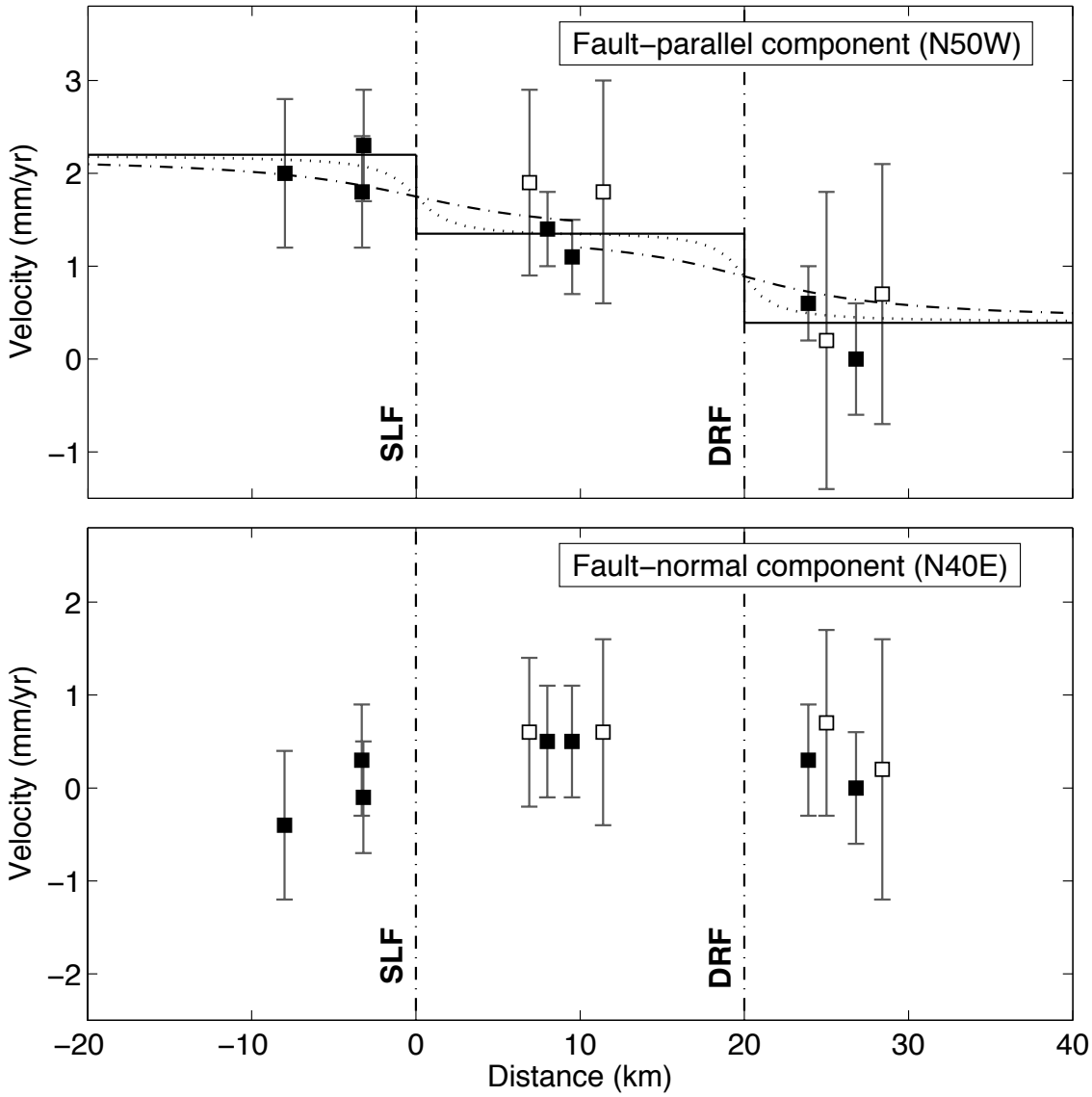

Figure 7.4: GPS velocity profiles (of the zone shown in Figure 3.1) across the SLF and DRF. (top) Velocity component in N50W direction plotted along the same direction, which is the fault-parallel component. The black solid line corresponds to the creeping case (zero locking depth) with slip rate of ∼1.0 mm/yr. The dotted lines are the best estimates of locking depths (for SLF 1.5 km and DRF 1.3 km). The dot-dashed lines present the deeper locking cases ($+1\sigma$ deviation) of SLF and DRF with depths of 7 - 8 km. The estimated model parameters for the SLF and DRF are presented in Table 7.1. (bottom) Velocity component in N40E direction plotted along the profile. It is the fault-normal component with extension positive. Black and white squares indicate sites with long and short observation intervals, respectively (Table 3.1). Error bars are for the 95% confidence level. The vertical dot-dashed lines delineate the location of the SLF and the DRF.

7.3.2 Locking depths of the DBPF, SLF, and DRF zones

According to equations (7.3 and 7.4), fault slip rate and locking depth can be used to estimate both the strain rate and seismic moment accumulation rate along a fault. With adequate seismicity and geodesy data sets, the locking depth is largely consistent with maximum seismicity depth of fault (Smith-Konter et al., 2011). The seismic moment (M_o) is a measure of the size of an earthquake proportional to the area (A) of fault rupture that defined as the product of rupture length (L) and width (W). It is defined by the following formula

$$M_o = \mu \times D \times A \tag{7.9}$$

where μ is the shear modulus, D is the average displacement across the rupture plane.

The maximum fault depth is considered as the locking depth, the fault segment length is assumed twice as the fault depth (Geller, 1976) or is defined by geologic analysis as introduced in chapter 2, and the fault slip rate are all used to estimate the earthquake potential of the fault. Thus, accurate estimate of fault slip rate and locking depth is fundamental in accurately future earthquake prediction.

A question about the relative motion across fault zones is whether those faults are locked or creeping. If a fault is locked, the velocity pattern is continuous across it, but a step-wise discontinuity appears if the fault is creeping (Savage and Burford, 1973). The steep gradient in the velocity field defines a zone of strain concentration and the locking depth of the fault. We investigate a two-dimensional calculation of surface deformation with an elastic half-space model. We assume the segments of SLF and DRF that delimit the profile zone (Figure 3.1) and the DBPF to be vertically dipping, based on structural exploration data (Minh et al., 2009, 2011). These studies have investigated on the deep geoelectric structure of the fault zones by magnetotelluric sounding. By using site velocities, their uncertainties presented in Table 5.2 that used to calculate the weighting factors for inputting data of the model, and distances to the fault, we estimate the relative motion and locking depth of fault by minimizing the residuals through a weighted least-squares inversion. The reduced χ^2, defined as the sum of the squared, weighted residuals divided by the number of degrees of freedom, is used to evaluate the consistency of the fit. Here we define the reduced χ^2 as

$$\chi^2 = \frac{1}{r}\sum_{i=1}^{N}\frac{(y_f - y_i)^2}{\sigma_i^2} \tag{7.10}$$

where y_f is the model estimate (the fit), y_i is the actual measurement, σ_i is the uncertainty in the individual measurement y_i, $r = (N - n)$ is the number of degrees of freedom, and n is the number of coefficients of the model. The estimated model pa-

rameters are presented in Table 7.1. In Figure 7.4, three curves corresponding to the best estimate of locking depth, a total creeping case (zero locking depth), and a deeper locking case ($+1\sigma$ deviation) are shown. All these curves match the observation within the uncertainties, suggesting the model is not well constrained.

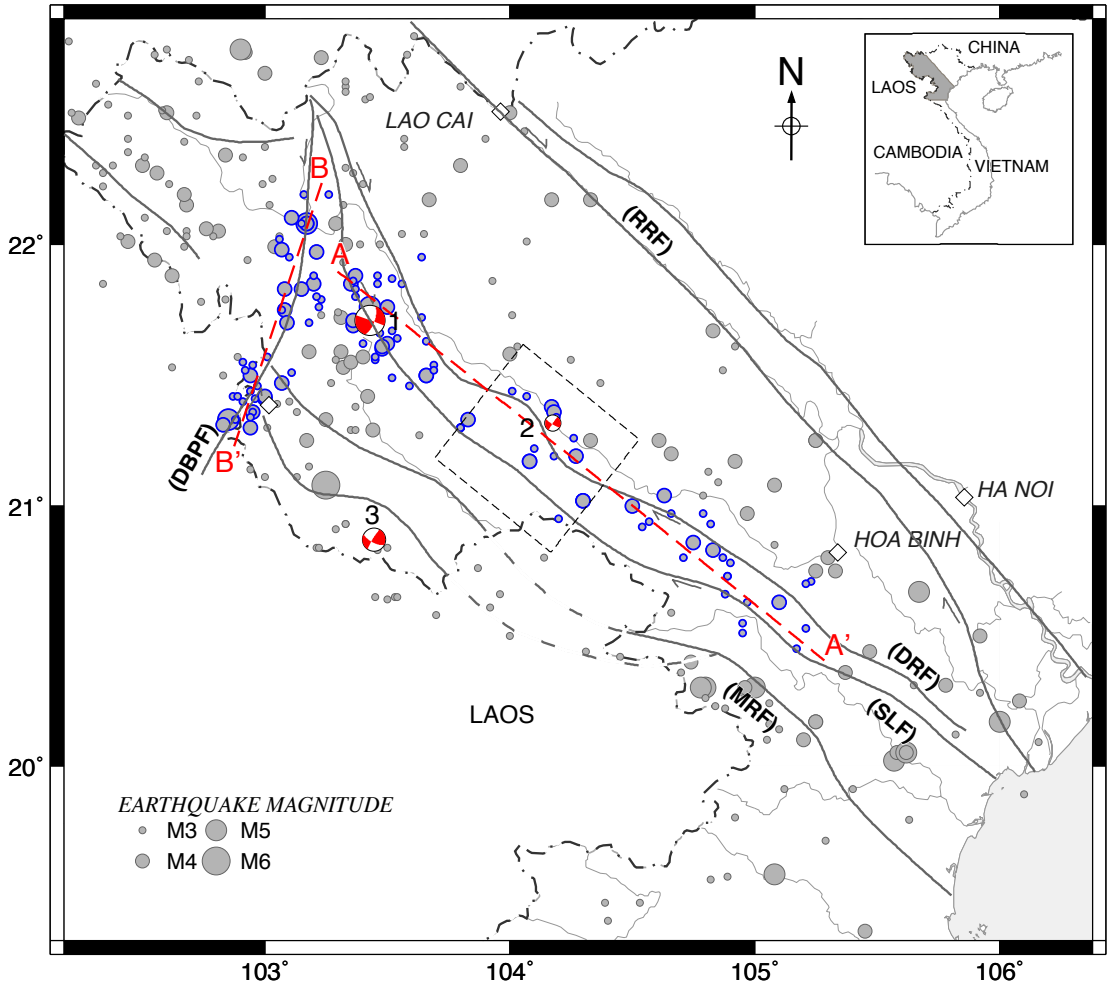

Figure 7.5: Map of seismicity and cross-section lines along the DBPF, SLF, and DRF zones. Earthquakes with local magnitude 3.0 - 6.8 occurred from 1903 to April 2012 along the fault zones and their vicinities. Thick open circles indicate earthquakes within 10 km from the fault traces. Dashed lines (AA' and BB') are the cross-section locations that are shown in Figure 7.6, 7.7, and 7.8. The focal mechanisms are of (1) the 1983 Tuan Giao earthquake M_w6.2; (2) the 2009 Muong La earthquake M_w3.6; (3) the 2010 Sop Cop earthquake M_w4.8. Rectangle with dashed line shows the profile zone of the GPS sites in Figure 7.4. Some descriptions are the same as Figure 7.2.

In the profile zone, only small earthquakes have been observed with maximum magnitude of 4.8 historically. Also, even in the deeper locking case ($+1\sigma$ deviation), the locking depth is only 7 - 8 km, which is quite shallow compared to faults worldwide such as the San Andreas fault system where geodetically determined locking depths range

Table 7.1: Dislocation models for the SLF, DRF and DBPF based on the GPS data in NWV.

Fault	Slip rate (mm/yr)	Locking depth (km)	χ^2
SLF	0.9 ± 0.6	1.5 ± 6.0	0.95
DRF	1.0 ± 0.6	1.3 ± 5.5	1.08
DBPF	1.8 ± 0.3	15.3 ± 9.8	1.23

from 6 to 22 km (Smith-Konter et al., 2011). So the central SLF and DRF could be creeping that the possible depth range of the creeping could not infer from the available GPS measurement data. On the other hand, the largest 1983 Tuan Giao earthquake (M_w6.2) occurred in northern portion of SLF (Figure 3.1) where may represent a locked zone. While, no large earthquakes have ever been recorded on the segment in the profile zone, south of the earthquake. This may imply spatial variability of locking condition along the fault. Discriminating between the creeping and locking models for SLF and DRF is difficult with the current geodetic network of lacking GPS sites near the faults. We take into account the hypocenter distribution of all events with magnitude greater than 3.0 that occurred along SLF and DRF from 1903 to April 2012 (Figure 7.5) to compare with the geodetically estimated locking depths of those faults. According to the earthquake catalog, the accuracy of the focal depth is 1 km. The earthquakes in the profile zone occur only in the earth's crust at depths not exceeding 10 km, and maximum focal depths vary in different zones (Figure 7.6). There are only two hypocenters with depths greater than 10 km in the profile zone of DRF (Figure 7.7). If seismogenic thickness of the profile zone is about 10 km, it is the thinnest along strike of the faults from A to A', because the hypocenters with deeper depths distribute outside of the profile zone (Figure 7.6 and 7.7). Many scientists have proven that the seismogenic thickness of an active fault can vary significantly along its strike due to contribution of crustal temperature and composition (e.g., Peterson et al., 1996; Magistrale, 2002; Wdowinski, 2009). However, there is no study about the heat flow as well as the composition of the crust in this profile zone to clarify this matter. The deeper locking depth (7 - 8 km) of SLF and DRF in the profile zone may seem too shallow compared to the depths of earthquakes with M $\geq$ 3 (Figure 7.6 and 7.7). However, earthquake partially ruptures below a faults locking depth (Shaw and Scholz, 2001; Shaw and Wesnousky, 2008; Wdowinski, 2009). It is possible the invalid of 'classic' locked-fault model here as Wdowinski (2009) suggested.

For the DBPF, the inversion reveals a locking depth and slip rate of 15.3 ± 9.8 km and 1.8 ± 0.3 mm/yr, respectively. Three curves corresponding to locking depths of 5.5, 15.3, 25.1 km (the best estimate and 1σ deviations) are plotted in Figure 7.3.

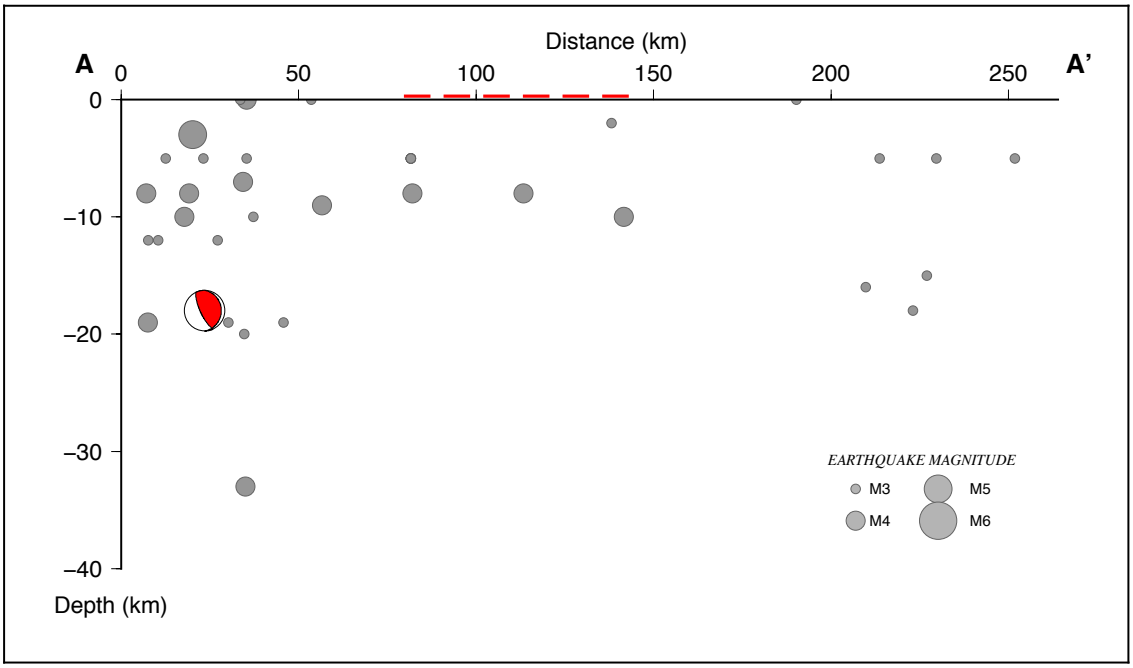

Figure 7.6: Seismicity as a function of depth is along the SLF zone within 10 km width, which is profiled from A to A'. Dashed line shows location of the profile zone where AA' goes through (Figure 7.5). The focal mechanism is of the 1983 Tuan Giao earthquake M_{w}6.2.

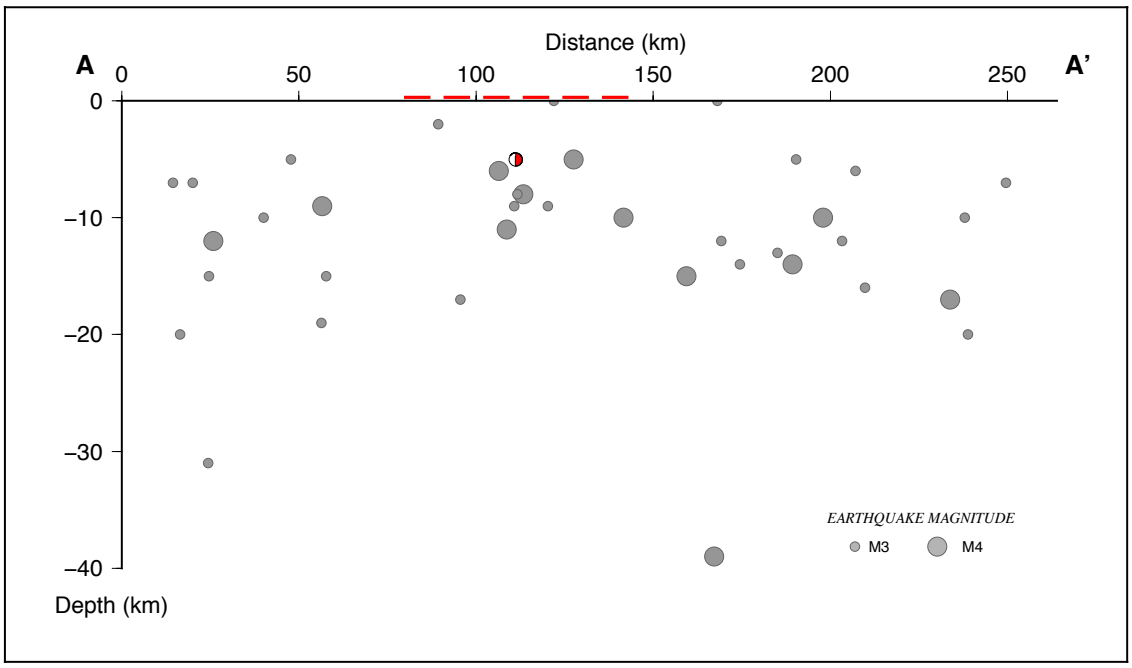

Figure 7.7: Seismicity as a function of depth is along the DRF trace within 10 km width, which is profiled from A to A'. Dashed line shows location of the profile zone where AA' goes through (Figure 7.5). The focal mechanism is of the 2009 Muong La earthquake M_{w}3.6.

Seismicity for the DBPF zone from 1903 to April 2012 with magnitude ≥ 3.0 is plotted in Figure 7.8. Hypocenters with depths less than 5.5, 15.3 and 25.1 km depth are 49%, 91% and 98% of all events with magnitude greater than 3.0 that occurred along DBPF, respectively. If the seismogenic depth is defined as the depth above that 90% of the earthquakes occur (D90), which is not easily influenced because of a few hypocenters with poor depth determine, the geodetically estimated locking depth is consistent with the depth distribution of crustal earthquakes. It means that seismogenic and locking depth are similar, about 15.3 km, indicating that the DBPF is locked throughout its entire seismogenic depth. The locking depth of 15.3 km is also consistent with the magnetotelluric sounding result in the DBPF zone estimated by Minh et al. (2009), in which the ductile regime was estimated at depth of 20 - 30 km. From these results, we can infer that the locking depth of 15.3 km for DBPF is reliable estimate. In spite of the sparse GPS network, the geodetic measurements in this work are sufficient to determine the current pattern of locking along the strike of DBPF for comparison with the previous studies such as Duong et al. (2006) and Lai et al. (2012).

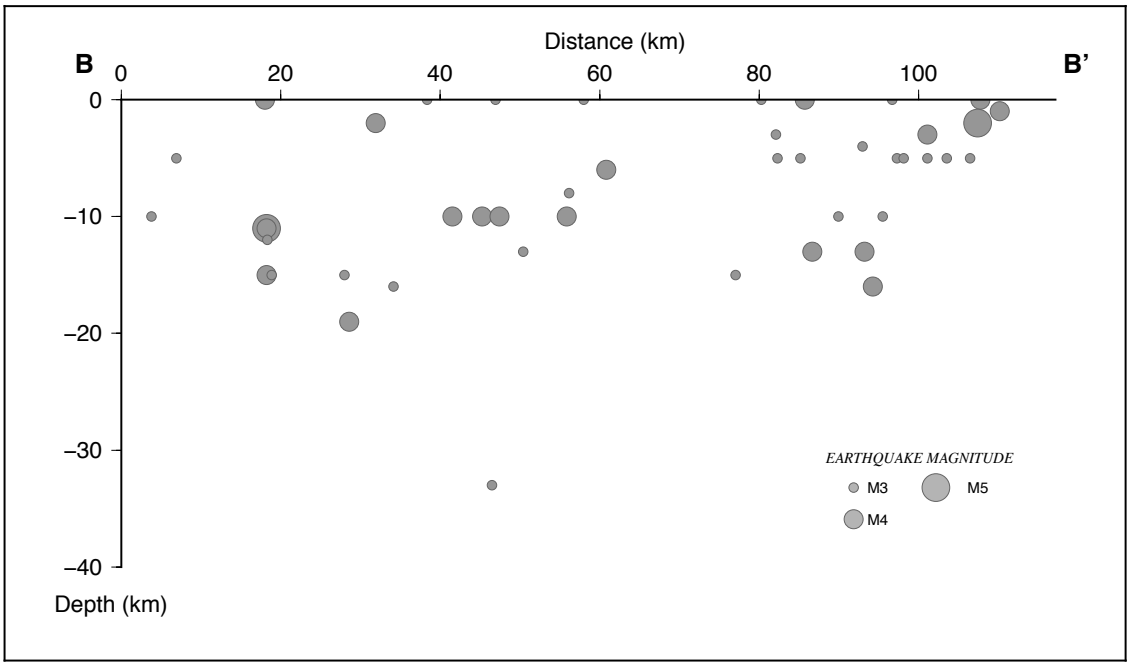

Figure 7.8: Seismicity as a function of depth is along the DBPF zone within 10 km width, which is profiled from B to B' (Figure 7.5).

The fault slip rate results show that there are no significant discrepancies between short-term slip rates inferred from GPS measurements and long-term slip rates investigated by geology. The agreement between short- and long- term slip rates imply that GPS-derived fault slip rates is correct properly simplifications in fault geometry, and

fault model fitting to velocity data, as well as the geologic estimates of long-term slip rate were investigated in representative locations along the faults (Marshall et al., 2013). During the interseismic period, GPS-derived fault slip rate estimated from the pattern of surface strain accumulation can be considered as the long-term slip rate of fault (e.g., Savage and Burford, 1973; Lisowski et al., 1991; Schmalzle et al., 2006).

7.3.3 Strain rate field in NWV

We utilize the distance-weighted approach to compute strain rate on a surface that is set out as a regularly spaced grid. At the center of each cell of the grid, the strain rate is calculated using velocities of GPS sites that are weighted by their distance to the center of the cell. The average strain rate is calculated for NWV from all GPS sites using the the least-squares method. The sites are weighted equally in the calculation. Result that the maximum strain rate is 2.4×10^{-8} per year, similar value has been obtained in NWV from the global strain rate model of Kreemer et al. (2000). Based on the analysis of the strain-rate tensors in Southeast Asia reported by Simons et al. (2007), NWV is a deformation zone of moderate strain rate, much lager than 7×10^{-9} per year that represents the undeformed interior of SU. The principal compresive axis is the NNW-SSE direction (N342°E). It is good correspondence with tectonic deformation during the Pliocene - Quaternary times with the predominately sub-longitude compressive stress field reflected by the long-term geological survey (Hung, 2002; Thuy, 2005).

The parameter D in equation (7.8) that controls the weight depends on the tectonic deformation features and spatial distribution of GPS sites (Sagiya et al., 2000). Basing on the equation (7.8), we plot the correlation between horizontal weighted observational errors and the Distance Decaying Constant (D), using the distance between the observation points (Figure 7.9). The result shows that the horizontal weighted observational error is proportional to D. We test several values for D and recognize that the area of the significant strain rates being greater than their 1σ uncertainties is also proportional to D. It means that the strain rates are smoother as D increases, reflecting the overestimated strain rates at places with sparse observation points. We apply $D =$ 19 km as a standard value corresponding to the horizontal weighted observational error of 0.1 mm/yr that is the same as the minimum horizontal original observational error.

We plot distribution of estimated principal strain rate axes, dilatational strain rate, and maximum shear strain rate in Figure 7.10, 7.11, and 7.12. In these figures, the strain rates being greater than their 1σ uncertainties are considered as the significant values that are denoted inside the zones bordered by the green lines. The estimated principal axes of strain rates remarkably present consistent with the geological structures of the

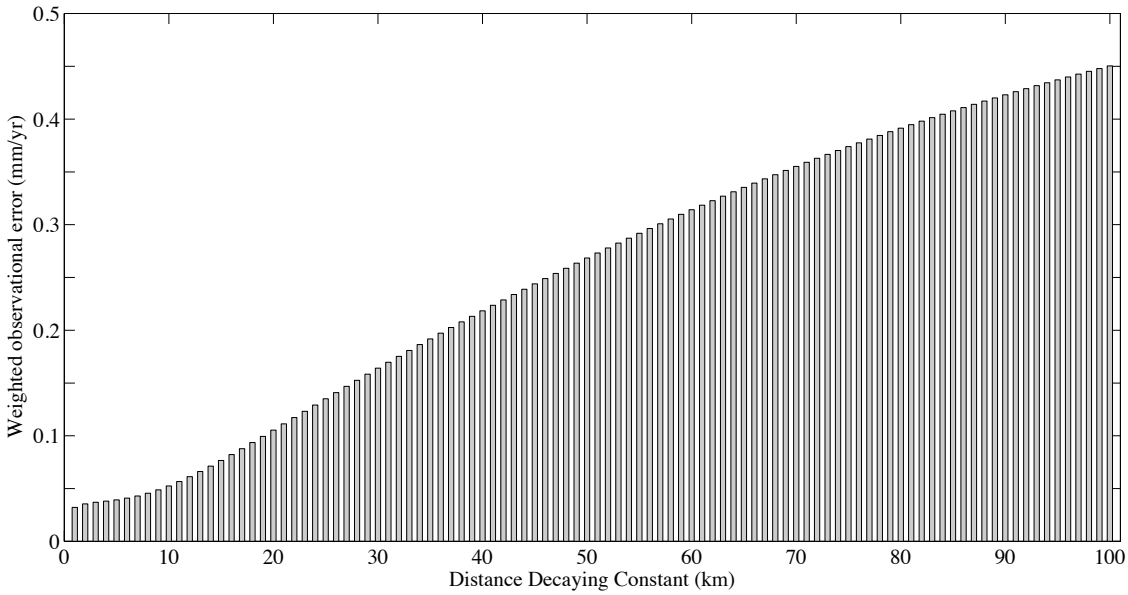

Figure 7.9: Horizontal observational errors weighted by the distance between the observation points depend on the Distance Decaying Constant.

region (Figure 7.10). The shortening rate axes are perfectly oriented at 45° to the fault traces for right-lateral slip on the SLF, DRF and for left-lateral on the DBPF. The principal strain rate axes (NW-SE compression of 1.3×10^{-8} per year, NE-SW expansion of 1.8×10^{-8} per year) estimated near the 1983 Tuan Giao earthquake ($M_{\mathrm{w}}6.2$) and (N-S compression of 1.5×10^{-8} per year, E-W expansion of 2.9×10^{-8} per year) near the 2009 Muong La earthquake ($M_{\mathrm{w}}3.6$) are compatible with their source mechanisms. The 2010 Sop Cop earthquake ($M_{\mathrm{w}}4.8$) is outside of the estimated strain rate zone, however, the trending of the principal strain rate axes is probably suited to its source mechanism. Moreover, the magnitude of extension rates gradually increases toward the southwest from the northeast of the 2009 Muong La earthquake ($M_{\mathrm{w}}3.6$). It infers that the normal faulting component gradually prevails toward the southwest. It is obviously in the focal mechanism of the 2010 Sop Cop earthquake ($M_{\mathrm{w}}4.8$) comparing with that of the 2009 Muong La earthquake ($M_{\mathrm{w}}3.6$). There are only three focal mechanisms plotted in Figure 7.10 to compare with the estimated strain rates, however, they match each other. It implies that the estimated principal strain rate axes can use to discuss the tectonic deformation axes in NWV. In the profile zone, southern side of SLF and northern side of DRF represent extension and compression regions, respectively. It is consistent with the velocity changes in the fault-normal component plotted along the profile (Figure 7.4- bottom). So the area between SLF and MRF, near Vietnam-Laos border is less seismicity than that of the northeastern profile. The largest strain rate but being extension rate is in the border area of Vietnam-Laos where earthquakes are rare (Figure 7.10). An explanation suggests that an area with large extension but very small compression strain rates reflects an aseismic region that produces less seismicity

such as the region between the 1983 Tuan Giao earthquake and the profile zone.

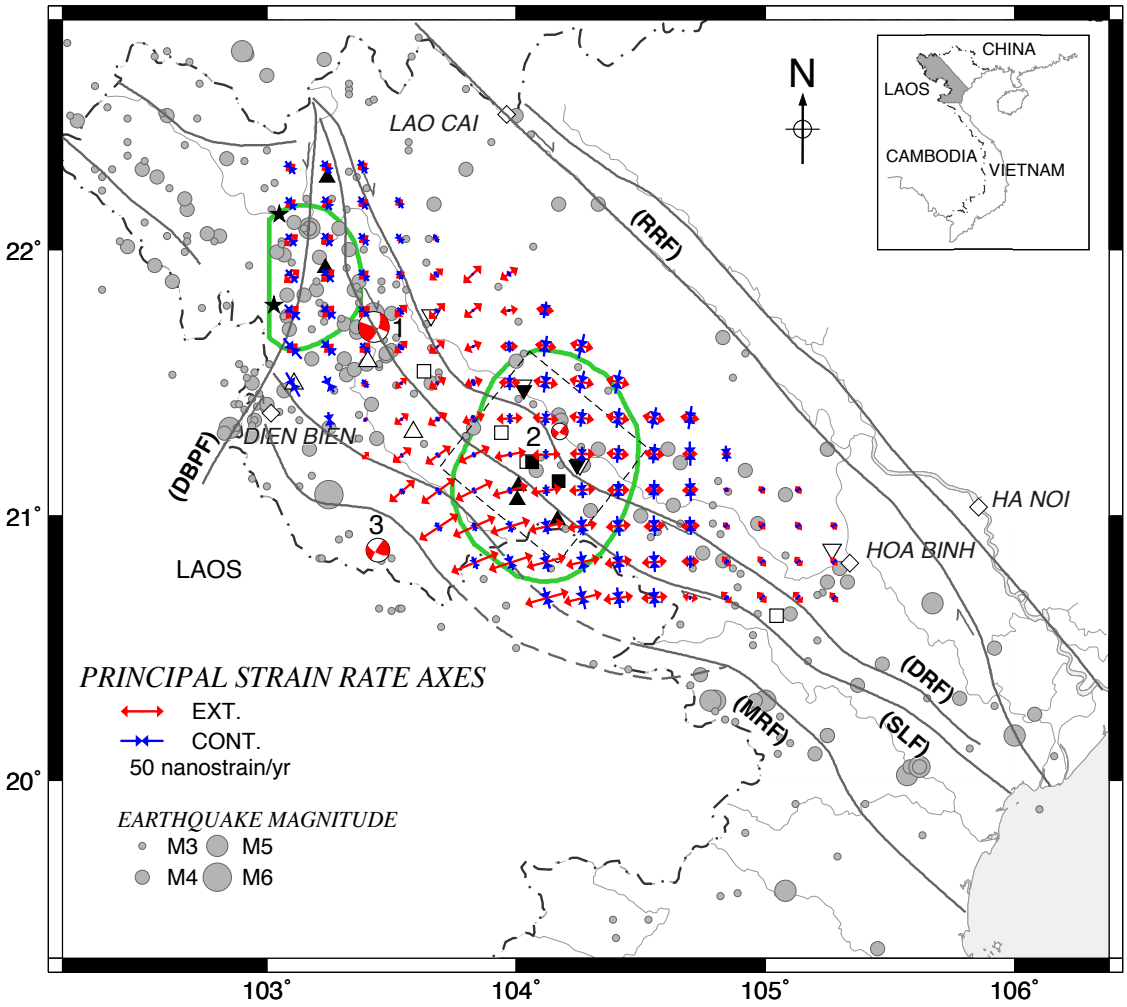

Figure 7.10: Estimated principal axes of strain rates. The strain rates inside the zones bordered by the green lines are significant which are greater than their 1σ uncertainties. The focal mechanisms are of (1) the 1983 Tuan Giao earthquake M_w6.2; (2) the 2009 Muong La earthquake M_w3.6; (3) the 2010 Sop Cop earthquake M_w4.8. Some descriptions are the same as Figure 7.2.

Figure 7.11 and 7.12 are estimated dilatational strain rate and maximum shear strain rate distributions, respectively. Dilatational strain rate can be considered as representative of horizontal deformation related to dip-slip faulting. Maximum shear strain rate can be related to strike-slip faults. In Figure 7.11, compressive tectonics is evident in the northwest part of estimated strain area where the seismic activity is the highest in NWV. The contraction increases toward the Dien Bien city and this state may extend to the southwestern city. It may be related to the subsidence of the Dien Bien basin with Pleistocene - present rates of 0.25 - 1 mm/yr (Tung, 2011). While, high extension tectonics exists in the same parts as discussed above in the principal strain

rate axes map, such as the east of the 1983 Tuan Giao earthquake and the southwest of the NAH2 site. Large extension is found in the southwest of GPS network and it increases to the southwest where has a low seismic productivity.

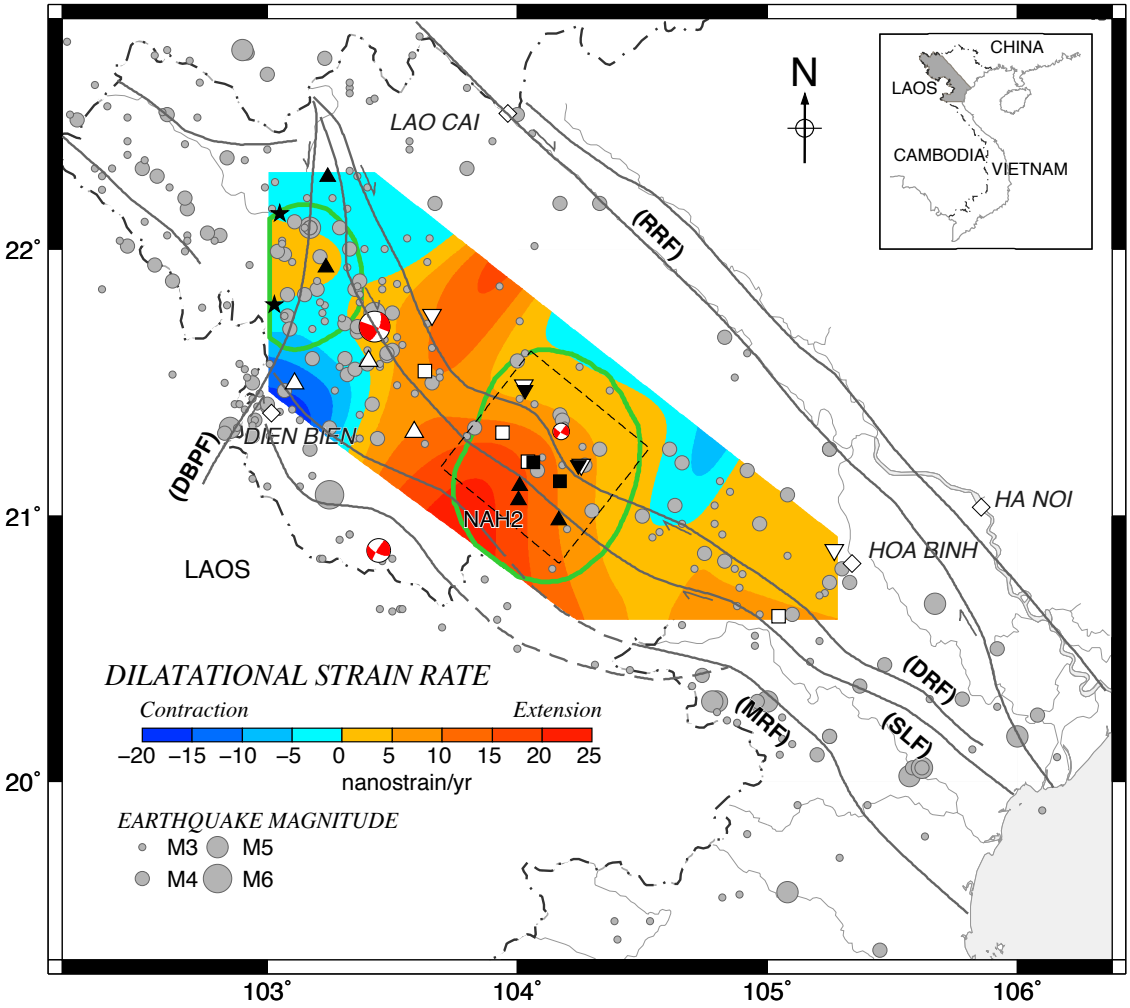

Figure 7.11: Estimated distribution of dilatational strain rate. Some descriptions are the same as Figure 7.2 and 7.10.

In Figure 7.12, maximum strain rate shows a similar tendency of dilatation strain rate distribution, however, the magnitude of maximum strain rate is basically larger than that of the dilatation strain rate. It implies that extension tectonics is generally in the NWV region. The peak shear strain rate of 1.8 $\times$ 10^{-8} per year for DBPF calculated across the fault in the dislocation model (Table 7.2) is within the bound of maximum strain rate (1.5 $\times$ 10^{-8} - 2.4 $\times$ 10^{-8} per year) estimated in the area of GPS sites distributed along the DBPF zone. Similarly, the peak shear strain rates of 1.9 $\times$ 10^{-8} per year for SLF and 2.3 $\times$ 10^{-8} per year for DRF (Table 7.2) are within the bound of maximum strain rate (1.9 $\times$ 10^{-8} - 2.7 $\times$ 10^{-8} per year) estimated in the

profile zone between the GPS sites installed along the SLF and DRF zones. They are reasonable estimates, because the peak shear strain rate estimated across the single fault by the dislocation line model with considering the natural locking of the fault is always smaller than the maximum shear strain rate caused by the dislocation surface that might represent the area of decoupling. The maximum strain rate gradually increases from north to south along the DBPF zone. It implies that the magnitude of left-lateral strike-slip increases as the same direction, which is agreement with geologic result of Tung (2011).

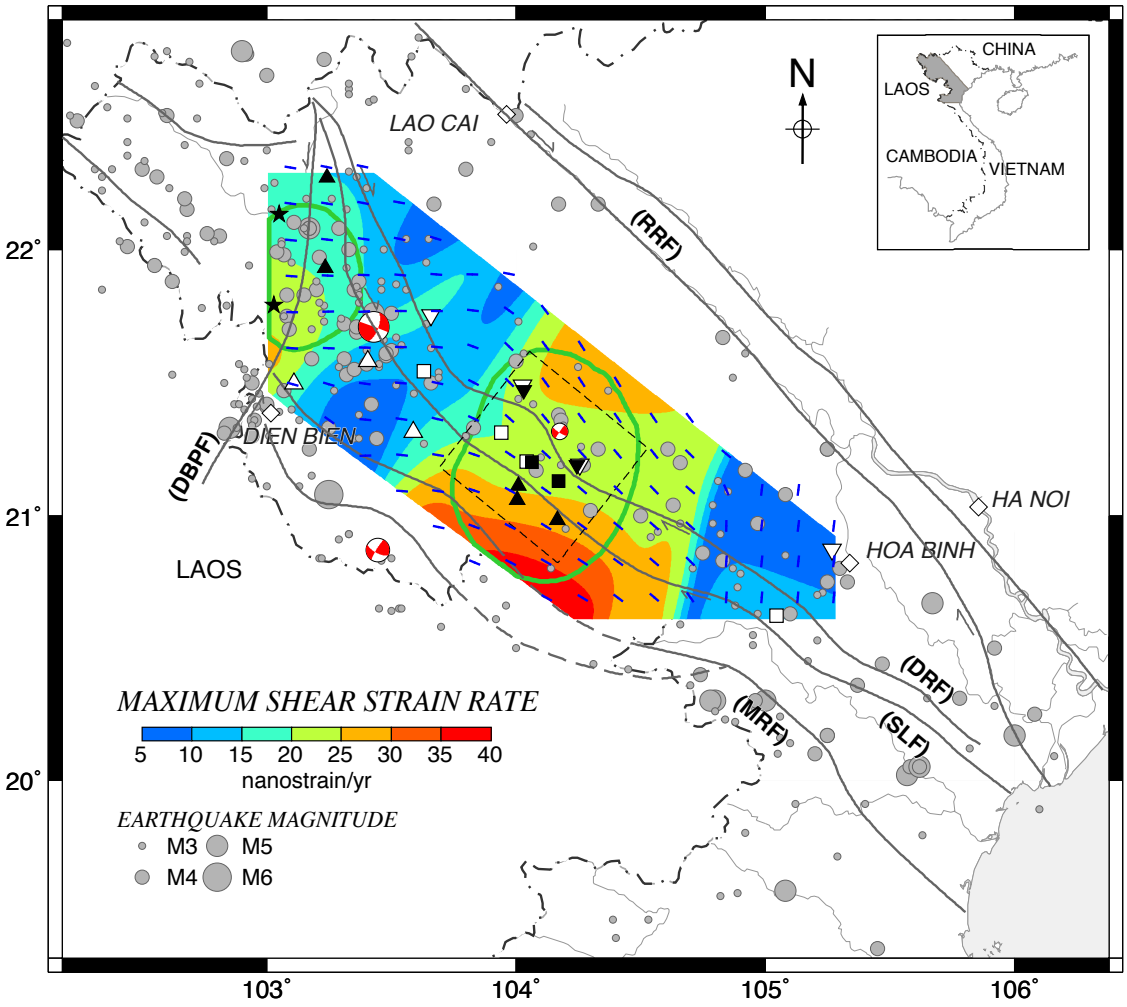

Figure 7.12: Estimated maximum shear strain rate distribution. Blue bars denote direction of maximum right-lateral shear. Left-lateral shear is the largest in the conjugate direction. Some descriptions are the same as Figure 7.2 and 7.10.

Maximum right-lateral shear inferred from the strain rate distribution is also shown in this figure. It matches the strike of active faults trending NW-SE direction such as SLF and DRF. Direction of maximum right-lateral shear is consistent with the right-lateral strike-slip focal mechanism of the 1983 Tuan Giao earthquake (M_w6.2). However,

this source mechanism does not match the SLF trace, implying the complicated geological structure in this area. It can explain that the event may occur in a subsidiary branch of SLF. Thus, it is necessary to study in detail on the geological structure of this area. The trend of maximum right-lateral shear in the west of Hoa Binh city does not matches the strike of SLF and DRF, however, we do not have any focal mechanism in this area to explain this difference. Additionally, left-lateral shear is the largest in the conjugate direction of maximum right-lateral shear. It is obviously that the left-lateral shear matches the strike of DBPF.

7.3.4 Earthquake potential assessment along the DBPF, SLF, and DRF zones

The earthquake potential assessment is necessary to seismic hazard analysis and earthquake mitigation. The strain rates, moment accumulation rates, maximum magnitude of seismic events and their recurrence intervals will be estimated for DBPF, SLF, and DRF. For this purpose, we apply some empirical relationship regressions and use the fault slips and locking depths estimated above.

Moment magnitude (M_{w}) is calculated from rupture area (A) by the equation for strike-slip fault type (Wells and Coppersmith, 1994) produced the empirical relationship between moment magnitude (M_{w}) and rupture area (A) for strike-slip faults

$$M_{\mathrm{w}} = 3.98 + 1.02 \log A \tag{7.11}$$

Hanks and Kanamori (1979) constructed the empirical relationship between seismic moment (M_o) and moment magnitude (M_{w}) as follow

$$\log M_o = 1.5 M_{\mathrm{w}} + 16.1 \tag{7.12}$$

The rupture fault area (A) is the product of rupture fault length (L) and down-dip rupture fault width (W). Rupture fault length and width associated strike slip earthquakes are empirically found by approximate relationship $L = 2W$ (Geller, 1976). The maximum fault depth is considered as the locking depth, the fault segment length is assumed twice as the fault depth (Geller, 1976) or is defined by geologic analysis as introduced in chapter 2, and the fault slip rate are all used to estimate the earthquake potential of the fault. If the down-dip rupture fault width is equal to the estimated locking depth, the rupture fault length is inferred approximate twice the estimated locking depth. It is assumed that the fault plane dip is 90° for the investigated faults. We apply

the deeper locking depths (7.5 km and 6.8 km) for the profile zone of SLF and DRF, respectively, and the locking depth of 15.3 km for DBPF, associated fault slip rates to calculate the strain rate, seismic moment accumulation rate for the faults, using the equations (7.3 and 7.4). Estimate of potential earthquake magnitude is made for the fault by substituting the estimated rupture fault area (A) in equation (7.11). The size of the largest earthquake is actually very uncertain for the estimation. So we assume that the largest one can be within a range of maximum magnitude. If the estimated locking depth is considered as the maximum fault depth and the fault length is assumed twice as the maximum fault depth (Geller, 1976), the estimated earthquake magnitude can be the maximum earthquake magnitude at the lowest of range in the investigated zone of fault. These fault zones are much longer than the above assumed fault lengths. Thus we also consider a case that the whole DBPF zone divided into three segments by geologic analysis as introduced in chapter 2 ruptures at once as the case of the 2008 Wenchuan earthquake M_{w}7.9 (e.g., Burchfiel et al., 2008) in China. For the SLF and DRF zones, we cannot calculate for whole fault zones because our investigation only focuses in the profile zone of the faults, so the locking depths calculated in the profile cannot represent for such whole fault zone. Besides, it is clearly that the recurrence interval of earthquake is not an independent value. Thus, to determine the recurrence interval of the earthquake with estimated magnitude, we calculate the seismic moment release using the equation (7.12), and then divide by the estimated seismic moment accumulation rate. The results are presented in Table 7.2. Based on our estimates, earthquakes with maximum magnitude as large as 6.0 could be generated every four or five hundred years with ruptures along SLF and DRF in the profile zone. However, only events have been observed with maximum magnitude of 4.8 historically within 100 years in the profile zone. While the DBPF zone could repeatedly rupture events every 566 years with magnitude probably reaching 6.7 or every 1338 years with maximum magnitude of 7.4. Our earthquake catalog shows that maximum observed event is only of $M_{\mathrm{s}} = 5.3$ (Son, 2004) or $M_{\mathrm{w}} = 5.1$ (Van, 2006) in this fault zone. There are two earthquakes with magnitude size of > 6.0 occurred in NWV, but these events are not related to the DBPF zone (Figure 3.1).

Table 7.2: Fault source parameters and earthquake potential of SLF, DRF, and DBPF.

Fault	Segment of fault	W (km)	L (km)	Slip rate (mm/yr)	Strain rate (/yr)	Seismic moment accumulation rate per unit length of fault (Nm/yr)	M_{w}	Seismic moment release (Nm)	Earthquake recurrence interval (yr)
SLF	$L = 2W$	creeping	-	0.9	-	-	no eq.	-	-
	$L = 2W$	1.5	3.0	0.9	9.55E-08	4.05E+10	4.6	1.17E+16	97
	$L = 2W$	7.5	15.0	0.9	1.91E-08	2.03E+11	6.1	1.62E+18	532
DRF	$L = 2W$	creeping	-	1.0	-	-	no eq.	-	-
	$L = 2W$	1.3	2.6	1.0	1.22E-0.7	3.90E+10	4.5	7.57E+15	75
	$L = 2W$	6.8	13.6	1.0	2.34E-08	2.04E+11	6.0	1.20E+18	431
DBPF	$L = 2W$	5.5	11.0	1.8	5.21E-08	2.97E+11	5.8	6.25E+17	191
	$L = 2W$	15.3	30.6	1.8	1.87E-08	8.26E+11	6.7	1.43E+19	566
	$L = 2W$	25.1	50.2	1.8	1.14E-08	1.36E+12	7.1	6.51E+19	957
	Segment 1	15.3	50.0	1.8	1.87E-08	8.26E+11	6.9	3.03E+19	734
	Segment 2	15.3	35.0	1.8	1.87E-08	8.26E+11	6.8	1.76E+19	608
	Segment 3	15.3	70.0	1.8	1.87E-08	8.26E+11	7.1	5.08E+19	878
	Whole	15.3	155.0	1.8	1.87E-08	8.26E+11	7.4	1.71E+20	1338

(Segment 1: Ma Lu Thang – Chan Nua; Segment 2: Chan Nua – Huoi Leng;
Segment 3: Huoi Leng – Thin Toc; Whole = Segment 1+Segment 2+Segment 3 (Figure 2.1))

Chapter 8

CONCLUSION AND FUTURE WORK

This dissertation has been concerned with the geodetic measurement and interpretation of crustal deformation in an extensional tectonic setting. It is aimed at utilizing the GPS measurements in order to clarify the tectonic affiliation of NWV and constrain crustal deformation across the major fault as well as implications for the potential of earthquake hazard. A sequence of researches has been carried out in this dissertation. First, all the GPS measurement data in this region have been analyzed to obtain coordinate time series for each GPS site. Next, the coseismic offsets due to the great earthquakes (the 2004 Sumatra, the 2008 Wenchuan, and the 2011 Tohoku earthquakes) have been calculated and offset the time series. Then the velocity of each GPS site has been calculated in the ITRF2008 reference frame. Finally, the crustal motion of the area has been compared with motions of blocks (SU, SC, EU, and BS); characteristics of major active fault zones such as fault slip rate, locking depth, strain rate, seismic moment accumulation rate, maximum possible earthquake, and earthquake occurrence rate, and strain rate field of the study region have been discussed. Here we summarize the sets of conclusions and their implications to each other, which have been made individually in the preceding chapters.

We have analyzed GPS campaign data collected at 22 sites in NWV spanning from 2001 to 2012 in ITRF2008 with a consideration of far-field coseismic displacements caused by the 2004 Sumatra, the 2008 Wenchuan, and the 2011 Tohoku earthquakes. We find that the horizontal displacements in NWV from the 2008 Wenchuan earthquake are smaller than 1 mm, so that they are negligible; the 2004 Sumatra earthquake caused southwestward movement of about 15 mm; while the 2011 Tohoku earthquake moved the area in the opposite direction, by 1.2 mm to the east and 0.5 mm to the north. As a result, consideration of the coseismic effects of the latter two earthquakes reduces

the horizontal velocity components by 1.0 ± 0.2 mm/yr. It is small but significant for regional deformation between SC and SU whose relative motion is as small as 4 mm/yr.

From our analysis, we recognize the left-lateral motion of about 2 mm/yr across the DBPF, and a right-lateral shear of 1 - 2 mm/yr across SLF and DRF. Our result is consistent with geological studies. In addition, we show for the first time spatial variation of the fault slip-rate along the DBPF. Although the GPS network is still sparse, the displacement patterns across these fault zones fit well with a locking depth of 15.3 ± 9.8 km and slip rate of 1.8 ± 0.3 mm/yr for DBPF, and a shallow locking depth (with a large uncertainty) with a right-lateral slip rate of about 1.0 ± 0.6 mm/yr for SLF and DRF. The hypocenters of 91% of the earthquakes fall at depths less than 15.3 km along the DBPF. Further densification of the GPS network is necessary to estimate more detail of the fault behavior in NWV.

NWV is moving independently from the stable Eurasia plate with a secular motion of 34.3 ± 0.7 mm/yr to the azimuth of N108° ± 0.7°E in ITRF2008. NWV can be considered as a part of transition boundary zone among three blocks, SC, SU, and BS, although its motion is close to that of SC. The relative motion between SC and SU is partly accommodated by the NW-SE trending fault zones such as SLF, DRF, and RRF, but other faults as far south as site NONN in central Vietnam could be also responsible. Therefore, in order to clarify the deformation accommodation style between SC and SU, it is necessary to expand the GPS network to the south of the current study area.

From strain rate field analysis, we find that the focal mechanisms match the estimated strain rates and the estimated principal strain rate axes can use to discuss the tectonic deformation axes as well as the seismicity in NWV. The study area is within the extensional tectonic setting with the maximum strain rate of 2.42×10^{-8} per year in average that is the moderate strain rate in Southeast Asia. The principal compressive axis is the NNW-SSE direction (N342°E) that is consistent with the geological studies. Moreover, the maximum right- and left-lateral shears match the strikes of active faults trending NW-SE direction such as SLF and DRF and trending sub-longitudal such as DBPF, respectively.

For earthquake hazard assessment purpose, the strain rates, seismic moment accumulation rates, potential earthquake magnitudes and associated recurrence intervals are estimated for DBPF, SLF, and DRF by using their fault slip rates and locking depths. Based on our final estimates (Table 7.2), earthquakes with maximum magnitude as large as 6.0 could be generated every four or five hundred years with ruptures along SLF and DRF in the profile zone that is plotted in Fig 3.1. While the DBPF zone could repeatedly rupture events every 566 years with magnitude probably reaching 6.7 or every 1338 years with maximum magnitude of 7.4.

This dissertation has proved that surveying of the NWV network with GPS is capable of detecting crust deformation over short time-scale and analyzing seismic hazard. However, many sites of the network have only been occupied with short observation spans. To obtain better estimates of crust strain in these parts of the network, it will be necessary to reoccupy more sites as well as to deploy more new sites between the existed ones.

The earthquake occurrence rate, an important part of seismic hazard assessment, can be also estimated by using historical seismicity. In this study, the earthquake occurrence rates of the faults have been determined, however, a comparison of the two approaches is necessary. Thus, estimate of the seismicity-derived earthquake occurrence rates of the faults should be conducted in the further work.

Bibliography

Allen, C. R., A. R. Gillespie, Han Yuan, K. E. Sieh, Zhang Buchun, and Zhu Chengnan, 1984. Red River and associated faults, Yunnan Province, China: Quaternary geology, slip rates, and seismic hazard. *Geological Society of America Bulletin*, 95(6):686–700.

Altamimi, Zuheir, Patrick Sillard, and Claude Boucher, 2002. ITRF2000: A new release of the International Terrestrial Reference Frame for earth science applications. *Journal of Geophysical Research: Solid Earth*, 107(B10):ETG 2(1–19). ISSN 2156-2202. doi: 10.1029/2001JB000561.

Altamimi, Zuheir, Xavier Collilieux, and Laurent Métivier, 2011. ITRF2008: an improved solution of the international terrestrial reference frame. *Journal of Geodesy*, 85(8):457–473. ISSN 0949-7714. doi: 10.1007/s00190-011-0444-4.

Ammon, C. J., T. Lay, H. Kanamori, and M. Cleveland, 2011. A rupture model of the 2011 off the Pacific coast of Tohoku Earthquake. *Earth, Planets, and Space*, 63: 693–696. doi: 10.5047/eps.2011.05.015.

Ammon, Charles J., Chen Ji, Hong-Kie Thio, David Robinson, Sidao Ni, Vala Hjorleifsdottir, Hiroo Kanamori, Thorne Lay, Shamita Das, Don Helmberger, Gene Ichinose, Jascha Polet, and David Wald, 2005. Rupture Process of the 2004 Sumatra-Andaman Earthquake. *Science*, 308(5725):1133–1139. doi: 10.1126/science.1112260.

Avouac, Jean-Philippe and Paul Tapponnier, 1993. Kinematic model of active deformation in central Asia. *Geophysical Research Letters*, 20(10):895–898. ISSN 1944-8007. doi: 10.1029/93GL00128.

Banerjee, P., F. F. Pollitz, and R. Bürgmann, 2005. The Size and Duration of the Sumatra-Andaman Earthquake from Far-Field Static Offsets. *Science*, 308(5729): 1769–1772. doi: 10.1126/science.1113746.

Bird, Peter, 2003. An updated digital model of plate boundaries. *Geochemistry, Geophysics, Geosystems*, 4(3):1027. ISSN 1525-2027. doi: 10.1029/2001GC000252.

Blewitt, Geoffrey and David Lavallée, 2002. Effect of annual signals on geodetic velocity. *Journal of Geophysical Research: Solid Earth*, 107(B7):ETG 9(1–11). ISSN 2156-2202. doi: 10.1029/2001JB000570.

Burchfiel, B. C., 2004. New technology, new geological challenges. *Geological Society of America: GSA Today*, 14(2):4–10.

Burchfiel, B. C., L. H. Royden, R. D. Hilstvan der , B. H. Hager, Z. Chen, R. W. King, C. Li, J. Lu, H. Yao, and E. Kirby, 2008. A geological and geophysical context for the Wenchuan earthquake of 12 May 2008, Sichuan, People's Republic of China. *GSA Today*, 18(7). doi: 10.1130/GSATG18A.1.

Calais, Eric, Mathilde Vergnolle, Vladimir San'kov, Andrei Lukhnev, Andrei Miroshnitchenko, Sharavyn Amarjargal, and Jacques Déverchère, 2003. GPS measurements of crustal deformation in the Baikal-Mongolia area (1994–2002): Implications for current kinematics of Asia. *Journal of Geophysical Research: Solid Earth*, 108(B10):ETG 14(1–13). ISSN 2156-2202. doi: 10.1029/2002JB002373.

Cao, Dinh Trieu, Dang Thanh Hai, Mai Xuan Bach, and Ngo Gia Thang, 2003. Fault system in northern Vietnam. *Journal of Geology, Series A*, 279(11-12):8–19. (in Vietnamese, with English Abstr.).

Cao, Dinh Trieu, Le Van Dung, Pham Nam Hung, Nguyen Huu Tuyen, Mai Xuan Bach, and Thai Anh Tuan, 2004. Main structural units of the Earth's crust in Northwest region of Vietnam. *Journal of Earth Science*, 26(3):244–257. (in Vietnamese, with English Abstr.).

Carter, Andrew, Delphine Roques, Charles Bristow, and Peter Kinny, 2001. Understanding Mesozoic accretion in Southeast Asia: Significance of Triassic thermotectonism (Indosinian orogeny) in Vietnam. *Geology*, 29(3):211–214.

Chen, Z., B. C. Burchfiel, Y. Liu, R. W. King, L. H. Royden, W. Tang, E. Wang, J. Zhao, and X. Zhang, 2000. Global Positioning System measurements from eastern Tibet and their implications for India/Eurasia intercontinental deformation. *Journal of Geophysical Research: Solid Earth*, 105(B7):16215–16227. ISSN 2156-2202. doi: 10.1029/2000JB900092.

Chlieh, Mohamed, Jean-Philippe Avouac, Vala Hjorleifsdottir, Teh-Ru Alex Song, Chen Ji, Kerry Sieh, Anthony Sladen, Helene Hebert, Linette Prawirodirdjo, Yehuda Bock, and John Galetzka, 2007. Coseismic Slip and Afterslip of the Great Mw 9.15 Sumatra–Andaman Earthquake of 2004. *Bulletin of the Seismological Society of America*, 97 (1A):S152–S173. doi: 10.1785/0120050631.

Clarke, P. J., R. R. Davies, P. C. England, B. Parsons, H. Billiris, D. Paradissis, G. Veis, P. A. Cross, P. H. Denys, V. Ashkenazi, R. Bingley, H.-G. Kahle, M.-V. Muller, and P. Briole, 1998. Crustal strain in central Greece from repeated GPS measurements in the interval 1989–1997. *Geophysical Journal International*, 135(1):195–214. ISSN 1365-246X. doi: 10.1046/j.1365-246X.1998.00633.x.

Cohen, S. C., 1999. Numerical Models of Crustal Deformation in Seismic Zones. *Advances in Geophysics*, 41:134–231.

Cox, A. V. and R. B. Hart. *Plate Tectonics: How It Works*, page 392. Blackwell Scientific Publications, Palo Alto, California, 1986.

Dach, R., U. Hugentobler, P. Fridez, and M. Meindl, 2007. Bernese GPS Software Version 5.0. *AIUB, University of Bern.*

Dach, R., U. Hugentobler, P. Fridez, and M. Meindl, 2011. Bernese GPS Software Version 5.0, Tutorial. *AIUB, University of Bern.*

DeMets, C., R. G. Gordon, D. F. Argus, and S. Stein, 1990. Current plate motions. *Geophysical Journal International*, 101:425–478.

DeMets, Charles, Richard G. Gordon, Donald F. Argus, and Seth Stein, 1994. Effect of recent revisions to the geomagnetic reversal time scale on estimates of current plate motions. *Geophysical Research Letters*, 21(20):2191–2194. ISSN 1944-8007. doi: 10.1029/94GL02118.

DeMets, Charles, Richard G. Gordon, and Donald F. Argus, 2010. Geologically current plate motions. *Geophysical Journal International*, 181(1):1–80. ISSN 1365-246X. doi: 10.1111/j.1365-246X.2009.04491.x.

Duong, Chi Cong and K. L. Feigl, 1999. Geodetic measurement of horizontal strain across the Red River fault near Thac Ba, Vietnam, 1963-1994. *Journal of Geodesy*, 73(6):298–310. ISSN 0949-7714. doi: 10.1007/s001900050247.

Duong, Chi Cong, H.-S. Yun, and J.-M. Cho, 2006. GPS measurements of horizontal deformation across the Lai Chau-Dien Bien (Dien Bien Phu) fault, in Northwest of Vietnam, 2002-2004. *Earth, Planets, and Space*, 58(5):523–528.

Dziewonski, A. M. and D. L. Anderson, June 1981. Preliminary reference Earth model. *Physics of the Earth and Planetary Interiors*, 25(4):297–356. ISSN 00319201. doi: 10.1016/0031-9201(81)90046-7.

England, Philip and James Jackson, 1989. Active Deformation of the Continents. *Annual Review of Earth and Planetary Sciences*, 17(1):197–226. doi: 10.1146/annurev.ea.17.050189.001213.

England, Philip and Peter Molnar, 1997. The field of crustal velocity in Asia calculated from Quaternary rates of slip on faults. *Geophysical Journal International*, 130(3): 551–582. ISSN 1365-246X. doi: 10.1111/j.1365-246X.1997.tb01853.x.

Feng, GuangCai, Eric A. Hetland, XiaoLi Ding, ZhiWei Li, and Lei Zhang, 2010. Coseismic fault slip of the 2008 Mw 7.9 Wenchuan earthquake estimated from InSAR and GPS measurements. *Geophysical Research Letters*, 37(1):L01302. ISSN 1944-8007. doi: 10.1029/2009GL041213.

Fielding, Eric J., Anthony Sladen, Zhenhong Li, Jean-Philippe Avouac, Roland Bürgmann, and Isabelle Ryder, 2013. Kinematic fault slip evolution source models of the 2008 M7.9 Wenchuan earthquake in China from SAR interferometry, GPS and teleseismic analysis and implications for Longmen Shan tectonics. *Geophysical Journal International*, 194:1138–1166. doi: 10.1093/gji/ggt155.

Geller, Robert J., 1976. Scaling relations for earthquake source parameters and magnitudes. *Bulletin of the Seismological Society of America*, 66(5):1501–1523.

Giang, Ha Thi, 2011. Focal mechanisms of earthquakes occurred in 2009-2010 in Northern Vietnam. *Final report of the 2011 Basic Project on science and technology of Institute of Geophysics. Stored at Institute of Geophysics, Hanoi, Vietnam.* (in Vietnamese).

Gusman, Aditya Riadi, Yuichiro Tanioka, Shinichi Sakai, and Hiroaki Tsushima, 2012. Source model of the great 2011 Tohoku earthquake estimated from tsunami waveforms and crustal deformation data. *Earth and Planetary Science Letters*, 341-344:234–242. ISSN 0012-821X. doi: 10.1016/j.epsl.2012.06.006.

Hanks, Thomas C. and Hiroo Kanamori, 1979. A moment magnitude scale. *Journal of Geophysical Research: Solid Earth*, 84(B5):2348–2350. ISSN 2156-2202. doi: 10.1029/JB084iB05p02348.

Hao, Ken Xiansheng, Hongjun Si, Hiroyuki Fujiwara, and Taku Ozawa, 2009. Coseismic surface-ruptures and crustal deformations of the 2008 Wenchuan earthquake Mw7.9, China. *Geophysical Research Letters*, 36(11):L11303. ISSN 1944-8007. doi: 10.1029/2009GL037971.

Hayes, G. P., 2011. Contemporary horizontal crustal movement estimation for northwestern Vietnam inferred from repeated GPS measurements. *Earth, Planets, and Space*, 63(7):529–534. doi: 10.5047/eps.2011.05.012.

Holt, W. E. and A. J. Haines, 1993. Velocity fields in deforming Asia from the inversion of earthquake-released strains. *Tectonics*, 12(1):1–20. ISSN 1944-9194. doi: 10.1029/92TC00658.

Holt, W. E., N. Chamot-Rooke, X. Le Pichon, A. J. Haines, B. Shen-Tu, and J. Ren, 2000. Velocity field in Asia inferred from Quaternary fault slip rates and Global Positioning System observations. *Journal of Geophysical Research: Solid Earth*, 105 (B8):19185–19209. ISSN 2156-2202. doi: 10.1029/2000JB900045.

Holt, William E., James F. Ni, Terry C. Wallace, and A. J. Haines, 1991. The active tectonics of the eastern Himalayan syntaxis and surrounding regions. *Journal of Geophysical Research: Solid Earth*, 96(B9):14595–14632. ISSN 2156-2202. doi: 10.1029/91JB01021.

Hung, Nguyen Van, 2002. Some basic features of neotectonic faults in northwestern Vietnam. *Geological Doctoral Thesis. Institute of Geological Sciences, Hanoi, Vietnam.* (in Vietnamese).

Hung, Nguyen Van and H. Q. Vinh, 2001. Moving characteristics of the Lai Chau-Dien Bien Fault zone during Cenozoic. *Journal of Geology: Series B*, 17-18:65–77.

Ide, Satoshi, Annemarie Baltay, and Gregory C. Beroza, 2011. Shallow Dynamic Overshoot and Energetic Deep Rupture in the 2011 Mw 9.0 Tohoku-Oki Earthquake. *Science*, 332(6036):1426–1429. doi: 10.1126/science.1207020.

Iinuma, T., M. Ohzono, Y. Ohta, and S. Miura, 2011. Coseismic slip distribution of the 2011 off the Pacific coast of Tohoku Earthquake (M 9.0) estimated based on GPS data—Was the asperity in Miyagi-oki ruptured? *Earth, Planets, and Space*, 63(7): 643–648. doi: 10.5047/eps.2011.06.013.

Isacks, Bryan, Jack Oliver, and Lynn R. Sykes, 1968. Seismology and the new global tectonics. *Journal of Geophysical Research*, 73(18):5855–5899. ISSN 2156-2202. doi: 10.1029/JB073i018p05855.

Ito, T., K. Ozawa, T. Watanabe, and T. Sagiya, 2011. Slip distribution of the 2011 off the Pacific coast of Tohoku Earthquake inferred from geodetic data. *Earth, Planets, and Space*, 63(7):627–630. doi: 10.5047/eps.2011.06.023.

Jackson, James and Dan McKenzie, 1988. The relationship between plate motions and seismic moment tensors, and the rates of active deformation in the Mediterranean and Middle East. *Geophysical Journal*, 93(1):45–73. ISSN 1365-246X. doi: 10.1111/j.1365-246X.1988.tb01387.x.

Jackson, James, John Haines, and William Holt, 1992. The horizontal velocity field in the deforming Aegean Sea region determined from the moment tensors of earthquakes. *Journal of Geophysical Research: Solid Earth*, 97(B12):17657–17684. ISSN 2156-2202. doi: 10.1029/92JB01585.

Ji, Chen. and G. Hayes, 2008. Preliminary result of the May 12, 2008 Mw7.9 Eastern Sichuan, China earthquake. *U.S. Geological Survey*. http://earthquake.usgs.gov/earthquakes/eqinthenews/2008/us2008ryan/finite_fault.php.

King, R. W., F. Shen, B. C. Burchfiel, Z. Chen, Y. Li, Y. Liu, L. H. Royden, E. Wang, X. Zhang, and J. Zhao, 1997. Geodetic measurement of crustal motion in southwest China. *Geology*, 25:179–182.

Koketsu, Kazuki, Yusuke Yokota, Naoki Nishimura, Yuji Yagi, Shinichi Miyazaki, Kenji Satake, Yushiro Fujii, Hiroe Miyake, Shinichi Sakai, Yoshiko Yamanaka, and Tomomi Okada, 2011. A unified source model for the 2011 Tohoku earthquake. *Earth and Planetary Science Letters*, 310(3-4):480–487. ISSN 0012-821X. doi: 10.1016/j.epsl.2011.09.009.

Koper, K. D., A. R. Hutko, T. Lay, C. J. Ammon, and H. Kanamori, 2011. Frequency-dependent rupture process of the 2011 Mw 9.0 Tohoku Earthquake: Comparison of short- period P wave backprojection images and broadband seismic rupture models. *Earth, Planets, and Space*, 63(7):599–602. doi: 10.5047/eps.2011.05.026.

Kreemer, C., J. Haines, W. E. Holt, G. Blewitt, and D. Lavallee, 2000. On the determination of a global strain rate model. *Earth, Planets, and Space*, 52:765–770.

Kreemer, C., W. E. Holt, and A. J. Haines, 2003. An integrated global model of present-day plate motions and plate boundary deformation. *Geophysical Journal International*, 154(1):8–34. ISSN 1365-246X. doi: 10.1046/j.1365-246X.2003.01917.x.

Kreemer, C., G. Blewitt, W. C. Hammond, and H.-P. Plag, 2006. Global deformation from the great 2004 Sumatra-Andaman Earthquake observed by GPS: Implications for rupture process and global reference frame. *Earth, Planets, and Space*, 58:141–148.

Kreemer, C., G. Blewitt, and W. C. Hammond, 2009. Geodetic constraints on contemporary deformation in the northern Walker Lane: 2. Velocity and strain rate tensor analysis. *Geological Society of America Special Papers*, 447:17–31. doi: 10.1130/2009.2447(02).

Kreemer, C., G. Blewitt, and W. C. Hammond, 2010. Evidence for an active shear zone in southern Nevada linking the Wasatch fault to the Eastern California shear zone. *Geological Society of America*, 38(5):475–478. doi: 10.1130/G30477.1.

Lacassin, Robin, Henri Maluski, P. Herve Leloup, Paul Tapponnier, Chaiyan Hinthong, Kanchit Siribhakdi, Saengathit Chuaviroj, and Adul Charoenravat, 1997. Tertiary diachronic extrusion and deformation of western Indochina: Structural and 40Ar/39Ar

evidence from NW Thailand. *Journal of Geophysical Research: Solid Earth*, 102(B5): 10013–10037. ISSN 2156-2202. doi: 10.1029/96JB03831.

Lai, Kuang-Yin, Yue-Gau Chen, and Doan Dinh Lam, 2012. Pliocene-to-present morphotectonics of the Dien Bien Phu fault in northwest Vietnam. *Geomorphology*, 173-174:52–68. ISSN 0169-555X. doi: 10.1016/j.geomorph.2012.05.026.

Lay, Thorne, Hiroo Kanamori, Charles J. Ammon, Meredith Nettles, Steven N. Ward, Richard C. Aster, Susan L. Beck, Susan L. Bilek, Michael R. Brudzinski, Rhett Butler, Heather R. DeShon, Goran Ekstrom, Kenji Satake, and Stuart Sipkin, 2005. The Great Sumatra-Andaman Earthquake of 26 December 2004. *Science*, 308(5725):1127–1133. doi: 10.1126/science.1112250.

Leloup, Philippe Herve, Robin Lacassin, Paul Tapponnier, Urs Scharer, Dalai Zhong, Xiaohan Liu, Liangshang Zhang, Shaocheng Ji, and Phan Trong Trinh, 1995. The Ailao Shan-Red River shear zone (Yunnan, China), Tertiary transform boundary of Indochina. *Tectonophysics*, 251(1-4):3–84. ISSN 0040-1951. doi: 10.1016/0040-1951(95)00070-4.

Lepvrier, C., H. Maluski, Vu Van Tich, A. Leyreloup, Phan Truong Thi, and Nguyen Van Vuong, 2004. The Early Triassic Indosinian orogeny in Vietnam (Truong Son Belt and Kontum Massif); implications for the geodynamic evolution of Indochina. *Tectonophysics*, 393(1-4):87–118. ISSN 0040-1951. doi: 10.1016/j.tecto.2004.07.030.

Lichten, Stephen M. and James S. Border, 1987. Strategies for high-precision Global Positioning System orbit determination. *Journal of Geophysical Research: Solid Earth*, 92(B12):12751–12762. ISSN 2156-2202. doi: 10.1029/JB092iB12p12751.

Lisowski, M., J. C. Savage, and W. H. Prescott, 1991. The velocity field along the San Andreas Fault in central and southern California. *Journal of Geophysical Research: Solid Earth*, 96(B5):8369–8389. ISSN 2156-2202. doi: 10.1029/91JB00199.

Magistrale, H., 2002. Relative contributions of crustal temperature and composition to controlling the depth of earthquakes in Southern California. *Geophysical Research Letters*, 29(10). doi: 10.1029/2001GL014375.

Marshall, Scott T., Gareth J. Funning, and Susan E. Owen, 2013. Fault slip rates and interseismic deformation in the western Transverse Ranges, California. *Journal of Geophysical Research: Solid Earth*, 118(8):4511–4534. ISSN 2169-9356. doi: 10.1002/jgrb.50312.

McCaffrey, Robert, 2005. Block kinematics of the Pacific-North America plate boundary in the southwestern United States from inversion of GPS, seismological, and geologic

data. *Journal of Geophysical Research: Solid Earth*, 110(B7). ISSN 2156-2202. doi: 10.1029/2004JB003307.

McCaffrey, Robert, 2009. The Tectonic Framework of the Sumatran Subduction Zone. *Annual Review of Earth and Planetary Sciences*, 37(1):345–366. doi: 10.1146/annurev.earth.031208.100212.

McClusky, S., S. Balassanian, A. Barka, C. Demir, S. Ergintav, I. Georgiev, O. Gurkan, M. Hamburger, K. Hurst, H. Kahle, K. Kastens, G. Kekelidze, R. King, V. Kotzev, O. Lenk, S. Mahmoud, A. Mishin, M. Nadariya, A. Ouzounis, D. Paradissis, Y. Peter, M. Prilepin, R. Reilinger, I. Sanli, H. Seeger, A. Tealeb, M. N. Toksoz, and G. Veis, 2000. Global Positioning System constraints on plate kinematics and dynamics in the eastern Mediterranean and Caucasus. *Journal of Geophysical Research: Solid Earth*, 105(B3):5695–5719. ISSN 2156-2202. doi: 10.1029/1999JB900351.

McKenzie, Dan and James Jackson, 1983. The relationship between strain rates, crustal thickening, palaeomagnetism, finite strain and fault movements within a deforming zone. *Earth and Planetary Science Letters*, 65(1):182–202. ISSN 0012-821X. doi: 10.1016/0012-821X(83)90198-X.

Michel, Gero W., Yue Qui Yu, Sheng Yuan Zhu, Christoph Reigber, Matthias Becker, Ewald Reinhart, Wim Simons, Boudewijn Ambrosius, Christophe Vigny, Nicolas Chamot-Rooke, Xavier Le Pichon, Peter Morgan, and Saskia Matheussen, 2001. Crustal motion and block behaviour in SE-Asia from GPS measurements. *Earth and Planetary Science Letters*, 187(3-4):239–244. ISSN 0012-821X. doi: 10.1016/S0012-821X(01)00298-9.

Minh, Le Huy, Pham Van Ngoc, Daniele Boyer, Nguyen Ngoc Thuy, Le Truong Thanh, Ngo Van Quan, and Guy Marquis, 2009. Investigation on the deep geoelectric structure of the Lai Chau - Dien Bien fault zone by magnetotelluric sounding. *Journal of Geology, Series A*, 311(3-4):11–21. (in Vietnamese, with English Abstr.).

Minh, Le Huy, Dinh Van Toan, Vo Thanh Son, Nguyen Chien Thang, Nguyen Ba Duan, Nguyen Ha Thanh, Le Truong Thanh, and Guy Marquis, 2011. Preliminary results of processing the sounding magnetotelluric data of Hoa Binh - Thai Nguyen and Thanh Hoa - Ha Tay profiles. *Journal of Earth Science*, 33(1):18–28. (in Vietnamese, with English Abstr.).

Minster, J. Bernard and Thomas H. Jordan, 1978. Present-day plate motions. *Journal of Geophysical Research: Solid Earth*, 83(B11):5331–5354. ISSN 2156-2202. doi: 10.1029/JB083iB11p05331.

Miyazaki, S., J. J. McGuire, and P. Segall, 2011. Seismic and aseismic fault slip before and during the 2011 off the Pacific coast of Tohoku Earthquake. *Earth, Planets, and Space*, 63(7):637–642.

Molnar, Peter and Paul Tapponnier, 1975. Cenozoic Tectonics of Asia: Effects of a Continental Collision. *Science*, 189(4201):419–426. doi: 10.1126/science.189.4201.419.

Morgan, W. Jason, 1968. Rises, trenches, great faults, and crustal blocks. *Journal of Geophysical Research*, 73(6):1959–1982. ISSN 2156-2202. doi: 10.1029/JB073i006p01959.

Morley, C.K., 2004. Nested strike-slip duplexes, and other evidence for Late Cretaceous–Palaeogene transpressional tectonics before and during India–Eurasia collision, in Thailand, Myanmar and Malaysia. *Journal of the Geological Society*, 161(5):799–812. doi: 10.1144/0016-764903-124.

Nakamura, Takeshi, Seiji Tsuboi, Yoshiyuki Kaneda, and Yoshiko Yamanaka, 2010. Rupture process of the 2008 Wenchuan, China earthquake inferred from teleseismic waveform inversion and forward modeling of broadband seismic waves. *Tectonophysics*, 491(1-4):72–84. ISSN 0040-1951. doi: 10.1016/j.tecto.2009.09.020.

Niell, A. E., 1996. Global mapping functions for the atmosphere delay at radio wavelengths. *ournal of Geophysical Research: Solid Earth*, 101(B2):3227–3246. doi: 10.1029/95JB03048.

Nishimura, T., H. Munekane, and H. Yarai, 2011. The 2011 off the Pacific coast of Tohoku Earthquake and its aftershocks observed by GEONET. *Earth, Planets, and Space*, 63:631–636. doi: 10.5047/eps.2011.06.025.

Nishimura, Takuya, Tomowo Hirasawa, Shin'ichi Miyazaki, Takeshi Sagiya, Takashi Tada, Satoshi Miura, and Kazuo Tanaka, 2004. Temporal change of interplate coupling in northeastern Japan during 1995–2002 estimated from continuous GPS observations. *Geophysical Journal International*, 157(2):901–916. doi: 10.1111/j.1365-246X.2004.02159.x.

Ozawa, S., T. Nishimura, H. Suito, T. Kobayashi, M. Tobita, and T. Imakiire, 2011. Coseismic and postseismic slip of the 2011 magnitude-9 Tohoku-Oki earthquake. *Nature*, 475:373–376. doi: 10.1038/nature10227.

Peterson, M. D., W. A. Bryant, C. H. Cramer, T. Cao, M. S. Reichle, A. D. Frankel, J. J. Lienkaemper, P. A. McCrory, and D. P. Schwartz, 1996. Probabilistic seismic hazard assessment for the state of California. *U.S. Geol. Surv. Open File Rep.*, (96-76):1–64.

Pollitz, Fred F., 1996. Coseismic Deformation From Earthquake Faulting On A Layered Spherical Earth. *Geophysical Journal International*, 125(1):1–14. ISSN 1365-246X. doi: 10.1111/j.1365-246X.1996.tb06530.x.

Pollitz, Fred F., Roland Burgmann, and Paramesh Banerjee, 2011. Geodetic slip model of the 2011 M9.0 Tohoku earthquake. *Geophysical Research Letters*, 38(7). ISSN 1944-8007. doi: 10.1029/2011GL048632.

Saastamoinen, J. *Atmospheric correction for the troposphere and stratosphere in radio ranging satellites*, volume 15, pages 247–251. AGU, Washington, DC, 1972. ISBN 0-87590-015-1. doi: 10.1029/GM015p0247.

Sagiya, Takeshi, August 2004. A decade of GEONET: 1994-2003 - The continuous GPS observation in Japan and its impact on earthquake studies. *Earth, Planets, and Space*, 56:xxix–xli.

Sagiya, Takeshi, Shin'ichi Miyazaki, and Takashi Tada, 2000. Continuous GPS Array and Present-day Crustal Deformation of Japan. *Pure and Applied Geophysics*, 157 (11-12):2303–2322. ISSN 0033-4553. doi: 10.1007/PL00022507.

Sato, Mariko, Tadashi Ishikawa, Naoto Ujihara, Shigeru Yoshida, Masayuki Fujita, Masashi Mochizuki, and Akira Asada, 2011. Displacement Above the Hypocenter of the 2011 Tohoku-Oki Earthquake. *Science*, 332(6036):1395. doi: 10.1126/science.1207401.

Savage, J. C. and R. O. Burford, 1973. Geodetic determination of relative plate motion in central California. *Journal of Geophysical Research*, 78(5):832–845. ISSN 2156-2202. doi: 10.1029/JB078i005p00832.

Schmalzle, G., T.H. Dixon, R. Malservisi, and R. Govers, may 2006. Strain accumulation across the Carrizo segment of the San Andreas Fault, California: Impact of laterally varying crustal properties. *Journal of Geophysical Research*, 111:B05403. doi: 10.1029/2005JB003843.

Shao, G., X. Li, C. Ji, and T. Maeda, July 2011. Focal mechanism and slip history of the 2011 Mw 9.1 off the Pacific coast of Tohoku Earthquake, constrained with teleseismic body and surface waves. *Earth, Planets, and Space*, 63:559–564. doi: 10.5047/eps.2011.06.028.

Shaw, B. E. and S. G. Wesnousky, December 2008. Slip-length scaling in large earthquakes: The role of deep penetrating slip below the seismogenic layer. *Bulletin of the Seismological Society of America*, 98(4):1633–1641. doi: 10.1785/0120070191.

Shaw, Bruce E. and Christopher H. Scholz, 2001. Slip-length scaling in large earthquakes: Observations and theory and implications for earthquake physics. *Geophysical Research Letters*, 28(15):2995–2998. ISSN 1944-8007. doi: 10.1029/2000GL012762.

Shen, Jun, Yipeng Wang, and Fangmin Song, 2003. Characteristics of the active Xiaojiang fault zone in Yunnan, China: a slip boundary for the southeastward escaping Sichuan-Yunnan Block of the Tibetan Plateau. *Journal of Asian Earth Sciences*, 21 (10):1085–1096. ISSN 1367-9120. doi: 10.1016/S1367-9120(02)00185-2.

Shen, Zheng-Kang, David D. Jackson, and Bob X. Ge, 1996. Crustal deformation across and beyond the Los Angeles basin from geodetic measurements. *Journal of Geophysical Research: Solid Earth*, 101(B12):27957–27980. ISSN 2156-2202. doi: 10.1029/96JB02544.

Shen, Zheng-Kang, Jiangning Lu, Min Wang, and Roland Burgmann, 2005. Contemporary crustal deformation around the southeast borderland of the Tibetan Plateau. *Journal of Geophysical Research: Solid Earth*, 110(B11). ISSN 2156-2202. doi: 10.1029/2004JB003421.

Shen, Zheng-Kang, J. Sun, P. Zhang, Y. Wan, M. Wang, R. Burgmann, Y. Zeng, W. Gan, H. Liao, and Q. Wang, 2009. Slip maxima at fault junctions and rupturing of barriers during the 2008 Wenchuan earthquake. *Nature Geoscience*, 2:718–724. doi: 10.1038/nego636.

Shestakov, Nikolay V., Hiroaki Takahashi, Mako Ohzono, Alexander S. Prytkov, Victor G. Bykov, Mikhail D. Gerasimenko, Margarita N. Luneva, Grigory N. Gerasimov, Andrey G. Kolomiets, Vladimir A. Bormotov, Nikolay F. Vasilenko, Jeongho Baek, Pil-Ho Park, and Mikhail A. Serov, 2012. Analysis of the far-field crustal displacements caused by the 2011 Great Tohoku earthquake inferred from continuous GPS observations. *Tectonophysics*, 524-525:76–86. ISSN 0040-1951. doi: 10.1016/j.tecto.2011.12.019.

Simons, Mark, Sarah E. Minson, Anthony Sladen, Francisco Ortega, Junle Jiang, Susan E. Owen, Lingsen Meng, Jean-Paul Ampuero, Shengji Wei, Risheng Chu, Donald V. Helmberger, Hiroo Kanamori, Eric Hetland, Angelyn W. Moore, and Frank H. Webb, 2011. The 2011 Magnitude 9.0 Tohoku-Oki Earthquake: Mosaicking the Megathrust from Seconds to Centuries. *Science*, 332(6036):1421–1425. doi: 10.1126/science.1206731.

Simons, W. J. F., A. Socquet, C. Vigny, B. A. C. Ambrosius, S. Haji Abu, Chaiwat Promthong, C. Subarya, D. A. Sarsito, S. Matheussen, P. Morgan, and W. Spakman, 2007. A decade of GPS in Southeast Asia: Resolving Sundaland motion

and boundaries. *Journal of Geophysical Research: Solid Earth*, 112:B06420. doi: 10.1029/2005JB003868.

Smith-Konter, Bridget R., David T. Sandwell, and Peter Shearer, 2011. Locking depths estimated from geodesy and seismology along the San Andreas Fault System: Implications for seismic moment release. *Journal of Geophysical Research: Solid Earth*, 116(B6). ISSN 2156-2202. doi: 10.1029/2010JB008117.

Son, Le Tu, 2000. Focal mechanism of Ta Khoa, Lai Chau and Muong Luan earthquakes in Northwest of Vietnam. *Journal of Earth Science*, 22(4):355–360. (in Vietnamese, with English Abstr.).

Son, Le Tu, 2004. The Dien Bien Earthquake, Ms = 5.3 on February 19, 2001. *Journal of Earth Science*, 26(2):112–121. (in Vietnamese, with English Abstr.).

Son, Le Tu, 2012. Study on the predicted induced-earthquake in vicinity of Lake Son La. *National Project on science and technology. DTDL.2009T/09. Period 2009-2011. Stored at Institute of Geophysics, Hanoi, Vietnam.* (in Vietnamese).

Tapponnier, P., G. Peltzer, A. Y. Le Dain, R. Armijo, and P. Cobbold, 1982. Propagating extrusion tectonics in Asia: New insights from simple experiments with plasticine. *Geology*, 10(12):611–616.

Tapponnier, P., R. Lacassin, P. H. Leloup, U. Scharer, Zhong Dalai, Wu Haiwei, Liu Xiaohan, Ji Shaochengi, Zhang Lianshangi, and Zhong Jiayou, 1990. The Ailao Shan/Red River metamorphic belt: Tertiary left-lateral shear between Indochina and South China. *Nature*, 343:431–437. doi: 10.1038/343431a0.

Thatcher, Wayne, 2003. GPS constraints on the kinematics of continental deformation. *International Geology Review*, 45:191–212.

Thuy, Nguyen Ngoc, 2005. Detailed earthquake zoning for northwestern Vietnam. *Final report of National Project on science and technology. KC08-10. Period 2001-2005. Stored at Institute of Geophysics, Hanoi, Vietnam.* (in Vietnamese).

Thuy, Nguyen Ngoc, Nguyen Dinh Xuyen, and Nguyen Thanh Tung, 1993. Induced earthquakes in Hoa Binh reservoir. *Journal of Earth Science*, 12(4):97–101. (in Vietnamese).

Tong, X., D. T. Sandwell, and Y. Fialko, 2010. Coseismic slip model of the 2008 Wenchuan earthquake derived from joint inversion of interferometric synthetic aperture radar, GPS, and field data. *Journal of Geophysical Research*, 115(B04314). doi: 10.1029/2009JB006625.

Tran, Dinh To, 2001. The analysis of GPS data in Tam Dao - Ba Vi network. *Journal of Earth Science*, 23(1):42–48. (in Vietnamese, with English Abstr.).

Tran, Dinh To, 2006. Processing results of GPS measurement data from the Son La and Song Da fault zones. *Journal of Geology, Series B*, 27:115–122.

Tran, Dinh To, Nguyen Trong Yem, Duong Chi Cong, Vy Quoc Hai, Witold Zuchiewicz, Nguyen Quoc Cuong, and Nguyen Viet Nghia, 2013. Recent crustal movements of northern Vietnam from GPS data. *Journal of Geodynamics*, 69:5–10. ISSN 0264-3707. doi: 10.1016/j.jog.2012.02.009.

Tsai, Victor C., Meredith Nettles, Goran Ekstrom, and Adam M. Dziewonski, 2005. Multiple CMT source analysis of the 2004 Sumatra earthquake. *Geophysical Research Letters*, 32(17). ISSN 1944-8007. doi: 10.1029/2005GL023813.

Tung, Van Duc, 2011. Development characteristics of the Lai Chau - Dien Bien fault zone. *Geological Doctoral Thesis. Institute of Geological Sciences, Hanoi, Vietnam.* (in Vietnamese, with English Summary).

Tung, Van Duc and Tran Van Thang, 2006. Neotectonic and geodynamic characteristics of Lai Chau town and its adjacency. *Journal of Earth Science*, 28(2):121–130. (in Vietnamese, with English Abstr.).

Tung, Van Duc and Tran Van Thang, 2008. Characteristics of active fault and neotectonic in Na Pheo - Nam Ty area. *Journal of Earth Science*, 30(1):73–83. (in Vietnamese, with English Abstr.).

Van, Phan Thi Kim, 2006. The Lai Chau-Dien Bien neotectonic fault zone and its acting manifestations by moderate local earthquakes. *Journal of Geology, Series B*, 27:40–48.

Vigny, C., W. J. F. Simons, S. Abu, R. Bamphenyu, C. Satirapod, N. Choosakul, C. Subarya, A. Socquet, K. Omar, H. Z. Abidin, and B. A. C. Ambrosius, 2005. Insight into the 2004 Sumatra-Andaman earthquake from GPS measurements in southeast Asia. *Nature*, 436:201–206.

Vy, Quoc Hai, Dinh To Tran, and Ngo Van Liem, 2011. Determination of present crustal movements of Red River Fault Zone by the Tam Dao - Ba Vi GPS network (1994-2007). *Journal of Earth Science*, 33(3DB):474–479. (in Vietnamese, with English Abstr.).

Wang, D. and J. Mori, July 2011. Rupture process of the 2011 off the Pacific coast of Tohoku Earthquake (Mw 9.0) as imaged with back-projection of teleseismic P-waves. *Earth, Planets, and Space*, 63:603–607. doi: 10.5047/eps.2011.05.029.

Wang, E., B. C. Burchfiel, L. H. Royden, L. Chen, J. Chen, W. Li, and Z. Chen. *Late Cenozoic Xianshuihe-Xiaojiang, Red River, and Dali fault systems of southwestern Sichuan and central Yunnan, China*, volume 327, page 108. The Geological Society of America: Special Paper, 1998.

Wang, Q., P. Z. Zhang, J. T. Freymueller, R. Bilham, K. M. Larson, X. Lai, X. You, Z. Niu, J. Wu, Y. Li, J. Liu, Z. Yang, and Q. Chen, 2001. Present-day crustal deformation in China constrained by Global Positioning System measurements. *Science*, 294(5542):574–577. doi: 10.1126/science.1063647.

Wdowinski, S., 2009. Deep creep as a cause for the excess seismicity along the San Jacinto fault. *Nature Geoscience*, 2:882–885. doi: 10.1038/ngeo684.

Wells, Donald L. and Kevin J. Coppersmith, 1994. New empirical relationships among magnitude, rupture length, rupture width, rupture area, and surface displacement. *Bulletin of the Seismological Society of America*, 84(4):974–1002.

Williams, Simon D. P., 2003. Offsets in Global Positioning System time series. *Journal of Geophysical Research: Solid Earth*, 108(B6). ISSN 2156-2202. doi: 10.1029/2002JB002156.

Wilson, P., J. Rais, Ch. Reigber, E. Reinhart, B. A. C. Ambrosius, X. Le Pichon, M. Kasser, P. Suharto, Dato Abdul Majid, Dato Paduka Awang Haji Othman Bin Haji Yaakub, R. Almeda, and C. Boonphakdee, 1998. Study provides data on active plate tectonics in southeast Asia region. *Eos, Transactions American Geophysical Union*, 79(45):545–549. ISSN 2324-9250. doi: 10.1029/98EO00398.

Xu, Caijun, Yang Liu, Yangmao Wen, and Rongjiang Wang, 2010. Coseismic Slip Distribution of the 2008 Mw 7.9 Wenchuan Earthquake from Joint Inversion of GPS and InSAR Data. *Bulletin of the Seismological Society of America*, 100(5B):2736–2749. doi: 10.1785/0120090253.

Xuyen, Nguyen Dinh and Nguyen Kim Lap, 1985. The 24 June 1983 Tuan Giao earthquake. *Proceeding of Institute of Geophysics, Hanoi*, IV. (in Vietnamese).

Xuyen, Nguyen Dinh and Tran Thi My Thanh, 1991. Recurrence Period of Strong Earthquakes in some Seismogenic Zones of Vietnam. *Journal of Earth Science*, 13(3). (in Vietnamese).

Yagi, Yuji and Yukitoshi Fukahata, 2011. Rupture process of the 2011 Tohoku-oki earthquake and absolute elastic strain release. *Geophysical Research Letters*, 38(19). ISSN 1944-8007. doi: 10.1029/2011GL048701.

Yin, An, 2010. Cenozoic tectonic evolution of Asia: A preliminary synthesis. *Tectonophysics*, 488(1-4):293–325. ISSN 0040-1951. doi: 10.1016/j.tecto.2009.06.002.

Yoshida, Y., H. Ueno, D. Muto, and S. Aoki, July 2011. Source process of the 2011 off the Pacific coast of Tohoku Earthquake with the combination of teleseismic and strong motion data. *Earth, Planets, and Space*, 63:565–569. doi: 10.5047/eps.2011.05.011.

Yue, H. and T. Lay, 2011. Inversion of high-rate (1 sps) GPS data for rupture process of the 11 March 2011 Tohoku earthquake (Mw 9.1). *Geophysical Research Letters*, 38 (7). ISSN 1944-8007. doi: 10.1029/2011GL048700.

Zhang, Guohong, Chunyan Qu, Xinjian Shan, Xiaogang Song, Guifang Zhang, Chisheng Wang, Jyr-Ching Hu, and Rongjiang Wang, 2011. Slip distribution of the 2008 Wenchuan Ms 7.9 earthquake by joint inversion from GPS and InSAR measurements: a resolution test study. *Geophysical Journal International*, 186(1):207–220. ISSN 1365-246X. doi: 10.1111/j.1365-246X.2011.05039.x.

Zhang, Jie, Yehuda Bock, Hadley Johnson, Peng Fang, Simon Williams, Joachim Genrich, Shimon Wdowinski, and Jeff Behr, 1997. Southern California permanent GPS geodetic array: Error analysis of daily position estimates and site velocities. *Journal of Geophysical Research: Solid Earth*, 102(B8):18035–18055. ISSN 2156-2202. doi: 10.1029/97JB01380.

Zuchiewicz, Witold, Nguyen Quoc Cuong, Andrzej Bluszcz, and Marek Michalik, 2004. Quaternary sediments in the Dien Bien Phu fault zone, NW Vietnam: a record of young tectonic processes in the light of OSL-SAR dating results. *Geomorphology*, 60 (3-4):269–302. ISSN 0169-555X. doi: 10.1016/j.geomorph.2003.08.004.

Appendix

EARTHQUAKE CATALOG OF NORTHWESTERN VIETNAM (1903 - 2012)

No.	Year	Month	Day	Hour	Minute	Second	Lat. (^{o})	Lon. (^{o})	Depth (km)	Mag.
1	1903	4					21.00	104.50	15	4.7
2	1903	4					19.58	105.08	21	5.2
3	1910	6					21.17	104.08	8	4.1
4	1910						21.25	104.33	15	4.7
5	1914	2		18			20.17	106.00	17	5.0
6	1914	12	10				22.08	103.17	11	5.0
7	1918	11					22.50	104.00	15	4.7
8	1920	2					21.41	103.00	16	4.9
9	1920	5		3			20.17	105.25	12	4.6
10	1920	6					21.42	103.00	13	4.6
11	1923	9	20				22.08	103.17	15	4.7
12	1923						20.25	106.08	12	4.6
13	1924			4			20.17	105.25	12	4.6
14	1926	9					21.33	103.83	8	4.8
15	1927	6					22.00	103.33	12	4.5
16	1928	12					22.08	103.17	11	4.5
17	1930	12					21.58	104.00	12	4.5
18	1933						21.25	103.17	7	4.1
19	1933						21.33	103.25	13	4.6
20	1934	1	12	13	32		22.10	103.10	12	3.3
21	1934	4	13	19	44		21.40	103.10	5	3.1
22	1934						21.17	104.92	12	4.7
23	1934			21	3		20.67	105.67	17	5.0
24	1935	11	1	16	22	11	21.08	103.25	22	6.8
25	1936	1	10				21.25	105.25	8	4.1
26	1936	3	27	20	11		21.42	103.42	18	4.8
27	1936	6	7	2	42		21.30	103.80	5	3.3
28	1936	6	24	16	4		21.30	103.80	5	3.3
29	1936	7	15	16	4		21.30	103.80	5	3.3
30	1936	8	4	4	44		21.30	103.80	5	3.3
31	1937	9	21	7	46		21.30	103.80	5	3.3

No.	Year	Month	Day	Hour	Minute	Second	Lat. (°)	Lon. (°)	Depth (km)	Mag.
32	1937	12					21.25	105.25	6	4.0
33	1939						20.50	105.92	12	4.6
34	1939	12					21.67	104.83	7	4.1
35	1940	12					22.17	103.67	20	4.8
36	1941	3	23	11	3		20.86	104.75	14	4.7
37	1942	5					21.75	103.08	10	4.4
38	1942	5	12				20.75	105.25	7	4.3
39	1942	10					22.17	104.33	13	4.6
40	1943	8	10	8	56		22.17	104.17	15	4.7
41	1945	2					21.50	103.66	9	4.2
42	1945	7					20.75	105.33	11	4.6
43	1945	9					21.08	105.08	15	4.7
44	1948						20.30	104.80	25	5.5
45	1951	4					20.97	104.97	13	4.1
46	1954						20.30	105.00	24	5.1
47	1957						19.25	104.50	21	5.2
48	1958	5					21.25	104.61	12	4.2
49	1958	8	13	13	20		20.02	105.57	20	5.2
50	1958						20.30	104.78	28	5.7
51	1960	3					20.05	105.58	15	4.1
52	1961	10					21.20	104.66	10	4.1
53	1961	11	26				22.50	102.60	15	4.1
54	1962	6	3				20.83	104.83	10	4.1
55	1964	3	29	16	50		20.10	105.20	15	4.1
56	1965						20.28	104.95	12	3.9
57	1966						19.36	105.45	17	4.1
58	1967	1	13	17	18		22.30	103.80	15	4.1
59	1968						20.05	105.62	25	5.1
60	1972						20.44	105.47	17	4.1
61	1973	7					20.30	104.96	17	4.1
62	1974	6					20.63	105.10	17	4.1
63	1976	3	9	10	16	10.4	20.65	103.45	10	3.1
64	1976	9	10		55	10.6	19.28	104.46	5	3.1
65	1976	10	4	16	23	5.6	21.73	104.01	5	3.1
66	1976						19.91	105.40	17	3.7
67	1977	1	5				20.05	105.62	19	4.7
68	1977	1	6				20.31	105.78	17	4.1
69	1977	2	4	11	12	48.5	22.08	102.05	9	3.6
70	1977	2	24	20	32	56.6	22.23	102.61	5	3.4
71	1977	2	25	15		8.4	22.19	103.16	5	3.4
72	1977	2	28	16	41		19.70	106.40	20	3.1

No.	Year	Month	Day	Hour	Minute	Second	Lat. (^{o})	Lon. (^{o})	Depth (km)	Mag.
73	1977	6	29	19	15	13.9	22.25	102.10	6	3.4
74	1977	7	15	14	16	53.8	22.33	102.91	5	3.4
75	1977	12	12	5	19	37	22.08	102.06	5	4.6
76	1978	2	6	6	8	57.9	22.30	102.38	10	3.9
77	1978	4	6	18	12	43.7	21.72	103.64	10	3.6
78	1978	4	26	11	52	28.3	21.85	102.34	6	3.4
79	1978	7	29	22	33	17.8	22.59	102.05	18	4.1
80	1978	8	10	9	38	58.3	22.05	102.68	5	3.7
81	1978	9	10	14	39	14	21.99	102.67	5	3.3
82	1978	9	11	10	7	47.6	22.19	102.09	12	3.3
83	1978	9	28	7	33	25.6	21.15	103.18	8	3.1
84	1978	9	28	8	23	13	22.71	103.23	19	4.4
85	1978	10	7	12	25	48.7	22.39	102.67	5	3.3
86	1978	11	11	22	32	6.4	21.29	103.35	19	3.4
87	1978	12	19	2		49.4	21.22	104.10	8	3.3
88	1979	2	24	17	15	56.8	20.14	105.10	8	3.2
89	1979	4	11	15		24.7	19.40	104.40	10	3.4
90	1979	5	7	7	59	34.2	22.60	103.80	2	3.5
91	1979	6	13	12	43	2.2	22.70	102.69	10	3.5
92	1979	9	14	19	55	52	19.71	105.29		3.2
93	1980	4	4	3	38	7.3	20.23	104.84	9	3.0
94	1980	4	7	5	3	32.7	22.58	102.02	8	3.9
95	1980	12	17	2	11	7.7	20.59	104.66	5	3.6
96	1980	12	17	17	46	46	20.93	104.82	5	3.3
97	1981	1	31		13	35.3	21.94	102.93	5	3.4
98	1981	4	21	19	5	8	22.65	103.00	30	4.1
99	1981	12	18	20	10	22.6	22.23	102.99	5	3.3
100	1982	2	20	9	25	16.2	22.30	102.50	30	4.5
101	1982	2	22	16	7	5.3	22.35	102.44	7	3.7
102	1982	4	30	9	16	19.4	20.31	105.65		3.0
103	1982	11	30	2	22	57	20.50	104.00	7	3.5
104	1982	12	1	1	34	38.2	21.02	104.30	10	4.1
105	1983	2	28	5	41	11.6	22.04	103.65	15	3.3
106	1983	3	7	6	54	58.6	20.55	104.95	15	3.2
107	1983	4	30	9	16	20.9	20.66	104.88	5	3.1
108	1983	6	24	7	18	15.4	21.71	103.43	18	6.2
109	1983	6	24	8	43	42.7	21.76	103.50	12	4.5
110	1983	6	24	15	45	5.78	21.60	103.48	33	4.0
111	1983	6	25	3	51	59.2	21.70	103.09	6	4.0
112	1983	6	25	8	18	24.6	21.79	103.23	0	3.7
113	1983	6	25	12	55	24.19	21.93	103.32	0	3.9
114	1983	6	25	13	16	18.72	21.59	103.18	1	4.3

No.	Year	Month	Day	Hour	Minute	Second	Lat. (^{o})	Lon. (^{o})	Depth (km)	Mag.
115	1983	6	25	17	40	34.29	21.72	103.31	25	4.5
116	1983	6	27	15	44	25.45	21.53	103.32	15	4.1
117	1983	7	1	16	45	1.1	21.47	103.07	0	4.0
118	1983	7	3	9	26	18.55	21.62	103.50	0	4.2
119	1983	7	7	11	16	38.83	21.80	103.21	33	3.5
120	1983	7	11	10	32	1.25	21.70	103.18	0	3.8
121	1983	7	14	21	33	56.16	21.55	103.35	63	4.4
122	1983	7	15	4	48	51.55	21.76	103.43	3	5.1
123	1983	9	4	16	39	42.41	22.05	102.81	33	4.2
124	1983	10	12	3	54	58.75	21.30	102.94	0	4.2
125	1983	10	29	13	29	47.8	22.40	103.57	19	3.5
126	1984	2	28	17	2	34.1	20.51	104.95	5	3.1
127	1984	3	21	7		53.4	20.64	103.50	1	3.3
128	1984	8	3	10	16	24.3	20.65	103.53	5	3.9
129	1984	8	4	7	50	59.5	20.65	103.54	5	3.0
130	1984	12	30	20	13	44.7	22.37	103.57	14	3.6
131	1984	12	31	8	59	59.5	19.80	104.92	18	3.2
132	1985	6	9	5	22	34.1	21.94	102.55	5	4.4
133	1985	6	9	21		33.7	22.61	102.31	15	3.4
134	1985	6	15	17	40	38	21.61	103.48	7	4.0
135	1985	6	16	12	37	9	21.69	103.36	8	4.0
136	1985	6	16	13	23	43.4	21.80	103.37	5	3.7
137	1985	8	19	13	41	18.8	22.15	102.68	10	4.8
138	1985	8	19	16	31	48.36	22.19	102.67	10	4.5
139	1985	10	21	21	53	34	21.59	103.31	19	4.0
140	1985	10	21	22	1	6.9	21.56	103.45	5	3.9
141	1985	11	1	17	1	19.4	21.85	103.35	19	4.1
142	1985	11	13	16	14	59.3	22.03	102.79	17	3.6
143	1986	1	20	20	3	54.7	21.88	103.37	8	4.1
144	1986	2	1	1	35	41	21.67	103.52	0	3.3
145	1986	3	2	23	52	5.7	21.71	103.36	10	4.9
146	1986	3	5	23	52	7.4	21.85	103.20	10	4.3
147	1986	3	9	5	2	15.7	20.93	103.33	5	3.7
148	1986	4	14	21	59	11	21.38	103.37	8	3.9
149	1986	8	24	1	15	45	21.57	103.45	20	3.5
150	1987	4	15	15	22	10.5	21.86	103.36	12	3.1
151	1987	4	21	16	7	5	20.84	103.50	7	3.2
152	1987	4	29	5	2	12.4	20.26	104.80	5	3.1
153	1987	5	30	8	23	29.3	20.58	103.70	10	3.3
154	1987	5	30	16	17	34.1	20.44	104.31	4	3.4
155	1987	6	10	7	20	49.2	21.83	103.37	12	3.5
156	1987	6	11	22	17	1.9	21.64	103.54	10	3.0

No.	Year	Month	Day	Hour	Minute	Second	Lat. (^{o})	Lon. (^{o})	Depth (km)	Mag.
157	1987	6	18	23	14	20	20.76	103.87	10	3.7
158	1987	6	21	15	49	49.4	20.42	104.45	20	3.6
159	1987	7	20	3	47	40.2	19.91	105.12	15	3.1
160	1987	9	7	1	46	26.4	21.36	103.13	19	3.3
161	1987	11	13	16	48	2.2	21.57	103.40	5	4.4
162	1987	11	13	17	9	44.8	21.56	103.29	19	3.3
163	1987	11	13	17	40	0.4	21.85	103.56	15	3.4
164	1987	11	14	20	42	3.9	21.49	103.52	19	3.2
165	1988	1	16	21	10	39.8	22.00	103.47	5	3.2
166	1988	1	30	4	48	41.5	22.73	102.92	15	4.2
167	1988	3	14	16	35	33.6	20.63	104.97	18	3.6
168	1988	3	14	22	57	18.9	21.44	104.01	2	3.7
169	1988	3	21	9	20	34.1	19.57	104.89	14	3.9
170	1988	6	15	6	13	7.9	20.45	105.17	5	3.8
171	1988	8	19	4	13	1.9	21.27	103.63	7	3.3
172	1989	2	7	19	57	5.9	21.73	103.23	16	3.7
173	1989	2	7	21	57	44.5	21.76	103.22	13	3.7
174	1989	4	14	12	37	44.8	20.71	105.23	20	3.8
175	1989	4	14	12	46	53.2	20.70	105.21	10	3.7
176	1989	4	20	15	29	5.9	22.01	102.44	5	4.0
177	1989	5	7	10	59	55.3	21.50	102.94	13	4.3
178	1989	5	22	23	5	23.2	20.80	105.30	15	4.8
179	1990	2	14	1	39	21.3	19.79	105.63	15	3.3
180	1990	2	14	7	28	29.6	21.88	103.46	7	3.8
181	1990	3	1	9	24	6.7	22.55	103.41	8	3.4
182	1990	3	26	7	59	34.9	21.54	103.69	19	3.3
183	1990	7	9	20	36	1.1	21.66	103.47	19	3.2
184	1991	1	3	15	43	36.1	22.08	103.15	15	3.0
185	1991	2	20	14	51	2.4	22.77	102.20	0	3.6
186	1991	4	5	15	34	29.8	22.22	102.34	5	3.6
187	1991	4	5	16	10	37.5	22.27	102.34	5	3.8
188	1991	4	5	16	21	9.7	22.27	102.56	0	4.2
189	1991	4	5	23	56	56.6	20.94	104.57	12	3.2
190	1991	5	9	13	37	52.7	21.79	102.84	0	3.4
191	1991	7	10	12	47	12.6	20.97	104.79	13	3.1
192	1991	8	14	16	8	23.1	22.04	103.56	0	3.0
193	1991	10	6	10	50	44	21.38	104.17	6	4.7
194	1991	10	11	2	26	23.1	21.36	104.18	11	4.1
195	1991	11	5	16	27	59.2	21.46	103.59	0	3.4
196	1991	12	1	17	6	28.1	21.61	104.03	15	3.1
197	1992	8	13	22	37	22.7	21.19	104.27	5	4.2

No.	Year	Month	Day	Hour	Minute	Second	Lat. (^{o})	Lon. (^{o})	Depth (km)	Mag.
198	1992	8	14	14	13	12.6	21.26	104.26	0	3.4
199	1992	8	21	22	57	32	21.19	104.18	9	3.9
200	1992	10	5	18	57	48.1	21.86	103.93	0	3.4
201	1992	10	28	17	37	25.1	21.61	104.92	8	3.2
202	1993	3	13	2	54	6.5	21.98	103.07	2	4.0
203	1993	3	29	1	17	28.4	21.83	103.15	10	4.7
204	1993	3	30	13	57	8.6	21.83	103.08	10	4.7
205	1993	4	11	6	27	41.7	21.75	103.07	8	3.9
206	1993	4	24	3	48	16.9	21.47	103.27	19	3.9
207	1993	5	24	20	30	57.7	21.97	103.21	19	4.1
208	1993	5	26	9	37	58.7	21.95	103.10	16	3.0
209	1993	7	14	14	9	24.1	22.40	103.90	18	3.7
210	1993	8	10	6	46	33.4	21.04	104.63	39	4.1
211	1993	9	14	18	12	26.4	22.05	102.60	0	3.7
212	1993	9	19	20	14	12	22.10	102.02	1	4.0
213	1993	10	23	3	58	36	21.52	104.87	0	3.5
214	1993	11	11	15	11	35.3	21.36	102.95	3	4.1
215	1993	12	21	10	4	5	22.19	103.26	10	3.8
216	1994	1	6	16	54	4.6	20.97	104.66	14	3.9
217	1994	3	31	14	19	5	22.62	102.73	0	3.2
218	1995	1	4	7	14	17.6	20.85	105.08	0	3.7
219	1995	4	16	17	44	36.6	20.12	105.82		3.5
220	1995	4	24	16	13	10.4	22.74	102.90	20	5.1
221	1995	5	13	17	9	32.2	22.49	102.44	0	3.3
222	1995	7	19	22	10	42.1	21.78	102.74	15	3.0
223	1995	11	9	20	55	15	22.06	102.76	16	4.5
224	1996	2	2	22	59	54	22.10	103.11	0	4.2
225	1996	2	9	2	13	20	20.24	105.06	5	3.3
226	1996	2	9	2	14	42.7	20.10	105.05	15	3.5
227	1996	3	18	18	19	38.1	20.80	104.71	0	3.0
228	1996	4	15	7	57	46	21.53	102.62	15	3.6
229	1996	4	27	9	52	20	22.33	102.16	45	3.7
230	1996	5	10	13	48	1.4	19.56	104.82	6	3.1
231	1996	6	22	18	39	29.9	21.29	103.44	5	4.7
232	1996	6	22	19	17	5	20.84	103.21	5	3.0
233	1996	7	26	17	22	21.6	21.29	103.37	17	3.2
234	1996	9	2	2	23	11.6	22.72	102.55	21	3.1
235	1996	9	24	13	31	30.2	21.74	103.45	5	3.3
236	1996	11	13	18	51	46	22.34	102.84	6	4.4
237	1997	1	30	22	13	10	22.03	102.68	30	3.2
238	1997	3	26	15	16	59.6	19.47	104.39	18	3.2
239	1997	4	18	5	10	23.2	20.22	104.88	19	3.2

No.	Year	Month	Day	Hour	Minute	Second	Lat. (^{o})	Lon. (^{o})	Depth (km)	Mag.
240	1997	6	7	14	7	35.6	21.09	104.85	5	3.9
241	1997	7	2	15	58	21	21.88	102.62	33	4.1
242	1997	7	29		35	17.6	20.16	105.06	19	3.1
243	1998	1	10	11	22	13	19.89	106.10	3	3.1
244	1998	2	10	8	18	3.4	21.13	104.81	20	3.1
245	1998	5	14	3	34	45.2	20.93	103.33	4	3.2
246	1998	6	30	6	10	55.3	20.40	104.74	15	4.3
247	1998	6	30	18	12	28.8	20.36	104.70		3.1
248	1998	11	15	12	29	44.7	22.43	104.06	16	3.0
249	1998	12	31	12	54	42.9	22.23	103.40	19	3.5
250	1999	1	27	7	27	59.4	22.29	103.33	29	3.4
251	1999	6	30	2	28	47.6	22.51	102.58	2	3.2
252	1999	7	7	11	26	11.9	22.60	103.33	21	3.5
253	1999	7	7	21	11	48.8	20.73	104.89	16	3.2
254	1999	9	13	19	9	12.5	20.78	104.90	6	3.4
255	1999	12	28	6	39	38.7	21.56	104.25	15	3.9
256	2000	4	8	6	46	5.2	21.85	103.46	20	3.1
257	2000	4	19	10	47	51	22.01	104.07	16	3.8
258	2000	10	5	15	54	54.7	21.87	103.52	7	3.4
259	2001	1	1	11	34	18.4	21.99	103.04	4	4.1
260	2001	2	19	15	51	34.2	21.33	102.85	2	5.1
261	2001	2	19	16	40	17.8	21.33	102.88	5	3.5
262	2001	2	19	19	2	49.2	21.42	102.87	5	3.8
263	2001	2	21	11	3	44.9	21.40	102.91	5	3.3
264	2001	2	22	11	36	34.3	21.36	102.95	5	3.2
265	2001	2	23	17	53	28.9	21.55	102.91	5	3.2
266	2001	2	24	22	14	31.4	21.34	102.94	5	3.6
267	2001	2	24	22	38	41.9	21.57	102.89	3	3.0
268	2001	3	4	20	19	48.8	21.31	102.83	1	4.2
269	2001	3	4	20	40	54.4	21.52	102.92	5	3.0
270	2001	3	5	15	6	58.3	21.50	102.83		3.3
271	2001	3	25	13	28	22.2	21.30	103.01	5	3.0
272	2001	3	29	13	32	22.56	22.56	103.43	5	3.1
273	2001	4	2	20	45	49.42	22.08	103.29	23	4.0
274	2001	4	3	4	30	10.3	22.27	103.36	5	3.0
275	2001	4	22	12	30	50.3	21.54	102.95	3	3.4
276	2001	4	23	15	51	20.4	21.39	103.05	4	3.7
277	2001	5	1	22	23	38.6	21.41	102.96	10	3.2
278	2001	6	4	21	2	14.9	22.03	102.41	10	3.9
279	2001	6	4	23	20	25.5	22.33	102.51		3.6
280	2001	6	8	7	38	13.7	21.14	102.94	8	3.1
281	2001	7	13	20	15	28.2	21.46	102.97	10	3.7

No.	Year	Month	Day	Hour	Minute	Second	Lat. (^{o})	Lon. (^{o})	Depth (km)	Mag.
282	2001	7	20	5	20	35	20.80	104.87	12	3.1
283	2001	7	31	2	3	33.63	21.57	103.01	15	3.6
284	2001	7	31	4	51	2.9	20.92	104.54		3.6
285	2001	9	7	20	33	46	22.53	102.36	5	3.4
286	2001	11	12	21	56	6.3	20.95	104.20	2	3.4
287	2001	11	28	4	42	18.75	22.25	103.03	10	3.8
288	2002	4	12	5	4	51.1	22.49	102.72	19	3.8
289	2002	8	16	14	36	21.1	21.88	103.20		3.1
290	2002	8	23	8	19	31.3	22.15	103.02	7	3.7
291	2002	8	23	8	21	10.9	22.58	103.33		3.2
292	2002	9	22	4	48	5.7	21.44	102.94	4	3.0
293	2002	12	5	13	45	32.9	22.03	103.06		3.2
294	2002	12	29	18	54	56.5	21.42	102.89		3.4
295	2002	12	29	19	5	30.6	22.02	103.06	15	3.9
296	2003	3	6	14	8	26.3	22.72	103.58		3.1
297	2003	7	27	13	39	58.2	20.84	103.22	4	3.7
298	2003	8	12	14	18	26.9	20.53	105.21	7	3.0
299	2003	8	19	12	21	9.9	22.15	103.32		3.2
300	2003	9	23	19	8	1.4	20.80	104.14	10	3.1
301	2003	10	14	8	20	20.8	21.11	103.13		3.3
302	2003	11	3	18	6	15.2	20.91	103.29	2	3.5
303	2003	11	8	15		57.1	21.04	104.79	10	3.3
304	2003	11	27	21	36	56.5	21.11	103.00	10	3.0
305	2003	12	13	13	57	57.8	21.51	103.11		3.1
306	2004	2	5	4	13	47	22.30	102.31	2	3.9
307	2004	5	11	18	33	32.8	22.79	103.61	8	3.1
308	2004	11	9	18	59	3.1	21.47	104.37	11	3.0
309	2004	11	15	10	36	51.1	20.61	103.92		3.1
310	2005	1	8	2	38	34.5	20.36	105.37	9	4.0
311	2005	2	3		5	1.7	21.52	103.69	15	3.0
312	2005	2	8	10	6	20.6	20.66	103.96	5	3.4
313	2005	2	17	8	25	41.8	21.42	104.07	17	3.1
314	2005	8	2	14	46	50.9	20.28	105.92	35	3.5
315	2005	9	26	13	48	37.6	22.48	102.24	29	4.6
316	2005	10	9	20	43	36.4	20.09	106.16	10	3.0
317	2005	11	11	5	36	45.9	19.47	104.53		3.3
318	2006	1	6	18	28	8.6	22.10	102.51	3	3.6
319	2006	1	15	14	29	47.1	21.74	103.30	12	3.0
320	2007	3	31	10	3	48.3	22.40	102.44	3	3.0
321	2008	2	10	2	41	46.5	21.62	103.40	12	3.1
322	2008	11	17	11	4	45.9	22.62	103.33	3	3.0

No.	Year	Month	Day	Hour	Minute	Second	Lat. (^{o})	Lon. (^{o})	Depth (km)	Mag.
323	2009	11	26	4	47	0.2	21.32	104.18	5	3.6
324	2009	11	26	13	59	1.8	21.34	104.19	9	3.6
325	2010	1	6	23	27	18.1	22.74	102.60	15	3.4
326	2010	9	6	4	13	15.7	22.50	102.21	3	3.1
327	2010	11	9	18	25	2.9	21.95	103.64	31	3.3
328	2010	12	30	18	50	20.3	20.87	103.45	17	4.8
329	2011	2	22	7	12	23.6	22.37	103.00	5	3.0
330	2011	4	28	2	1	49.6	22.00	103.39	5	3.4
331	2011	6	29	8	26	37.8	20.83	103.46	3	3.4
332	2012	1	21	11	54	24.8	21.63	103.66	5	3.2